

HIGHLY ROBUST SUPERHYDROPHOBIC COATING OF
ALUMINUM 2024-T3 ALLOY FOR CORROSION MITIGATION, DEICING,
AND SELF-CLEANING OF AIRCRAFT

A Thesis by

Balakrishnan Subeshan

Bachelor of Science, Wichita State University, 2017

Submitted to the Department of Mechanical Engineering
and the faculty of the Graduate School of
Wichita State University
in partial fulfillment of
the requirements for the degree of
Master of Science

May 2018

© Copyright 2018 by Balakrishnan Subeshan

All Rights Reserved

HIGHLY ROBUST SUPERHYDROPHOBIC COATING OF
ALUMINUM 2024-T3 ALLOY FOR CORROSION MITIGATION, DEICING,
AND SELF-CLEANING OF AIRCRAFT

The following faculty members have examined the final copy of this thesis for form and content, and recommend that it be accepted in partial fulfillment of the requirement for the degree of Master of Science, with a major in Mechanical Engineering.

Ramazan Asmatulu, Committee Chair

Muhammad Rahman, Committee Member

Mehmet Bayram Yildirim, Committee Member

DEDICATION

To my parents, sister, brother-in-law, friends, and country

ACKNOWLEDGEMENTS

I would like to express my heartfelt appreciation and gratefulness to Dr. Ramazan Asmatulu, my advisor, for his valuable supervision and exceptional support throughout my research. I also wish to thank my reading committee members, Dr. Muhammad Rahman and Dr. Mehmet Bayram Yildirim, for their remarks and advice on my work. I also acknowledge the Department of Mechanical Engineering for providing me with financial assistance. Special thanks go to Dr. Eylem Asmatulu from the Department of Mechanical Engineering for offering remarkable support during my research.

I would specifically like to thank my laboratory mate and sister, Aybala, who provided countless words of support and encouragement, in addition to lab assistance when needed. Another sister of mine, Dr. Jayangika, provided experiences and advices to help me avoid problems and face life positively. I would like to express gratitude toward Vinay for helping me through my studies. Also, special thanks to Nizam and Ankit for their help and support.

Last, and most importantly, I express my truthful appreciation, love, and gratitude to my father and mother, Balakrishnan and Nagakanni; my sister, Rewathi; and my brother-in-law, Prasanna, for their love, encouragement, and support in many ways throughout my life. Their belief in me and their pride in my achievements were the motivation and reward for all of my hard work.

ABSTRACT

Metals and alloys are used extensively because of their characteristics, including high strength, ability to bear heavy loads and stress, ductility, machinability, and so on. Metals and alloys are subject to corrosion when they come in contact with an aggressive environment. Among all the metals and alloys, aluminum is primarily used for various applications under aggressive atmospheric conditions, which result in its loss of metallic luster, changes in the dimensions of the aluminum, and its loss of strength. Many techniques have been used to minimize the corrosion of aluminum and its alloys, one of which is to employ a plasma surface cleaning treatment. Using this technique to fabricate the aluminum surface as a superhydrophobic (SH)-coated surface is the ultimate goal, whereby the coated surface becomes a water-fearing surface, can resist corrosion for a longer period of time, and can be applied as the best surface for icing conditions. Heat treatment was executed on the surface to make the SH coating highly robust.

The corrosive behavior of Aluminum 2024-T3 alloy was tested using a 3.0% sodium chloride (NaCl) solution, which is an aggressive solution. The resulting behavior was investigated by means of contact angle measurement, linear polarization, electrochemical impedance spectroscopy (EIS), Fourier transform-infrared (FTIR) spectroscopy, Vickers microhardness, and salt soaking. Additional tests—tape adhesive, deicing, freezing time, super-cooled water, and self-cleaning—were performed to show that the surface coat remains superhydrophobic schematically. It was discovered that the plasma surface cleaning treatment increases the adhesiveness between the substrate and the top coat, which results in the coated surface remaining superhydrophobic for a long period of time. The corrosion rate of the surface is also reduced, which provides a double benefit.

TABLE OF CONTENTS

Chapter	Page
1. INTRODUCTION	1
1.1 Background	1
1.2 Motivation and Objective	2
2. LITERATURE REVIEW	5
2.1 Metals and Alloys in Manufacturing Industry	5
2.1.1 Aluminum 2024-T3 Alloys	5
2.1.2 Industrial Uses of Aluminum 2024-T3 Alloys	6
2.2 Definition of Corrosion	7
2.2.1 Classification of Corrosion	9
2.2.1.1 General Attack Corrosion	9
2.2.1.2 Pitting Corrosion	10
2.2.1.3 Crevice Corrosion	10
2.2.1.4 Galvanic Corrosion	11
2.2.1.5 Environmentally Induced Cracking Corrosion	12
2.2.1.6 Intergranular Corrosion	12
2.2.1.7 De-Alloying Corrosion	13
2.2.1.8 Erosion-Assisted Corrosion	13
2.2.2 Mechanism of Corrosion	13
2.2.3 Importance of Corrosion Mitigation	16
2.3 Corrosion Mitigation Methods	17
2.3.1 Environmental Modification	17
2.3.2 Cathodic Protection	18
2.3.2.1 Galvanic Anode System	18
2.3.2.2 Impressed Current Protection System	19
2.3.3 Metal Selection	20
2.3.4 Corrosion Inhibitors	20
2.3.5 Coatings	21
2.3.6 Plating	22
2.3.6.1 Electroplating	22
2.3.6.2 Mechanical Plating	22
2.3.6.3 Electroless Plating	23
2.3.6.4 Hot Dipping	23
2.3.7 Plasma Surface Cleaning Treatment	23
2.3.7.1 Mechanism of Plasma Surface Cleaning Treatment	25
2.3.7.2 Benefits of Plasma Surface Cleaning Treatment	27
2.4 Corrosion Rate Measurement	28
2.4.1 Linear Polarization Method	28
2.4.2 Electrochemical Impedance Spectroscopy	32

TABLE OF CONTENTS (continued)

Chapter	Page
2.5	Principle of Superhydrophobicity40
2.5.1	Hydrophilic, Hydrophobic, and Superhydrophobic Surfaces40
2.5.2	Contact Angle and Wettability of Superhydrophobic Surfaces42
2.5.3	Wenzel State and Cassie-Baxter Model46
2.6	Icing Problems and Their Solutions.....48
2.6.1	Atmospheric Icing.....49
2.6.2	In-Cloud Icing.....50
2.6.3	Precipitation Icing.....50
3.	EXPERIMENTAL MATERIALS AND METHODS51
3.1	Experimental Materials51
3.1.1	Aluminum 2024-T3 Alloy51
3.1.2	Ultrasonic Cleaner52
3.1.3	Mini Sprayer53
3.1.4	Superhydrophobic Coatings.....54
3.1.4.1	Bottom Coat55
3.1.4.2	Top Coat.....55
3.1.5	Plasma Cleaner Used for Preparing Sample Surface56
3.1.6	Industrial Oven Used for Heat Treatment.....57
3.1.7	Optical Contact Angle Goniometer58
3.1.8	3M Adhesion Tape.....59
3.1.9	Sodium Chloride Solution.....59
3.1.10	Deionized Water60
3.1.11	Gamry Reference 600 Potentiostat60
3.1.12	Fourier Transform Infrared Spectrometry62
3.1.13	Vickers Hardness Test64
3.1.14	Ice Cube66
3.1.15	Inclinometer67
3.1.16	Digital Anemometer.....67
3.1.17	Electric Blower68
3.1.18	Water Sprayer68
3.2	Experimental Methods69
3.2.1	Aluminum 2024-T3 Alloy Division72
3.2.2	Cleaning of Aluminum 2024-T3 Alloy.....72
3.2.3	Preparation of Bottom Coat73
3.2.4	Application of Bottom Coat.....73
3.2.5	Plasma Surface Cleaning Treatment.....74
3.2.6	Preparation of Top Coat.....75
3.2.7	Application of Top Coat76
3.2.8	Heat Treatment of Aluminum 2024-T3 Alloy76
3.2.9	Measuring Contact Angle76

TABLE OF CONTENTS (continued)

Chapter	Page
3.2.10	Tape Adhesion Test on Plasma-Treated SH-Coated Samples77
3.2.11	Immersion in 3% 0.5M NaCl Solution78
3.2.12	Measuring Corrosion Rate Using Polarization Curves78
3.2.13	Electrochemical Analysis Using Electrochemical Impedance Spectroscopy80
3.2.14	Performing Fourier Transform Infrared Analysis81
3.2.15	Measuring Vickers Hardness Number81
3.2.16	Preparing Ice Cubes for De-Icing Test83
3.2.17	Performing Deicing Test with Ice Cubes84
3.2.18	Performing Air Blower Tests on Formed Ice Cubes at Different Angles (0°, 5°, 10°, and 20°)84
3.2.19	Performing Salt Soaking Test85
3.2.20	Performing Freezing Time Test86
3.2.21	Performing Super-Cooled Water Test86
3.2.22	Performing Self-Cleaning Test86
4.	RESULTS AND DISCUSSION88
4.1	Contact Angle Measurement88
4.1.1	CA Results of All 27 Plasma-Treated SH-Coated AA 2024-T3 Samples88
4.1.2	CA Results of Four Best Plasma-Treated SH-Coated AA 2024-T3 Samples90
4.1.3	CA Results of Four Best Plasma-Treated SH-Coated AA 2024-T3 Samples after Tape Adhesive Test91
4.1.4	CA Results of Four Best Plasma-Treated SH-Coated AA 2024-T3 Samples Immersed in 3% 0.5M NaCl Solution for 30 Days92
4.1.5	CA Results of Four Best Plasma-Treated SH-Coated AA 2024-T3 Samples Immersed in DI Water for 30 Days94
4.1.6	Comparison of CA Results of Uncoated, SH-Coated, and Plasma-Treated SH-Coated AA 2024-T3 Samples96
4.2	Electrochemical Analysis Using Polarization Curves97
4.2.1	PC Results of Four Best Plasma-Treated SH-Coated AA 2024-T3 Samples97
4.2.2	PC Results of 8 Minutes High RF Level Plasma-Treated SH-Coated AA 2024-T3 Samples Immersed in 3% 0.5M NaCl Solution for 30 Days99
4.2.3	PC Results of 8 Minutes Medium RF Level Plasma-Treated SH-Coated AA 2024-T3 Samples Immersed in 3% 0.5M NaCl Solution for 30 Days100

TABLE OF CONTENTS (continued)

Chapter	Page
4.2.4	Corrosion Rate Behavior of Plasma-Treated SH-Coated AA 2024-T3 Samples Immersed in 3% 0.5M NaCl Solution for 30 Days102
4.2.5	PC Results of 8 Minutes High RF Level Plasma-Treated SH-Coated AA 2024-T3 Samples Immersed in DI Water for 30 Days104
4.2.6	PC Results of 8 Minutes Medium RF Level Plasma-Treated SH-Coated AA 2024-T3 Samples Immersed in DI Water for 30 Days106
4.2.7	Corrosion Rate Behavior of Plasma-Treated SH-Coated AA 2024-T3 Samples Immersed in DI Water for 30 Days108
4.2.8	Comparison of PC Results of Uncoated, SH-Coated, and Plasma-Treated SH-Coated AA 2024-T3 Samples110
4.3	Electrochemical Analysis Using Electrochemical Impedance Spectroscopy111
4.3.1	EIS Results of Four Best Plasma-Treated SH-Coated AA 2024-T3 Samples112
4.3.2	EIS Results of 8 Minutes High RF Level Plasma-Treated SH-Coated AA 2024-T3 Samples Immersed in 3% 0.5M NaCl Solution for 30 Days113
4.3.3	EIS Results of 8 Minutes Medium RF Level Plasma-Treated SH-Coated AA 2024-T3 Samples Immersed in 3% 0.5M NaCl Solution for 30 Days116
4.3.4	EIS Results of 8 Minutes High RF Level Plasma-Treated SH-Coated AA 2024-T3 Samples Immersed in DI Water for 30 Days118
4.3.5	EIS Results of 8 Minutes Medium RF Level Plasma-Treated SH-Coated AA 2024-T3 Samples Immersed in DI Water for 30 Days121
4.3.6	Comparison of EIS Results of Uncoated, SH-Coated, and Plasma-Treated SH-Coated AA 2024-T3 Samples123
4.4	FTIR Spectra Analysis of Plasma-Treated SH-Coated AA 2024-T3 Samples....125
4.5	Vickers Micro Hardness Number Measurement of Plasma-Treated SH-Coated AA 2024-T3 Samples127
4.6	Deicing Test Analysis128
4.6.1	Sliding Angle and Contact Angle Results of 8 Minutes Plasma-Treated SH-Coated AA 2024-T3 Sample after De-Icing Test.....129
4.6.2	Air Blower Test on 8 Minutes Plasma-Treated SH-Coated AA 2024-T3 Sample with Ice Cube.....131
4.6.3	Air Blower Test on 8 Minutes Plasma-Treated SH-Coated AA 2024-T3 Sample with Ice Cube on Surface at Different Angles (0°, 5°, 10°, and 20°).132
4.7	Self-Cleaning Ability of Plasma-Treated SH-Coated AA 2024-T3 Samples.....133
4.8	Salt Soaking Test Analysis134
4.8.1	Contact Angle Measurements of Four Best Plasma-Treated SH-Coated AA 2024-T3 Samples after Salt Soaking Test.....135

TABLE OF CONTENTS (continued)

Chapter	Page
4.8.2 Polarization Curves of Four Best Plasma-Treated SH-Coated AA 2024-T3 Samples after Salt Soaking Test.....	136
4.8.3 Electrochemical Impedance Spectroscopy of Four Best Plasma-Treated SH-Coated AA 2024-T3 Samples after Salt Soaking Test.....	137
4.9 Freezing Time Test of Plasma-Treated SH-Coated AA 2024-T3 Samples.....	139
4.10 Super-Cooled Water Test of Plasma-Treated SH-Coated AA 2024-T3 Samples.....	140
5. CONCLUSIONS.....	142
6. FUTURE WORK.....	144
REFERENCES	145

LIST OF TABLES

Table	Page
1. Common Electrical Elements	38
2. Surface Characterization of Hydrophilic, Hydrophobic, and Superhydrophobic Surfaces	41
3. Aluminum 2024-T3 Alloy Component Percentages	52
4. Initial Contact Angle Measurement for All 27 Plasma-Treated SH-Coated AA 2024-T3 Samples	88
5. Contact Angle Measurements of Four Best Plasma-Treated SH-Coated AA 2024-T3 Samples after each tape adhesive peel test	92
6. Contact Angle Measurements of Four Best Plasma-Treated SH-Coated AA 2024-T3 Samples Immersed in 3% 0.5M NaCl Solution for 30 Days	93
7. Contact Angle Measurements of Four Best Plasma-Treated SH-Coated AA 2024-T3 Samples Immersed in DI Water for 30 Days	94
8. Corrosion Rate Parameters of Four Best Plasma-Treated SH-Coated AA 2024-T3 Samples	98
9. Corrosion Rate Parameters of 8 Minutes High Plasma-Treated SH-Coated AA 2024-T3 Samples Immersed in 3% 0.5M NaCl Solution for 30 Days.....	100
10. Corrosion Rate Parameters of 8 Minutes Medium Plasma-Treated SH-Coated AA 2024-T3 Samples Immersed in 3% 0.5M NaCl Solution for 30 Days.....	101
11. Corrosion Rates of Plasma-Treated SH-Coated AA 2024-T3 Samples Immersed in 3% 0.5M NaCl Solution for 30 Days.....	103
12. Corrosion Rate Parameters of 8 Minutes High Plasma-Treated SH-Coated AA 2024-T3 Samples Immersed in DI Water for 30 Days	105
13. Corrosion Rate Parameters of 8 Minutes Medium Plasma-Treated SH-Coated AA 2024-T3 Samples Immersed in DI Water for 30 Days	107
14. Corrosion Rates of Plasma-Treated SH-Coated AA 2024-T3 Samples Immersed in DI Water for 30 Days.....	109

LIST OF TABLES (continued)

Table	Page
15. Comparison of Corrosion Rates Parameters of Uncoated, SH-Coated, and Plasma-Treated SH-Coated AA 2024-T3 Samples	111
16. Randles Cell Parameters of Plasma-Treated SH-Coated AA 2024-T3 Samples	113
17. Randles Cell Parameters of 8 Minutes High Plasma-Treated SH-Coated AA 2024-T3 Samples Immersed in 3% 0.5M NaCl Solution for 30 Days.....	115
18. Randles Cell Parameters of 8 Minutes Medium Plasma-Treated SH-Coated AA 2024-T3 Samples Immersed in 3% 0.5M NaCl Solution for 30 Days.....	117
19. Randles Cell Parameters of 8 Minutes High Plasma-Treated SH-Coated AA 2024-T3 Samples Immersed in DI Water for 30 Days	120
20. Randles Cell Parameters of 8 Minutes Medium Plasma-Treated SH-Coated AA 2024-T3 Samples Immersed in DI Water for 30 Days	122
21. Comparison of Randles Cell Parameters of Uncoated, SH-Coated, and Plasma-Treated SH-Coated AA 2024-T3 Samples	124
22. Vickers Microhardness Test Results of Uncoated and Plasma-Treated SH-Coated AA 2024-T3 Samples	128
23. Time Required for Removal of Ice Formed from 8 Minutes High Plasma-Treated SH-Coated AA 2024-T3 Sample	132
24. Self-Cleaning Test Results of Uncoated and Plasma-Treated SH-Coated AA 2024-T3 Samples	134
25. Corrosion Rate Parameters of Plasma-Treated SH-Coated AA 2024-T3 Samples after Salt Soaking Test	136
26. Randles Cell Parameters of Plasma-Treated SH-Coated AA 2024-T3 Samples after Salt Soaking Test	139

LIST OF FIGURES

Figure	Page
1. Example of corrosion in industry.....	1
2. Superhydrophobic coating surface showing water droplet bouncing like a ball	3
3. Aluminum alloy designation tree.....	5
4. Example of corrosion initiating attack on aluminum plate.....	8
5. Illustration of general attack corrosion	9
6. Mechanism of galvanic corrosion.....	11
7. Basic principles of corrosion	14
8. Illustration of aluminum corrosion mechanism	16
9. Example of corrosion failure: collapse of Lowe’s motor speedway bridge	17
10. Schematic diagram of galvanic anode system	19
11. Schematic diagram of impressed current protection system.....	20
12. Schematic diagram of corrosion inhibition mechanism.....	21
13. Schematic diagram of coating method.....	22
14. Graphical representation of hot dipping process	23
15. Illustration of how plasma surface treatment works and how plasma is generated.....	25
16. Changes in surface wetting and apparent area of contact after plasma treatment	26
17. Illustration of how plasma surface cleaning treatment works	26
18. (a) Typical i vs. η dependency based on Butler-Volmer equation; (b) red curves showing Tafel plot of net (anodic and cathodic) current; and (c) typical three-electrode setup for linear polarization method for measuring corrosion rate	29
19. Classic Tafel plot	30
20. Polarization (η) as a function of $\log i$	31

LIST OF FIGURES (continued)

Figure	Page
21. Nyquist plot with impedance vector	35
22. Simple equivalent circuit with one time constant	36
23. Bode plot with one time constant.....	37
24. Equivalent circuit of simplified Randles cell.....	39
25. Nyquist plot for simplified Randles cell circuit.....	39
26. Bode plot for simplified Randles cell circuit	40
27. Schematic representation of water droplet on hydrophilic, hydrophobic, and superhydrophobic surfaces.....	41
28. Schematic of contact angle and wettability of water drop placed on surfaces of different hydrophobicity	42
29. Drop on flat surface	43
30. Rough surface of liquid reservoir	45
31. Drop on rough surface	46
32. Schematic of water droplet in Wenzel state (left) and Cassie-Baxter state (right).....	46
33. Aluminum 2024-T3 alloy samples.....	51
34. Ultrasonic cleaner	52
35. Mini sprayer	53
36. Ultra Ever Dry SE bottom coat (left) and top coat (right)	54
37. Plasma cleaner	57
38. Industrial oven	58
39. Optical contact angle goniometer	59
40. Experimental setup for electrochemical corrosion test.....	61

LIST OF FIGURES (continued)

Figure	Page
41. Color code for sensors connections with Gamry cell	62
42. FTIR spectrometer	64
43. Vickers’s pyramidal indenter	65
44. Vickers microhardness test machine.....	65
45. Ice cube	66
46. Inclinator	67
47. Digital anemometer.....	67
48. Electric blower	68
49. Water sprayer	68
50. Twenty-seven samples plasma-treated with various RF levels and heat-treated at different temperatures	69
51. Dish liquid detergent, ethanol, and acetone	72
52. Application of bottom coat	74
53. Plasma surface cleaning treatment procedure.....	75
54. Application of top coat.....	76
55. Tape adhesion test procedure.....	77
56. Plasma-treated aluminum samples immersed in 3% 0.5M NaCl solution.....	78
57. Plasma-treated aluminum samples using Gamry reference 600 potentiostat	79
58. Plasma-treated aluminum sample within magnification close to 10M.....	83
59. Ice cube kept on top of plasma-treated aluminum sample.....	84
60. Electric air blower for removing ice	85

LIST OF FIGURES (continued)

Figure	Page
61. Plasma-treated aluminum samples immersed in glass beaker with 3% 0.5 M NaCl solution for 90 days	85
62. One drop of water applied to both plasma-treated aluminum sample and uncoated aluminum sample	86
63. Self-cleaning test method.....	87
64. Contact angle measurement for four best plasma-treated SH-coated AA 2024-T3 samples.....	90
65. Contact angle measurements of four best plasma-treated SH-coated AA 2024-T3 samples after each tape adhesive peel test	91
66. Contact angle measurements of plasma-treated SH-coated AA 2024-T3 samples immersed in 3% 0.5M NaCl solution for 30 days	94
67. Contact angle measurements of plasma-treated SH-coated AA 2024-T3 samples immersed in DI water for 30 days.....	96
68. Comparison of contact angle measurements of uncoated, SH-coated, and plasma-treated SH-coated AA 2024-T3 samples	97
69. Tafel curves of four best plasma-treated SH-coated AA 2024-T3 samples	98
70. Tafel curves of 8 minutes high plasma-treated SH-coated AA 2024-T3 samples immersed in 3% 0.5M NaCl solution for 30 days	99
71. Tafel curves of 8 minutes medium plasma-treated SH-coated AA 2024-T3 samples immersed in 3% 0.5M NaCl solution for 30 days.....	101
72. Comparison of corrosion rates of plasma-treated SH-coated AA 2024-T3 samples immersed in 3% 0.5M NaCl solution for 30 days	103
73. Tafel curves of 8 minutes high plasma-treated SH-coated AA 2024-T3 samples immersed in DI water for 30 days.....	105
74. Tafel curves of 8 minutes medium plasma-treated SH-coated AA 2024-T3 samples immersed in DI water for 30 days.....	107

LIST OF FIGURES (continued)

Figure	Page
75. Comparison of corrosion rates of plasma-treated SH-coated AA 2024-T3 samples immersed in DI water for 30 days.....	109
76. Tafel curves of uncoated, SH-coated, plasma-treated SH-coated AA 2024-T3 samples.....	110
77. Nyquist plots of plasma-treated SH-coated AA 2024-T3 samples.....	112
78. Bode plots of plasma-treated SH-coated AA 2024-T3 samples	113
79. Nyquist plots of 8 minutes high plasma-treated SH-coated AA 2024-T3 samples immersed in 3% 0.5M NaCl solution for 30 days	114
80. Bode plots of 8 minutes high plasma-treated SH-coated AA 2024-T3 samples immersed in 3% 0.5M NaCl solution for 30 days	115
81. Nyquist plots of 8 minutes medium plasma-treated SH-coated AA 2024-T3 samples immersed in 3% 0.5M NaCl solution for 30 days	117
82. Bode plots of 8 minutes medium plasma-treated SH-coated AA 2024-T3 samples immersed in 3% 0.5M NaCl solution for 30 days	118
83. Nyquist plots of 8 minutes high plasma-treated SH-coated AA 2024-T3 samples immersed in DI water for 30 days.....	119
84. Bode plots of 8 minutes high plasma-treated SH-coated AA 2024-T3 sample immersed in DI water for 30 days.....	120
85. Nyquist plots of 8 minutes medium plasma-treated SH-coated AA 2024-T3 samples immersed in DI water for 30 days.....	122
86. Bode plots of 8 minutes medium plasma-treated SH-coated AA 2024-T3 samples immersed in DI water for 30 days.....	123
87. Comparison of Nyquist plots of uncoated, SH-coated, and plasma-treated SH-coated AA 2024-T3 samples.....	124
88. Comparison of Bode plots of uncoated, SH-coated, and plasma-treated SH-coated AA 2024-T3 samples	125

LIST OF FIGURES (continued)

Figure	Page
89. FTIR spectra analysis of plasma-treated SH-coated AA 2024-T3 samples and only SH-coated sample for 0 days	126
90. FTIR spectra analysis of plasma-treated SH-coated AA 2024-T3 samples after 30 days	126
91. Vickers microhardness test results of uncoated and plasma-treated SH-coated AA 2024-T3 samples	128
92. Sliding angle measurements of 8 minutes high plasma-treated SH-coated AA 2024-T3 sample after deicing test	130
93. Contact angle measurements of 8 minutes high plasma-treated SH-coated AA 2024-T3 sample after deicing test	130
94. Contact angle measurements of 8 minutes high plasma-treated SH-coated AA 2024-T3 sample after air blower test	131
95. Contact angle measurements of 8 minutes high plasma-treated SH-coated AA 2024-T3 sample after air blower test at different tilted angles	133
96. Self-cleaning results of uncoated and plasma-treated SH-coated AA 2024-T3 samples.....	134
97. Comparison of contact angle measurement of four best plasma-treated SH-coated AA 2024-T3 samples after salt soaking test	135
98. Comparison of Tafel curves of four best plasma-treated SH-coated AA 2024-T3 samples after salt soaking test.....	137
99. Comparison of Nyquist plots of four best plasma-treated SH-coated AA 2024-T3 samples after salt soaking test.....	138
100. Comparison of Bode plots of four best plasma-treated SH-coated AA 2024-T3 samples after salt soaking test.....	138
101. Water droplet on plasma-treated SH-coated AA 2024-T3 sample (left) and uncoated AA 2024-T3 sample (right)	139
102. Frozen water droplet on plasma-treated SH-coated AA 2024-T3 sample (left) and uncoated AA 2024-T3 sample (right).....	140

LIST OF FIGURES (continued)

Figure	Page
103. Super-cooled water test on plasma-treated SH-coated AA 2024-T3 sample (left) and uncoated AA 2024-T3 sample (right)	141

LIST OF ABBREVIATIONS

AA	Aluminum Alloy
AC	Alternate Current
ASTM	American Standard for Testing Materials
ATR	Attenuated Total Reflectance
b_a	Tafel Slope of Anodic Polarization
b_c	Tafel Slope of Cathodic Polarization
C	Capacitance
C_{dl}	Double Layer Capacitance
CA	Contact Angle
cfm	Cubic Feet per Minute
CPR	Corrosion Penetration Rate
Cu	Copper
DI	Deionized
E	Electrode Potential
E_{corr}	Corrosion Potential
EC	Electrochemical
EIS	Electrochemical Impedance Spectroscopy
FTIR	Fourier Transform Infrared
HV	Vickers Hardness Number
I_a	Anodic Current
I_c	Cathodic Current
I_o	Current (Density)

LIST OF ABBREVIATIONS (continued)

I_{corr}	Corrosion Current
LG	Liquid-Gas
LW	Lifshitz-van der Waals
M	Molar Concentration
mph	Miles per Hour
mpy	Mills per Year
NaCl	Sodium Chloride
OH	Hydroxide
PC	Polarization Curve
pH	Potential Hydrogen
PVC	Polyvinyl Chloride
R	Resistance
r	Roughness of Textured Solid
R_{ct}	Charge Transfer Resistance
RF	Radio Frequency
R_{p}	Polarization Resistance
R_{s}	Solution Resistance
SG	Solid-Gas
SH	Superhydrophobic
SL	Solid-Liquid
Z	Impedance
Zn	Zinc

LIST OF SYMBOLS

θ	Angle
Φ_s	Area Section of Solid Surface
$^{\circ}\text{C}$	Degree Celsius
η	Over Potential
ϕ	Phase Shift
ω	Radial Frequency
γ	Surface Tension

CHAPTER 1

INTRODUCTION

1.1 Background

The proper functioning of machines and appropriateness of materials are essential to accomplishing various daily objectives in the contemporary world. The naturally recurring, most significant deterrent to the maintenance of these machines and materials is corrosion. The primary catalyst in the corrosive process is water. Many of the operations and applications of the mentioned entities, a humid or wet environment, the severity of the need to evolve anti-corrosion procedures and techniques cannot be understated. Figure 1 shows an example of corrosion in industry [1].



Figure 1. Example of corrosion in industry [1].

The prevalence of textbook methods for preventing corrosion, such as galvanization, is increasingly diminishing. This decrease in utilization of time-tested methods is attributed to the operability of advanced technological applications in conditions that are conducive to initiation of the corrosive process. A few revolutionary corrosion-prevention methodologies have been

periodically devised in order to be compatible with technological progression. The two preventive methodologies at the forefront of this innovative process involve the fabrication of superhydrophobic (SH) and superhydrophilic surfaces.

As the terminology suggests, superhydrophobic surfaces are those that are averse to or resist the wetting property of water. SH surfaces have gained popularity in the development of anti-wetting textile fabrics [2]. Here, the fibers constituting such fabrics are coated with chemical compounds containing nanoparticles, the properties of which are instrumental in the provision of critical contact angles, which make the water droplets wholly and smoothly slide off the contact surface immediately, thus ensuring dryness [2].

On the other end of the spectrum, superhydrophilic surfaces are functionally the opposite of superhydrophobic surfaces but are utilized for the same end goal of maintaining surface dryness [3]. Superhydrophilic coatings are also the result of a series of chemical alterations, but unlike SH coatings, they entirely absorb and retain the water in order to achieve surface dryness. Although this is a robust approach to maintaining surface dryness, its application can be contradictory to its implementation. For instance, surface dryness is required for electrical devices such as cell phones, which are often exposed to wet, humid conditions. If a superhydrophilic coat was to be applied to maintain dryness, then the risk of retained water permeating into the internal components and subsequent malfunction cannot be ignored.

1.2 Motivation and Objective

It is hypothesized that proper surface treatment improves the coating performance against various environmental conditions. The broad-based concurrence on a superhydrophobic surface being the most efficient resistor to corrosion poses a new question: What method produces the best superhydrophobic surface? This question is the prime motivation behind this research.

When we examine established techniques for achieving SH qualities, one of the more prominent is by spraying a coat that contains a liquid interface [4]. The liquid interface possesses chemically embedded molecules that induce a reduction in the wetted area fraction and consequently in the heat transfer rate, thereby allowing for air trapped between the liquid interface and the material surface to act as a perfectly smooth pathway for the ejection of water droplets [4]. Figure 2 shows a superhydrophobic coating surface, which causes the water droplet to bounce like a ball [5].



Figure 2: Superhydrophobic coating surface showing water droplet bouncing like a ball [5].

Further studies based on mathematical and analytical modeling of the behavior demonstrated by this method reveal that the SH effect achieved by the layers of coats held together by adhesive are constrained by the time variable [6], which implies that the durability of this methodology is questionable. Doubts about durability are further enhanced when considering environmental surroundings that can alter essential variables, such as contact angles [6].

An alternate technique that improves the durability of the superhydrophobic surface has been advocated [7]. It involves chemical alterations at a nanolevel that result in self-repairing hydrophobic coatings. During its manufacturing phase the coat is injected with nanosized

potential hydrogen (pH) capsules, which can chemically contemplate the degradation of the SH surface as an acidic situation, and hence, courtesy of their chemical properties, release alkaline compounds, which accomplish regeneration of the water bonding and consequently that of the SH coating [7].

The regeneration method embodies high chemical complexity. The interference of variation assumed in environmental factors such as lighting conditions, heat, humidity, and pressure has not been quantified either, due to the effects of acid/base chemical reactions and their residual salts, with vital entities about practical applications such as human tissue and metallic surfaces, have not been identified. This leaves the proposed solution with a void. An answer that advocates for filling the vacuum of practicality, and consequently establishes itself through scientific means of trial and error as the optimum solution, is the multilayered SH coating bonded together with other iterations of plasma and heat treatment. The realization of this coating and its achievement of the benchmark for prolonging the durability of the SH effect is the primary objective of this research.

CHAPTER 2

LITERATURE REVIEW

2.1 Metals and Alloys in Manufacturing Industry

2.1.1 Aluminum 2024-T3 Alloys

Aluminum alloys (AAs) have been the primary metal substances used in many industries because they started changing from wood in the late 1920s. Despite the fact that in the future the position of aluminum may possibly dwindle, mainly through the increasing use of composite substances, high-strength aluminum alloys are and will continue to be employed as significant industrial materials. Aluminum is attractive because it is an exceedingly low-cost and light-weight metal that can be heat treated to reasonably high-strength levels, and it is one of the most effortlessly fabricated of the high-performance materials, which correlates directly with lower expenses [8]. Figure 3 illustrates the designation tree of the aluminum alloy [9].

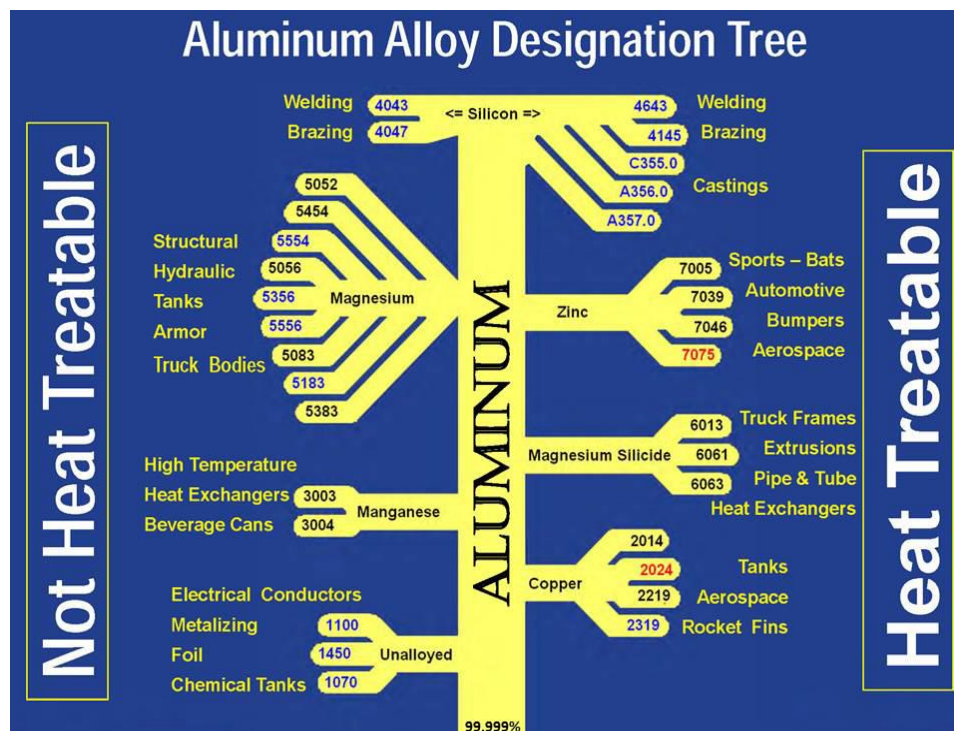


Figure 3. Aluminum alloy designation tree [9].

AAs are recognized through a four-digit number system. The first digit represents the alloy group and the other digits indicate the alloys that are present in the mix. In an alloy, the usage of copper (Cu) and zinc (Zn) indicates that the aluminum can modify its specifications whereby the alloy can be both hardened and softened through the usage of heat. The ensuing temper designation is indicated using a letter-number combination following the alloy numbers. The most common temper designations are T3 and T6. The T3 alloy is solution heat-treated and cold-worked through the flattening method. The T6 alloy is solution heat-treated and artificially aged. Each alloy has its own properties that rely on the composition of the alloying factors. This research employed Aluminum 2024-T3 alloy, which has added approximately 93.5% aluminum, 4.5% copper, 0.6% manganese, 1.5% magnesium, 0.5% silicon, 0.5% iron, 0.25% zinc, and 0.15% titanium [10]. One of the purposes here was to select the Aluminum 2024-T3 alloy for its mechanical properties. It is the most common of the high-strength aluminum alloys. It is high-grade aircraft satisfactory, which is lightweight, strong, and exceptionally corrosion resistant. However, it must be dealt with properly because even aluminum cannot escape from corrosion and will corrode quickly after cleaning, so any treatment should be done rapidly to prevent corrosion from becoming trapped beneath the base paint.

2.1.2 Industrial Uses of Aluminum 2024-T3 Alloys

Aluminum is used abundantly in the contemporary world. AAs have several technical benefits, which have made them one of the most useful alloy structures. They have a silvery-white look and show many unusual properties. They have extensive applications in distinct domains, such as transport, aircraft, home decor and add-ons, constructing and creation, and so on. No other metal can be utilized in so many different ways as aluminum. It has a few properties that have made it feasible for many valuable uses and applications in numerous fields [11].

Aluminum and AAs have been used as aerospace constituents, particularly in commercial airplanes because of their extreme strength/stiffness-to-weight ratio, mechanical functionalities, and corrosion resistance. Corrosion resistance results from the passive oxide film that clearly forms on aluminum alloys and significantly reduces the rate of corrosion. However, when exposed to aggressive environments, aluminum and its alloys react with oxygen and chloride ions to form complex interfaces. The passive oxide film is at risk of localized breakdown, leading to the loss of the underlying aluminum metal. If the localized attack takes place at an open surface, then it results in pitting corrosion. These corrosion forms can cause a structural breakdown appearing as sites of crack initiation [12].

2.2 Definition of Corrosion

Corrosion is a natural and expensive destructive procedure, like earthquakes, tornados, floods, and volcanic eruptions, with one arbitrary distinction in that we can only be a silent spectator to the above-stated system of destruction, but corrosion can be prevented or at least managed. While metal is subject to corrosion, its properties are modified because of the unintentional, however damaging, response with the exposed environment. The corrosion process is continuous and irreversible [13]. It includes a set of electrochemical (EC) redox reactions. Consequently, the metal is oxidized to a corrosion product at anodic sites, and some parts of metals are decreased at cathodic sites. Due to the EC nature of most corrosion approaches, EC methods are beneficial tools for analyzing corrosion. More typically, EC techniques can be used to measure the kinetics of corrosion rates in particular environments and additionally measure or manipulate the oxidizing power of the surroundings. Figure 4 displays an example of corrosion initiating an attack on an aluminum plate [14].



Figure 4. Example of corrosion initiating attack on aluminum plate [14].

Do all metals corrode? Yes, all metals can corrode. A few, like pure iron, corrode quickly. Stainless steel, which combines iron and different alloys, is slower to corrode and consequently is used more often. A small group of metals referred to as noble metals are much less reactive than others and therefore seldom corrode. In fact, they are the most effective metals found in nature in their pure form. Noble metals are often very precious. They consist of copper, palladium, silver, platinum, and gold. The same amount of energy needed to extract metals from their minerals is emitted in the course of the chemical reactions that produce corrosion [15].

The most extensively used aircraft AA is Aluminum 2024-T3 alloy. Many researchers [16] have performed a tremendous amount of work to recognize the corrosion mechanism of the Aluminum 2024-T3 alloy. The heterogeneous distribution of the Cu phases within the alloy is the reason for the low resistance of the alloy. These second-phase particles provide additional mechanical strength to the aluminum matrix; however, they are undesirable for corrosion resistance in the alloy. Pitting is the principal form of corrosion, but other forms of corrosion such as intergranular and stress corrosion can also occur [17].

2.2.1 Classification of Corrosion

Corrosion can be categorized into distinct categories primarily based on the material, environment, or morphology of the damage it causes. A discussion of the eight distinctive modes of corrosion follows.

2.2.1.1 General Attack Corrosion

General attack corrosion is the most common type of corrosion and occurs from a chemical or electrochemical response that results in the deterioration of the entire exposed surface of a metal at approximately the same rate. An example of general attack corrosion is shown in Figure 5. The outcome of general attack corrosion within the metal is that the metal becomes thinner and the appearance of the surface is altered. This corrosion typically brings on failure by reducing the mechanical strength of additives or by reducing the wall thickness until leaking results severe [18]. In the end, the metal deteriorates to the point factor of failure. General attack corrosion accounts for the most amount of metal destruction; however, it is a secure form of corrosion because it is predictable, workable, and frequently preventable [19].



Figure 5. Illustration of general attack corrosion [20].

2.2.1.2 Pitting Corrosion

Pitting corrosion occurs when a small hole, or cavity, forms within the metal, generally because of depassivation of a small region. It usually happens at flaws in coatings implemented to prevent corrosion of the underlying metal; however, pitting corrosion also occurs in metals that can withstand corrosion through the formation of a local oxide, hydroxide, or salt film. The small region turns anodic, while part of the remaining metal turns cathodic, thereby generating a localized galvanic reaction. The deterioration of this small region penetrates the metal and may lead to failure [21]. This form of corrosion is frequently difficult to discover because it is noticeably small and may be covered or hidden by corrosion-produced compounds. The time required to provoke pitting depends on the temperature and composition of the environment. As soon as pitting is initiated, the corrosion rate at the bottom of a pit can be numerous orders of magnitude more than that outside the pit, and in this way, pitting can cause perforation of storage bottles, etc. Alternatively, it can provoke cracks that propagate to failure by way of different mechanisms [22].

2.2.1.3 Crevice Corrosion

Crevice corrosion takes place in a particular region, the environment of which does not mix freely with the bulk environment. The chemistry of the environment in these places can fluctuate substantially from that of the bulk environment, and this distinction can bring about the corrosive attack. This sort of corrosion is often related to a stagnant micro-environment, like that observed beneath gaskets, joints, washers, and clamps, and additionally could result in the initiation of cracks that propagate to failure through different mechanisms. Acidic surroundings or a reduction of oxygen in a crevice also can cause crevice corrosion. Much like pitting corrosion, an extended incubation period may be required to initiate this corrosion; however, as

soon as it starts, this corrosion can increase at rates that might be orders of significance greater than rates outside the crevice [23].

2.2.1.4 Galvanic Corrosion

Galvanic corrosion takes place when distinct metals are placed together in a corrosive electrolyte. Distinct metals have different chemical properties, and different alloys with distinct chemical compositions can have various chemical and EC properties within the same environment [24]. Joining dissimilar metals in a way such that an electrical circuit is completed through the joint and the environment will bring about an increasing rate of corrosion of the more active metal and a decreasing rate of corrosion of the more noble metal. A galvanic couple forms between the two metals, in which one metal turns into the anode and the other the cathode. The anode corrodes and deteriorates more quickly than it would if it was alone, even as the cathode deteriorates more slowly than it would otherwise. This mechanism is clarified in Figure 6 [26]. The extent of the change depends on several factors consisting of the ratio of the regions of every alloy exposed to the environment, the potential difference between the alloys, the electrical resistivity of the joint, and the conductivity of the environment [25].

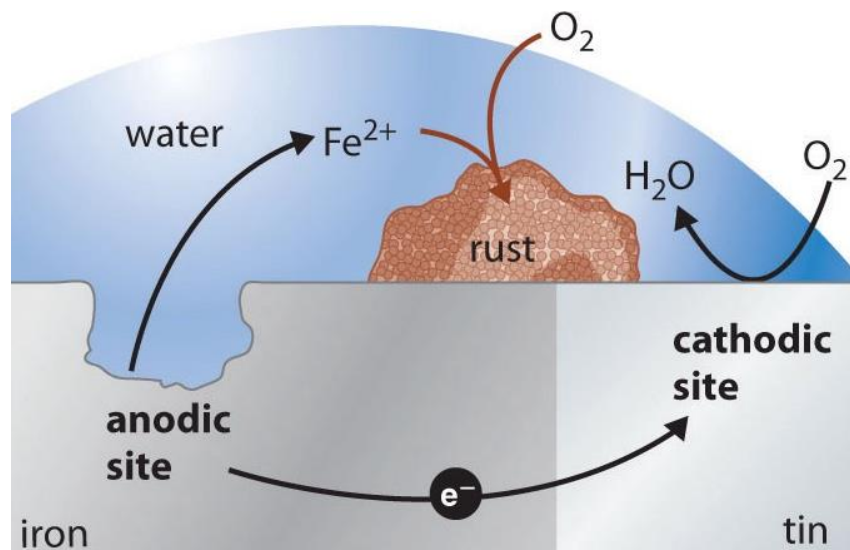


Figure 6. Mechanism of galvanic corrosion [26].

2.2.1.5 Environmentally Induced Cracking Corrosion

Environmental induced cracking is a corrosion technique that could result from a combination of chemically reactive environmental conditions affecting the metal. Exposure to aqueous solutions, natural solvents, liquid metals, solid metals, and gases has been observed to result in failure of this kind. Relying on the environment and the type of loading, this form of corrosion has many distinctive names, including stress corrosion cracking, chloride stress cracking, hydrogen embrittlement, liquid brittle embrittlement, and substantial metal embrittlement. However, all of them encompass crack propagation precipitated through exposure to an environment. The environments that cause this type of corrosion are not usually very aggressive, and this mechanism of failure could cause unexpected loss of agent or prevent the right operation of valves [27].

2.2.1.6 Intergranular Corrosion

Intergranular corrosion is another kind of chemical attack that occurs at the grain boundaries of a metal. This type of corrosion frequently takes place because of impurities in the metal, which tend to be more concentrated close to the grain boundaries which may be more intense in the course of the solidification process [28]. Because of this, certain metal environment combinations can bring about fast corrosion of the region among the crystals. While intergranular corrosion occurs, the surface of the material can appear as being unattacked. However, the mechanical strength of the alloy can worsen slowly over time or can occur quickly until the materials is damaged beneath any applied load or until individual grains begin to release and the material falls apart [29].

2.2.1.7 De-Alloying Corrosion

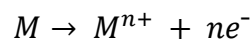
Distinct metals have distinctive chemical activities, whereby one metal in an alloy may be selectively eliminated from the surface. This selective leaching of an alloying element can result in the surface becoming de-alloyed. In a few instances, this de-alloyed layer is not restricted to the surface and grows into a solid that inflicts a severe loss of mechanical strength. Similarly to reducing the strength of any aspect, de-alloyed layers are porous, and de-alloying also may cause damage to the agent from a metallic storage container in the laboratory [30].

2.2.1.8 Erosion-Assisted Corrosion

Mixing or stirring of a solution can increase the rate of corrosion, either by increasing the rate of transport to the surface, or by mechanically destroying or eliminating surface films that could protect the underlying metal from attack. An increase in the rate of corrosion because of the relative motion of the environment is referred to as erosion-assisted corrosion. Typically, the relative motion of agents within metallic storage and distribution structures is fairly low, and in the course of deployment, erosion-assisted corrosion may additionally occur within nozzles [31].

2.2.2 Mechanism of Corrosion

Corrosion is described as the continuous destruction or deterioration of a material with the aid of a chemical or EC attack. The corrosion reaction is referred to as electrochemical because the overall corrosion reaction may be split into two partial reactions. Figure 7 shows the basic principles of corrosion [34]. The anodic or oxidation reaction entails the metal going into dissolution by using releasing electrons [32].



where M the atom is on the metal surface, M^{n+} is the metal oxidized to metal ions, and ne^{-} is the number of electrons produced throughout the anodic process. The consumption of these

electrons from the anodic reaction indicates a reduction or cathodic reaction. Numerous cathodic reactions occur in metal corrosion, a few of the more common being as follows [33]:

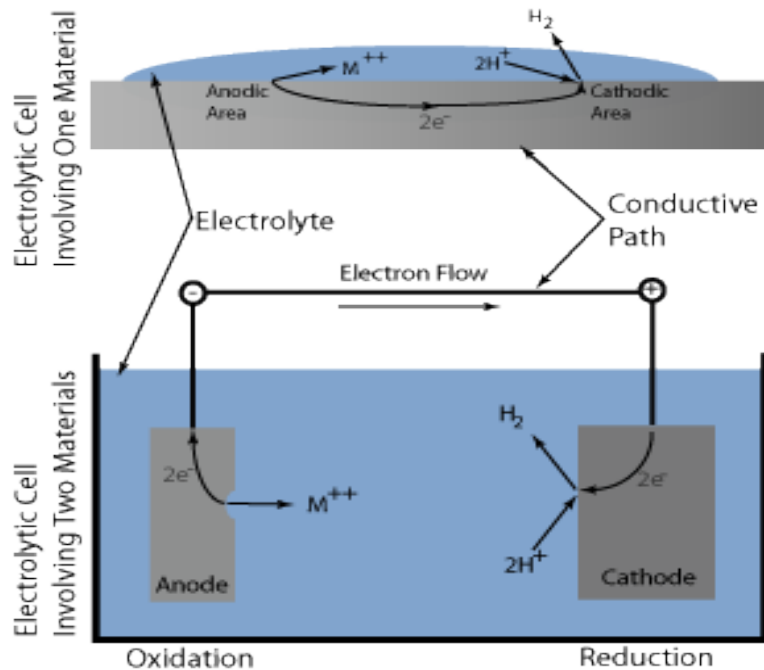
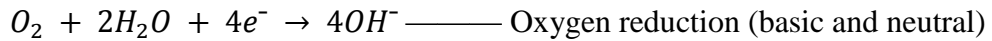
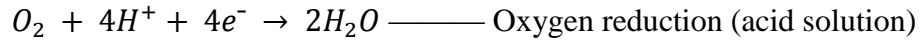
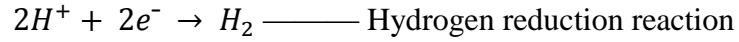
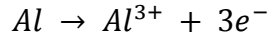


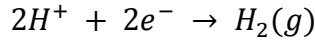
Figure 7. Basic principles of corrosion [34].

The hydrogen reduction reaction occurs when a metal is exposed to an acid medium, whereas the oxygen reduction reaction is most common in aqueous solutions, which is generated by contact with air. The metal ion reduction reaction is not often observed in chemical media. The anodic and cathodic reactions must occur concurrently on the metal surface. The amount of electrons produced through the anodic reaction is consumed by using the cathodic reaction, and consequently, charge neutrality is maintained [35].

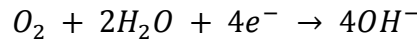
Moving on to the corrosion mechanism of an aluminum alloy, when an AA sample is exposed to a solution of sodium chloride (NaCl), the corrosion of the metal leads to oxidation of the AA as the anodic reaction [36]:



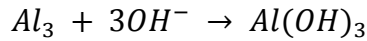
Because of the acidity on the anodic sites, hydrogen evolution occurs as a secondary cathodic reaction (within the pit):



Because the NaCl solution consists of a certain amount of dissolved oxygen, the primary cathodic reaction on the cathodic sites (outside the pit) could be the reduction of oxygen:



Because of the cathodic reactions, the concentration of hydroxide ions will increase, so the local pH becomes more alkaline, and the following chemical reaction takes place:



$Al(OH)_3$ would be further transformed into Al_2O_3 by



It has been mentioned that the presence of chloride ions in the environment results in the pitting corrosion of AA. The role of Cl^{-} in the pitting processes and its interaction with the passive film have been studied significantly, and models have evolved to demonstrate this pitting corrosion [37, 38]. According to the factor defect model, chloride ions might compete with cation vacancies and replace oxygen within the oxide film to form metal chlorine, thus resulting in degradation of the oxide film and the initiation of pitting [39]. Figure 8 illustrates the mechanism of aluminum corrosion [40].

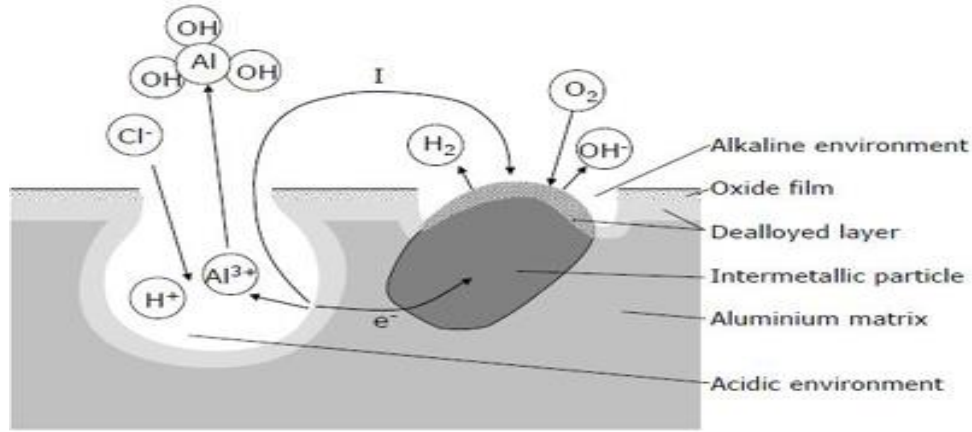
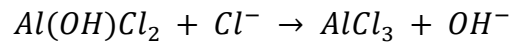
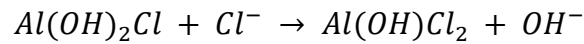
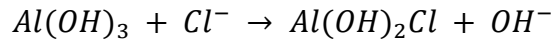


Figure 8. Illustration of aluminum corrosion mechanism [40].

The aluminum chloride recognized in this work proves that chloride ions will react with cation, including of Al^{3+} , to form the chloride-containing compound. The following mechanisms are proposed to explain the formation of aluminum chloride [41]:



Therefore, the corrosion products formed on aluminum alloy in a close-to-neutral pH NaCl solution usually encompass $Al(OH)_3$, Al_2O_3 , and $AlCl_3$, as recognized.

2.2.3 Importance of Corrosion Mitigation

Corrosion studies have developed significantly because of the increasing awareness of the need to preserve the world's metal resources. Corrosion failures can be severe, as shown in Figure 9 with the collapse of the Lowe's motor speedway bridge [42]. The reasons for the importance of corrosion mitigation studies are as follows:

- Aggregated utilization of metals in most areas of the technical terminology.
- Use of rare and costly metals, the protection of which necessitates special precautions.

- Use of the latest excessive-strength alloys, which are more prone to certain kinds of corrosive attack.
- Growing pollution of air and water resulting in more corrosive surroundings.
- Severe protection standards for working devices, which can also fail in a catastrophic way due to corrosion [18].



Figure 9. Example of corrosion failure: collapse of Lowe's motor speedway bridge [42].

2.3 Corrosion Mitigation Methods

Corrosion is the damage of any material because of its reaction with the environment and which causes destructive consequences on material and the environment. In certainly all situations, corrosion can be controlled, slowed, or even stopped through the use of proper techniques. In some cases, corrosion mitigation can depend on the circumstances of the metal that is corroded. Corrosion mitigation techniques can be categorized as follows:

2.3.1 Environmental Modification

Corrosion occurs as the result of chemical interactions among metals and gases in the surrounding environment. Metal deterioration can be decreased immediately by disposing of the

metal form or changing the type of environment. This may be as simple as restricting the metal's contact with rain or seawater by storing the metal materials interiorly or by directly manipulation the environment affecting the metal. Techniques to reduce the sulfur, chlorine, or oxygen content in the surrounding environment can restrict the speed of metal corrosion. As an example, feed water for water boilers could be handled with softeners or other chemical media to alter the hardness, alkalinity, or oxygen content with the purpose of reducing corrosion on the interior of the unit [43].

2.3.2 Cathodic Protection

Galvanic corrosion takes place when two distinct metals are located together in a corrosive electrolyte. This is a common problem for metals submerged collectively in seawater; however, this also can occur when two distinctive metals are closely immersed in wet soils. This is why galvanic corrosion regularly attacks ship hulls, offshore rigs, and oil and pipelines [44]. Cathodic protection works by changing the undesirable anodic sites, which are active on a metal's surface, to cathodic sites, which might be passive through the application of an opposing current. This opposing current supplies free electrons and forces local anodes to be polarized to the potential of the local cathodes [45]. Cathodic protection can be applied using two methods: galvanic anode system and impressed current protection system.

2.3.2.1 Galvanic Anode System

The galvanic anode system method is like the introduction of galvanic anodes, which uses metal anodes that are added to the electrolytic environment in order to sacrifice their life by the way of corrosion for the purpose of protecting the cathode. Sacrificial anodes are typically made of zinc, aluminum, or magnesium—metals that have the most negative electron potential. With this technique, metallic ions flow from the anode to the cathode, which leads the anode to

corrode faster it would otherwise. As a result, the anode is often replaced [46], as shown in Figure 10 [47].

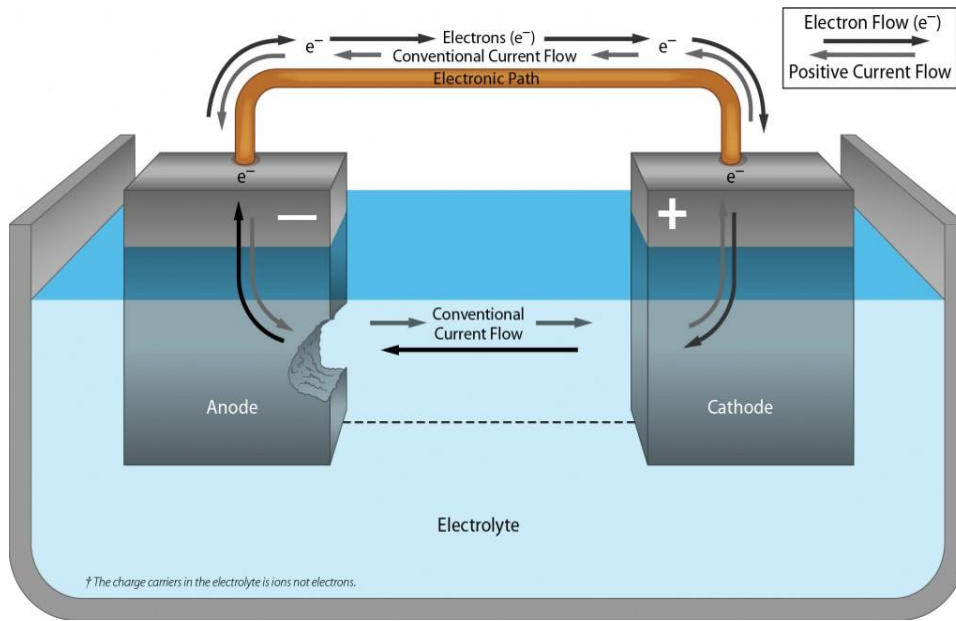


Figure 10. Schematic diagram of galvanic anode system [47].

2.3.2.2 Impressed Current Protection System

The impressed current protection system method of cathodic protection is frequently used to protect buried pipelines and ship hulls, which calls for an alternative source of direct electrical current to be supplied to the electrolyte. The negative terminal of the current source is attached to the metal, while the positive terminal is connected to an auxiliary anode that is delivered to complete the electric circuit, as shown in Figure 11 [47]. In contrast to the first method (galvanic anode system), within the impressed current protection system, the auxiliary anode is not sacrificed [48].

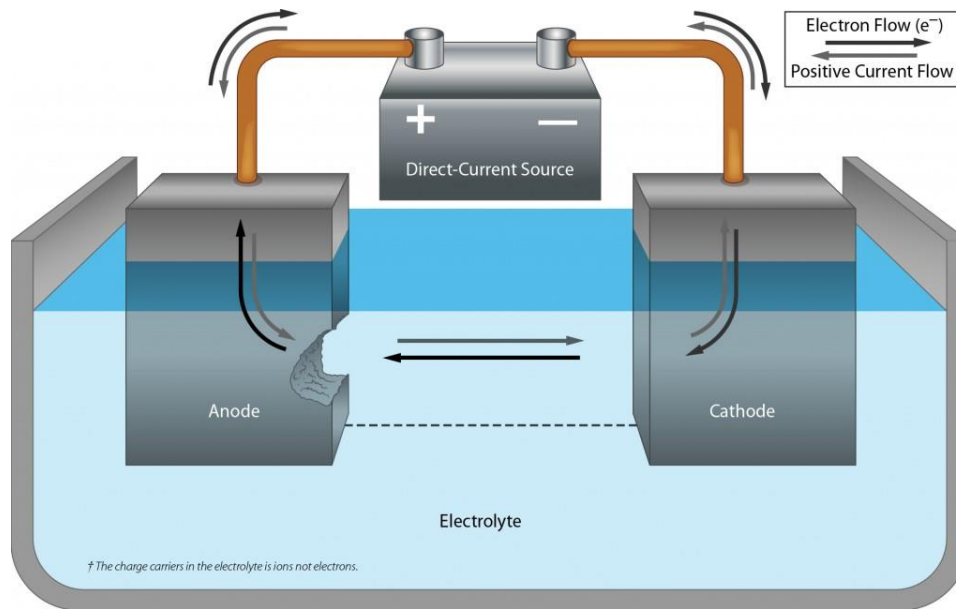


Figure 11. Schematic diagram of impressed current protection system [47].

2.3.3 Metal Selection

No metal is resistant to corrosion in all environments; however, through tracking and expertise, environmental situations are the reason for corrosion, and modifications to the form of metal being used in an environment can result in an extensive reduction in corrosion. Metal corrosion resistance information can be utilized in combination with facts on the environmental conditions in order to make decisions concerning the suitability of each metal. Improvement in the latest alloys, which are designed to protect against corrosion in particular environments, is continually being investigated. Hastelloy nickel alloys, Nirosta steels, and titanium metal alloys are all examples of alloys designed for corrosion prevention [49].

2.3.4 Corrosion Inhibitors

Corrosion inhibitors are substances that respond with the metal's surface or the environmental gases that impose corrosion, thereby interrupting the chemical reaction that results in corrosion. Inhibitors can work by way of adsorbing themselves on the metal's surface and forming a protective film. These chemical compounds can be implemented as a solution or as a

protective coating through dispersion techniques. The inhibitors method of slowing corrosion relies upon converting the anodic or cathodic polarization channel, decreasing the flow of ions to the metal's surface, and growing the electrical resistance of the metal's surface. Figure 12 shows the schematic diagram of the corrosion inhibition mechanism [50].

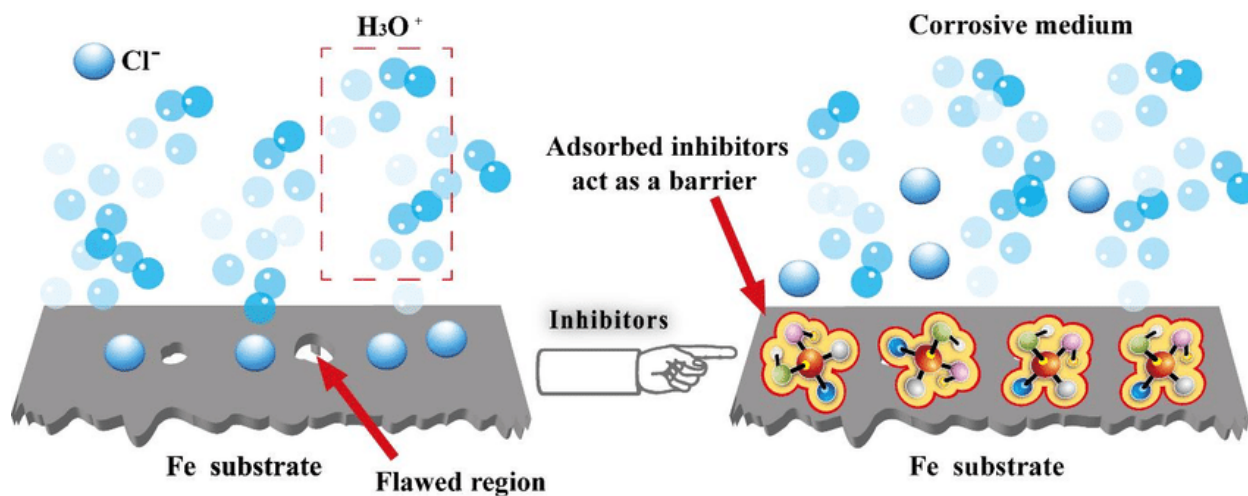


Figure 12. Schematic diagram of corrosion inhibition mechanism [50].

The primary industries that use corrosion inhibitors are in petroleum refining, oil and gas exploration, chemical production, and water treatment facilities. The advantage of corrosion inhibitors is that they can be implemented in-situ to metals as a corrective motion to counter unexpected corrosion [51, 52].

2.3.5 Coatings

In any civilized society, coatings are everywhere. Coatings are found on walls, refrigerators, cabinets, and furnishings. Much less manifestly, coatings are found on the wires of electrical motors, printed circuits, internal television sets, and compact disks, as well as inside vehicles, underneath the hood, and in additives of the automotive stereo and computer systems [53]. Paints and different natural coatings are used to protect metals from the degradative impact

of environmental gasses. Coatings are grouped by the type of polymer employed. Figure 13 shows a schematic diagram of the coating method [54].

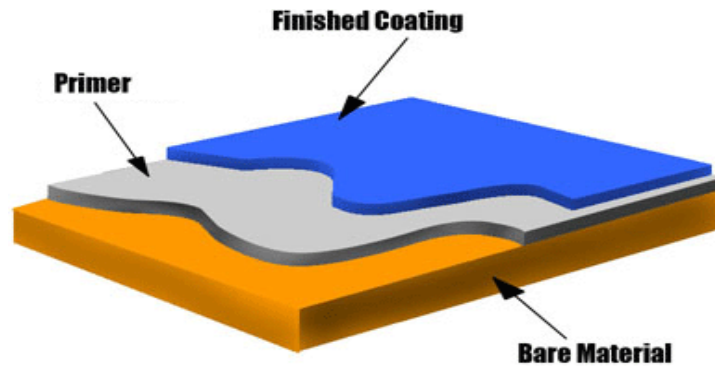


Figure 13. Schematic diagram of coating method [54].

Common organic type of coatings consist of alkyd and epoxy ester coatings that, when air dried, promote cross-link oxidation; component urethane coatings, acrylic coatings; epoxy polymer radiation curable coatings; vinyl, acrylic or styrene polymer aggregated latex coatings, water-soluble coatings; excessive stable coatings; and powder coatings [55].

2.3.6 Plating

Plating can be applied to inhibit corrosion as well as provide aesthetic, decorative finishes. The four common types of plating: electroplating, mechanical plating, electroless, and hot dipping.

2.3.6.1 Electroplating

In electroplating, a thin layer of metal, often nickel, tin, or chromium, is deposited on the substrate metal in an electrolytic bath. The electrolyte typically includes a water solution containing salts of the metal to be deposited [56].

2.3.6.2 Mechanical Plating

In mechanical plating, a metal powder can be bloodlessly welded to a substrate metal by way of tumbling the element, together with the powder and glass beads, with an aqueous

solution. Mechanical plating is regularly used to adhere zinc or cadmium to small metal parts [56].

2.3.6.3 Electroless Plating

In this non-electric plating technique, a coating metal, consisting of cobalt or nickel, is deposited on the substrate metal by means of a chemical reaction.

2.3.6.4 Hot Dipping

In the hot dipping method, as shown in Figure 14 [58], the substrate metal is dipped in a molten bath, which is the protective layer, thereby coating it with a thin metal layer that adheres to the substrate metal [57].

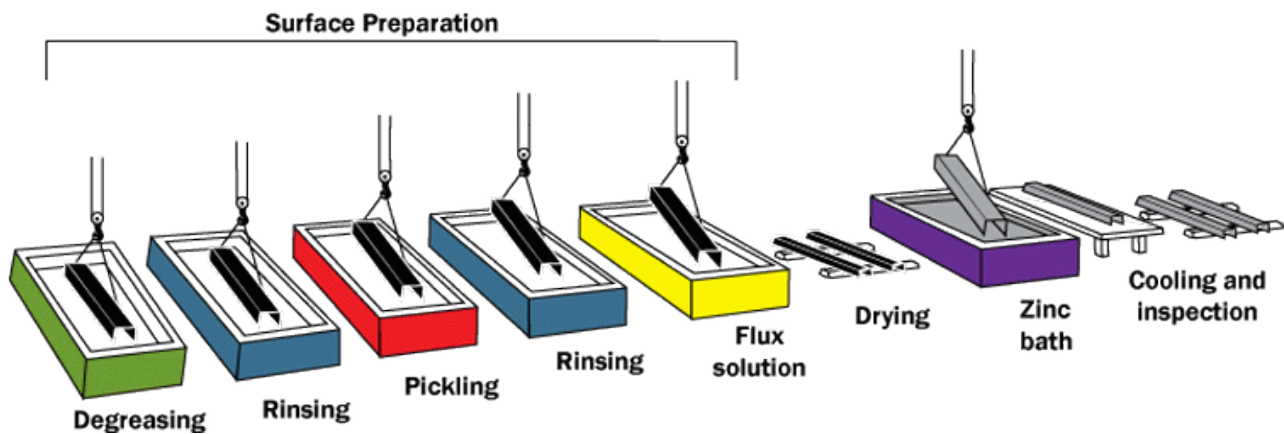


Figure 14. Graphical representation of hot dipping process [58].

2.3.7 Plasma Surface Cleaning Treatment

Materials that have low surface energy generally require surface treatment to promote the wetting of inks and coatings. One manner of increasing the surface energy and reactivity is to attack the metal surface with atmospheric plasma. When ionized gas is discharged onto the metal, crosslinking and activation are produced on its surface, as the result of ablation [59].

The surface treatment is the primary level of any coating technique for a material. This results in the proper functioning, protection, and performance of the coating systems. Surface treatment of the Aluminum 2024-T3 alloy serves three most essential functions.

- Provides corrosion protection to the bare metal.
- Forms robust physical or chemical bonds to the substrate, and stops delamination of the coating system.
- Provides adhesion to the epoxy primer or the top coat.

These functions indicate that without a surface treatment step, the top coat can become delaminated from the surface when exposed to an aggressive aqueous environment as compared to a top coat that has a pretreatment layer. Desirable adhesion of the primary layer to the metal substrate is instrumental in producing an excellent corrosion-resistant coating [60, 61].

A definite benefit of plasma surface treatment over different techniques is the uniformity of the surface modification and the corresponding uniformity of adhesion effects performed. The adhesion of surface treatment layer relies upon the traits of the metal surface, which consists of surface roughness, surface contaminants, nature of chemical bonds on the surface, and so forth. The plasma surface cleaning treatment is staged from the surface cleaning to the surface conversion into distinct oxides in order to enhance the adhesion of the surface treatment to the metal and eventually the adhesion of paints.

Plasma is a chemically active media; this gas appears as the fourth state of matter, representing the specific large type of components, as excited and ionized particles, each atomic and molecular, photons, and radicals. Most of these species carry a considerable amount of energy to induce chemical reactions, both in the plasma volume and at its interface with solid surfaces [62]. Figure 15 illustrates how the plasma surface treatment works and how the plasma

is generated [63]. In a plasma surface treatment, the plasma is formed from an excessive energy discharge among electrodes. Depending on the polarities concerned, the ions (+ polarity) that might be formed are accelerated in one direction, and the electrons (- polarity) are accelerated in the opposite direction. Preferably, the surfaces to be cleaned (or modified) are placed on a sample tray that is parallel to the electrode sets so that the plasma motion is calmly disbursed throughout the sample plane, and all samples receive the same degree of cleaning.

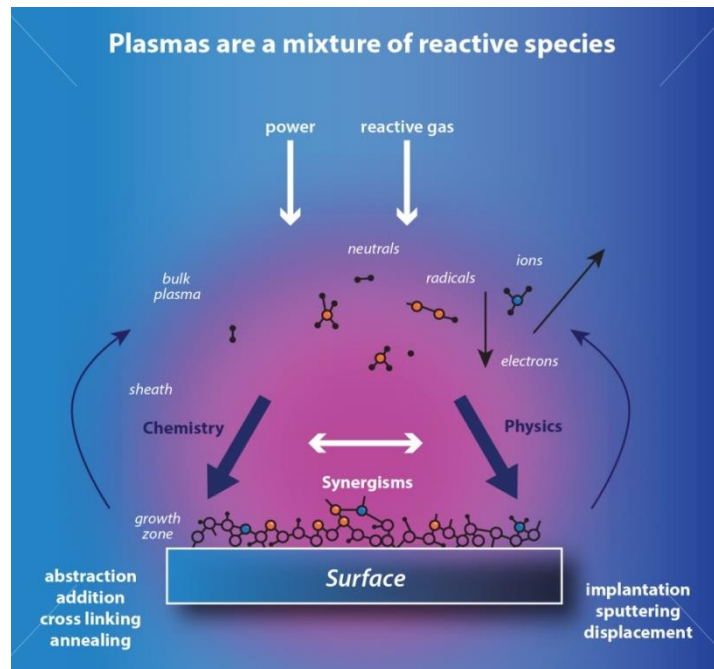


Figure 15. Illustration of how plasma surface treatment works and how plasma is generated [63].

2.3.7.1 Mechanism of Plasma Surface Cleaning Treatment

One mechanism by which a surface is modified is by way of the ablative impact of “molecular sandblasting.” In this mode, the excessive energy plasma particles “knock off” molecules from the sample surface. The surface region of any given planar dimension is consequently improved through the molecular peaks and valleys produced. Plasma gases that clean with the aid of ablation alone are inert gases consisting of argon and nitrogen. A secondary treatment takes place when a chemical reaction additionally occurs between the plasma gas and

the ongoing surface treatment. Gases that fall into this class are oxygen, sulfur hexafluoride, carbon tetrafluoride, and so forth. The precise gas(es) is decided on consistent with the nature of the surface treatment required or the quality of the contaminant to be eliminated [64]. Figure 16 shows the changes in surface wetting and apparent area of contact after plasma treatment [65].

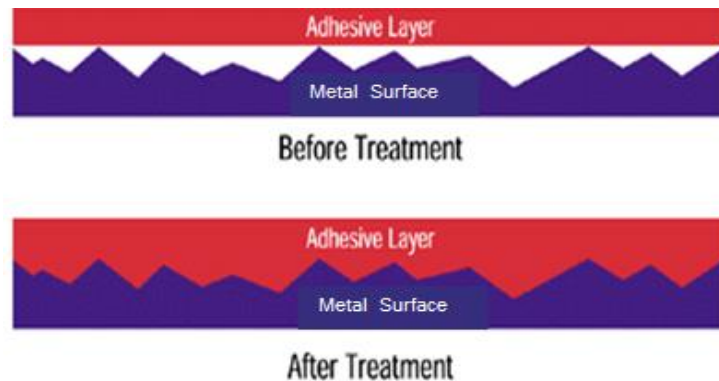


Figure 16. Changes in surface wetting and apparent area of contact after plasma treatment [65].

To eliminate organic contaminants, oxygen plasma accompanied by argon plasma is typically used in the plasma surface cleaning treatment. Here, the oxygen plasma will crack the organic hydrocarbon molecule, thereby producing water, carbon monoxide, and carbon dioxide. Any remaining oxide layer is then ablated from the surface throughout a next argon plasma cycle [66]. Figure 17 shows how the plasma surface cleaning treatment works.

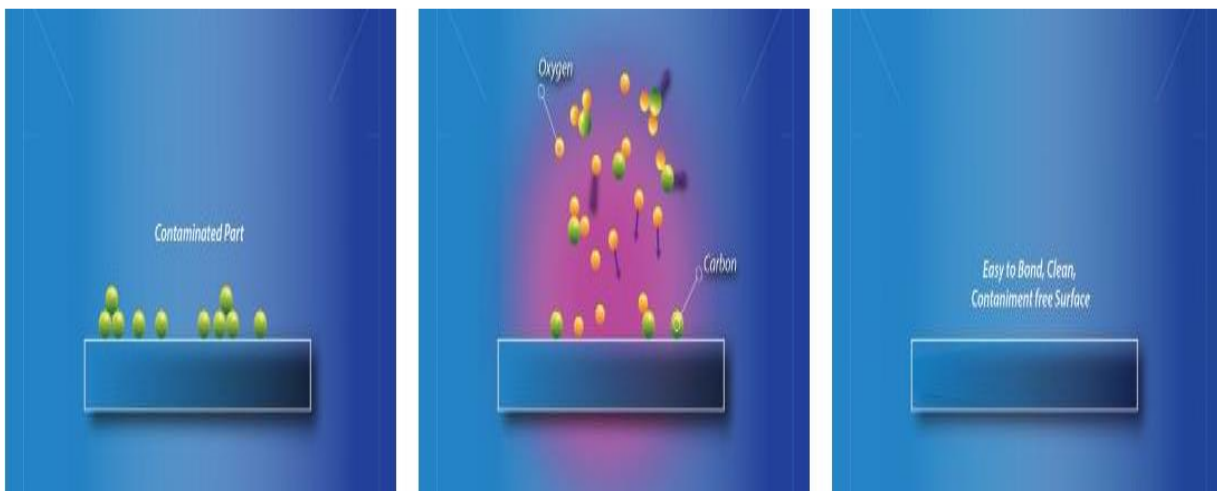


Figure 17. Illustration of how plasma surface cleaning treatment works [63].

2.3.7.2 Benefits of Plasma Surface Cleaning Treatment

Plasma is a particularly unusual and reactive chemical environment in which many plasma-surface reactions occur. The high-density of ionized and excited species inside the plasma can alternate the surface properties of ordinarily inert materials. Plasma surface treatment strategies combining the benefits of conventional plasma and ion beam technologies are potent techniques for medical implants with complicated shapes [67]. Mainly, modification of the surface energetics of the materials can enhance the adhesion strength, surface and coating properties, and biocompatibility, to name a few [68]. In short, plasma-based techniques provide the following benefits:

- Plasma processing rise from the best expertise of plasma physics and chemistry discovered in different fields, which includes microelectronics, as an example, plasma homogeneity, and the results of non-uniform plasma on the substrate surface [69].
- Plasma engineering is dependable, reproducible, non-line-of-sight, noticeably less expensive, and relevant to distinctive sample geometries in addition to distinct materials including metals, polymers, ceramics, and composites. Plasma techniques can be monitored quite appropriately using in-situ plasma diagnostic devices.
- Plasma treatment can bring about modifications of a spread of surface characteristics, for instance, chemical, tribological, electrical, optical, biological, and mechanical. Proper applications yield dense and pinhole-free coatings with excellent interfacial bonds because of the graded nature of the interface.
- Plasma processing can offer sterile surfaces and can be scaled as much as industrial production exceedingly without problems. On the other hand, the ability of non-plasma techniques for distinct substrate materials is smaller [70].

- Plasma techniques are well matched with protecting strategies to permit surface patterning [71], a method that is typically used within the microelectronics industry.

Plasma surface treatment is an economical and powerful materials processing technique in many fields. It is feasible to alternate in continuum the chemical composition and properties consisting of wettability, metal adhesion, dye capacity, refractive index, hardness, chemical inertness, and lubricity of materials surfaces. The application of plasma primarily based surface treatment techniques is quite diverse, and examples of applications encompass cleansing and sterilization, coating or depositing, and implantation of the modification of surface chemistry of a substrate.

2.4 Corrosion Rate Measurement

The importance of corrosion prevention the increasing awareness of the occurrence of alloy or metal corrosion. It is very important to determine the rate of corrosion. If the corrosion rate is decidedly small, then the failure initiated is of little practical significance. The corrosive rate can be measured by many techniques, such as weight loss of the material, depth of diffusion, and amount of pits per unit area. Though researchers extensively use these methods, they deliver time-average values over a very long period. However, electrochemical techniques can be used to determine corrosion rates quickly.

2.4.1 Linear Polarization Method

In a corroding material, the method of linear polarization takes place with the various current and the potential utilized over a small range of the open circuit potential. Open circuit potential is the potential of the working electrode relative to the reference electrode while no potential or current is being implemented in the cell. This direct current potential reaction is because of the exponential relation of the anodic and cathodic currents of a corroding material to

the potential and is derived from the Butler-Volmer equation [72]. Over a minimal potential variance that is much less than 20 mV, this variance between cathodic and anodic exponential curves is probably linear.

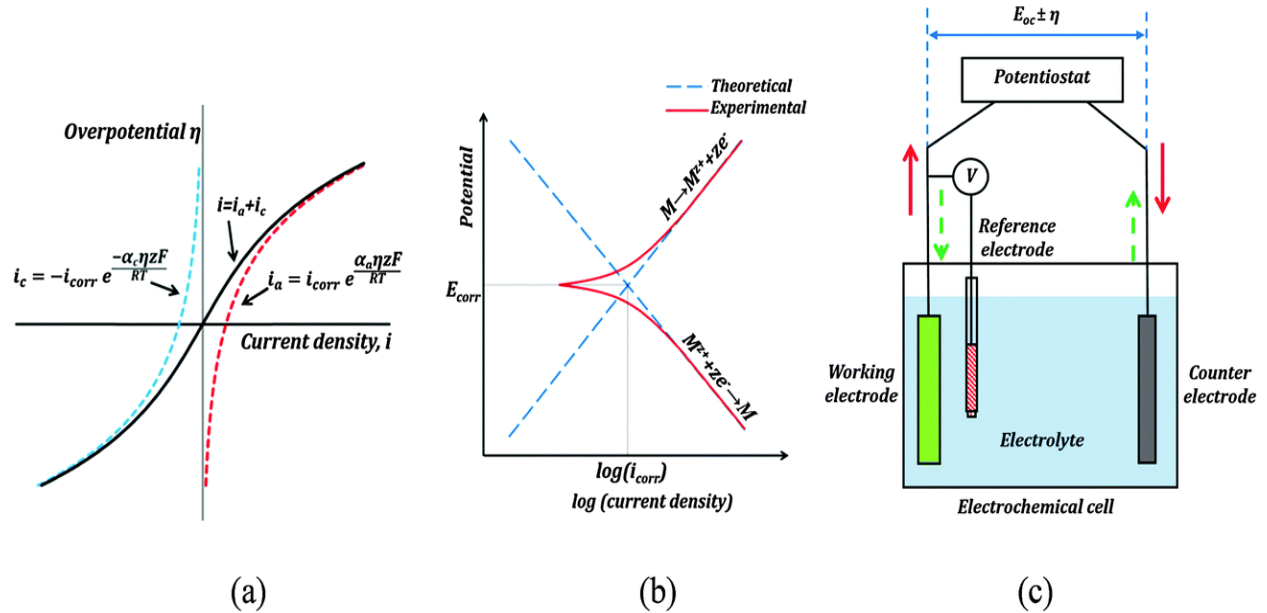


Figure 18. (a) Typical i vs. η dependency based on Butler-Volmer equation; (b) red curves showing Tafel plot of net (anodic and cathodic) current; and (c) typical three-electrode setup for linear polarization method for measuring corrosion rate [73].

When a metal is submerged in an aqueous solution comprised of ions of that metal, oxidation of the metal and a reduction of the metal ions will occur at the same time. These reactions stand for two variables, the rate of these two reactions can be regarded with the aid of the anodic current density (i_a) and the cathodic current density (i_c). Assuming that there are no similar electrode reactions taking place at the electrode surface, the two current densities could be equivalent and opposed at equilibrium, which is known as exchange current density (i_0), as shown in Figure 19 as a Tafel plot [74].

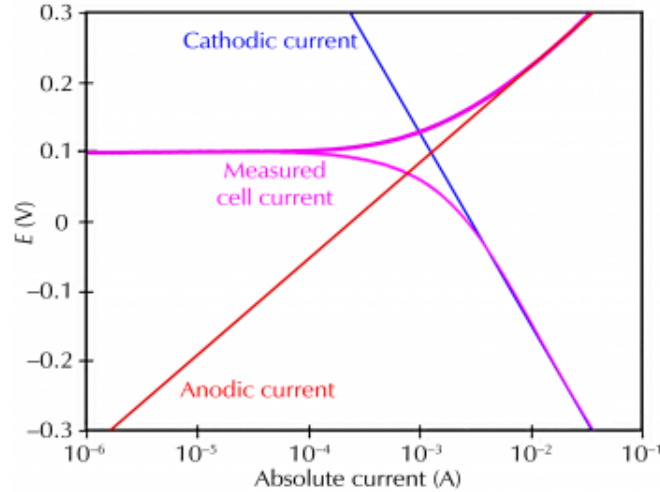


Figure 19. Classic Tafel plot [74].

Afterward, applying an external i_0 to the electrode surface, i_a will not be equal to i_c in amount, which also changes the electrode potential (E). The electrode is supposed to be polarized. The change of electrode potential is referred to as polarization, and the eccentricity from the reversible electrode potential is called the over potential, η :

$$\eta = E_i - E \quad (2.1)$$

In general, polarization can be classified as activation polarization or concentration polarization. Activation polarization is referred to as charge transfer polarization, which is initiated by the resistance produced when electrical charges transfer over a double layer. Concentration polarization is known for the concentration slope formed between the interface of the electrode and the bulk solution [75].

Activation and concentration polarizations are only considered in an electrochemical method. Activation polarization is primary within a small polarization current range. In contrast, concentration polarization is the first tool when the EC method is polarized distant from equilibrium. The chain between these two types of polarization can be demonstrated by the polarization curve (PC), as shown in Figure 20. When the polarization current is in the

experience of activation polarization, two areas can be denoted, the linear polarization area and the Tafel area. The linear polarization area is traced just about ± 10 mV from the equilibrium potential, and the Tafel area is at about ± 50 mV [76].

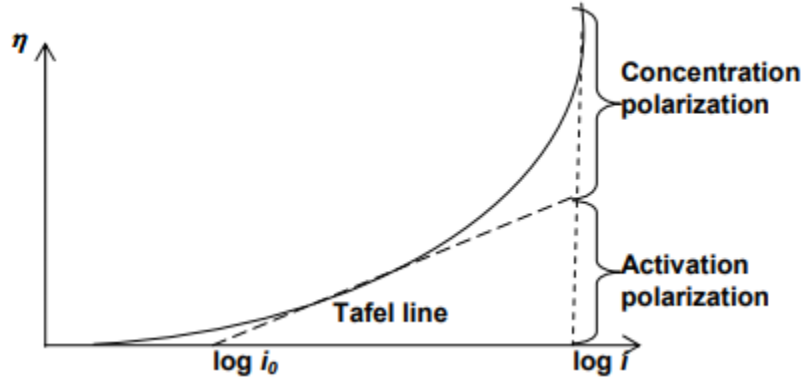


Figure 20. Polarization (η) as function of $\log i$ [77].

At polarization, which is indicated by values larger than 50 mV, there is a linear correlation between the over potential and the logarithm of the current density as accessible by the Tafel line. This correlation can be symbolized by the Tafel equation (2.2):

$$\eta = a + b \log i \quad (2.2)$$

where η is the overpotential, and a and b are constants, which can be expected hypothetically for many reaction mechanisms. Experimentally, the Tafel slope b can be acquired by calculating the gradient of the $(dE/d \log i)$ plot. In detail, for cathodic polarization, the Tafel slope is represented as b_c ; for anodic polarization, the slope is represented as b_a [78].

In linear polarization area, a metal is polarized with a low current in an electrolyte (i.e., for potentials that are about ± 10 mV from the corrosion potential (E_{corr})), an undeviating relation concerning the potential (E), and the current (I) applied to the electrode, which can be stated as

$$I_{corr} = \frac{b_a b_c}{2.3(b_a + b_c)} \left(\frac{dI}{dE} \right) E_{corr} \quad (2.3)$$

which is effective, while the relationship between current (I) and potential (E) follows the equation:

$$I = I_{corr} \left\{ \exp \frac{2.3(E-E_{corr})}{b_a} - \exp \frac{-2.3(E-E_{corr})}{b_c} \right\} \quad (2.4)$$

In equation (2.3), $\left(\frac{dI}{dE}\right)_{E_{corr}}$ is the gradient of the potential-current plot at the E_{corr} and is called the polarization resistance (R_p); b_a and b_c are the Tafel b slopes of the anodic and cathodic polarization curves, respectively; and I_{corr} is the corrosion current. Using K to substitute for $\frac{b_a b_c}{2.3(b_a + b_c)}$, the equation can be modified as

$$R_p = \frac{K}{I_{corr}} \quad (2.5)$$

If the value of K is recognized and R_p is obtained from experiment, then the I_{corr} can be derived from this equation. The values assigned to b_a and b_c are different for different materials, and nearly estimated values are frequently used in the calculation. Moreover, the gradient of the potential-current curve is every so often attained when E is not close to E_{corr} . The impreciseness of the Tafel slope value rises the use of the linear polarization method [79].

2.4.2 Electrochemical Impedance Spectroscopy

Electrochemical impedance spectroscopy (EIS), also recognized as alternate current (AC) impedance spectroscopy, is an EC method used to estimate the electrochemical properties of an electrode and electrode/electrolyte interface. This method has established its use in the field of electrochemistry in line with the dynamic facts that are extracted from the electrode surface and the interfacial properties with an electrically conducting electrode [80]. Corrosion is an area where EIS shows a significant role in investigating the kinetic properties and the mechanism. More than defining the surface electrical properties of an electrode, EIS is used for defining the interfacial properties where simple microscopic developments occur. Essential significant

electrochemical reactions at the electrode surface and electrode/electrolyte interface are the critical aspect in accepting the corrosion mechanism and its properties [81].

EIS is constructed from Ohm's law on electrical circuits, which explains resistance as the ratio of voltage over current:

$$R = \frac{E}{I} \quad (2.5)$$

where R is the resistance, I is the current over the resistor, and E is the voltage through the resistor.

The capacity of a conducting material to resist the flow of a current in an electrical circuit is called resistance, and this material is called a resistor. For ideal resistors, the resistance rate is independent of the frequency at all current and voltage values. Impedance (Z) is the collective term related to resistance and is used where the complex behavior of one or more electrical circuit fundamentals is present. In EIS, a small AC voltage (1–10 mV) is applied to the EC system more than the range of frequencies and the response to the input signal, i.e., current, is measured. The response current signal ensures a phase difference with the applied potential signal. The variation in output potential with phase difference after an AC current is applied to a system is termed overvoltage [82]. When a potential signal rouses an EC system, it affects the numerous necessary developments such as electron transfer inside the electrode and at the electrode/electrolyte interface and from a charged species. Each electrolyte interface will perform exclusively when an electrical signal pass in the system. By computing this exclusive temporary response, it is conceivable to extract several properties of that EC system with one single measurement [83].

The rate of transfer of excited particles inside an electrolyte, inside an electrode, and at the electrode/electrolyte interface is determined by the resistance of the electrolyte, electrode,

and rate of response at the interface. Surface structural imperfections, crystallographic orientation, and the presence of extraneous species can similarly impact the confined electrical field. EIS continuously applies an insignificant potential disruption with the purpose of maintaining pseudo linearity in the cell's response. For small electrical signals, the reaction is always pseudo-linear, with a small variation in phase between the applied and response signal [84].

As the input to the EC system, consider an AC sinusoidal potential signal, as displayed below:

$$E = E_0 \sin(\omega t) \quad (2.6)$$

where E is the potential at time t , E_0 is the amplitude of the signal, and ω and t are radial frequency and time, respectively. The response to this sinusoidal potential signal will be a sinusoidal current signal, which has the identical frequency with altered amplitude and a phase shift, and is given as

$$I = I_0 \sin(\omega t + \phi) \quad (2.7)$$

where I_0 is the amplitude, and I is the current response at time t with a phase change ϕ .

By making use of Ohm's law on electrical circuits to the above input and response signal, the impedance can be calculated as

$$Z = \frac{E}{I} \quad (2.8)$$

$$Z = \frac{E_0 \sin(\omega t)}{I_0 \sin(\omega t + \phi)} \quad (2.9)$$

$$Z = Z_0 \frac{\sin(\omega t)}{\sin(\omega t + \phi)} \quad (2.10)$$

where $Z_0 = \frac{E_0}{I_0}$ is the amplitude of the impedance.

By referring to Euler's rule of complex functions for equation 2.10, it is possible to definite impedance in the formulation of a complex function with both real and imaginary parts as

$$Z = Z_0(\cos \phi + j \sin \phi) \quad (2.11)$$

With the EC method, the complex function is stated in one or both of two graphical representations known as Bode and Nyquist plots. If the real portion of the impedance is plotted against the imaginary portion of the impedance on the x- and y-axis, respectively, then we get a Nyquist plot, as shown in Figure 21.

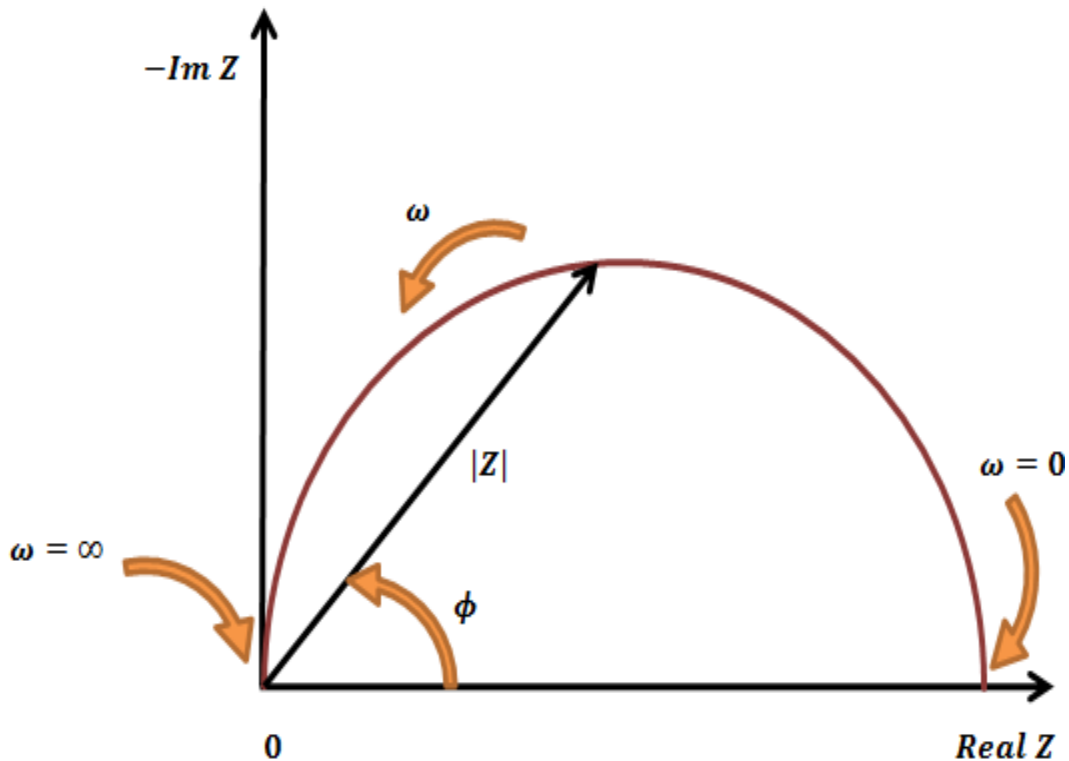


Figure 21. Nyquist plot with impedance vector.

From the Nyquist plot, it is possible to extract small EC factors consisting of solution resistance (R_S), polarization resistance (R_P), and overall resistance. Also, it is feasible to alter the number of time constants convoluted in the EC reaction by observing the shape of the Nyquist

plot. Each semicircle in the Nyquist plot is standard of a time constant associated with the EC process. Often only a portion of one or more of semicircles is seen. On the Nyquist plot, impedance is represented as a vector of length $|Z|$. The angle between this vector and the x-axis is ϕ , where ϕ is the phase [85]. The simple equivalent circuit with one time constant is shown in Figure 22.

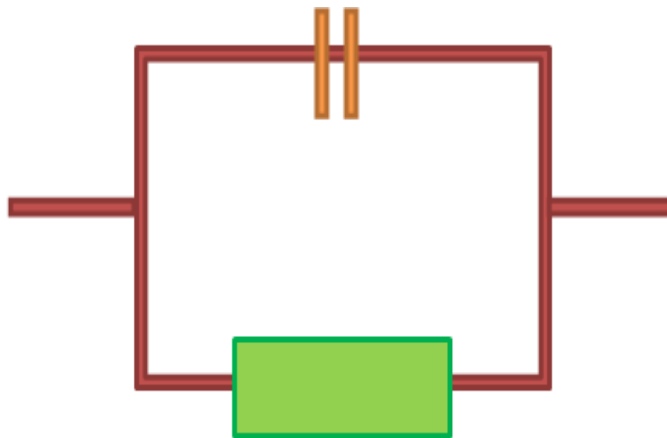


Figure 22. Simple equivalent circuit with one time constant.

A Nyquist plot does not display any frequency value; however, approximate frequency is used to develop the impedance at each data point. To overcome this inadequacy, a Bode plot was established to specify accurately what frequency was used to generate a data point. This Bode plot is designed with frequency on the x-axis and the absolute value of impedance and the phase angle on the y-axis. The Bode plot is likely to read impedance with detail to frequency and similarly the connection of capacitance and resistance in the EC reaction from the phase angle and frequency [86]. Figure 23 shows the Bode plot for the one time constant.

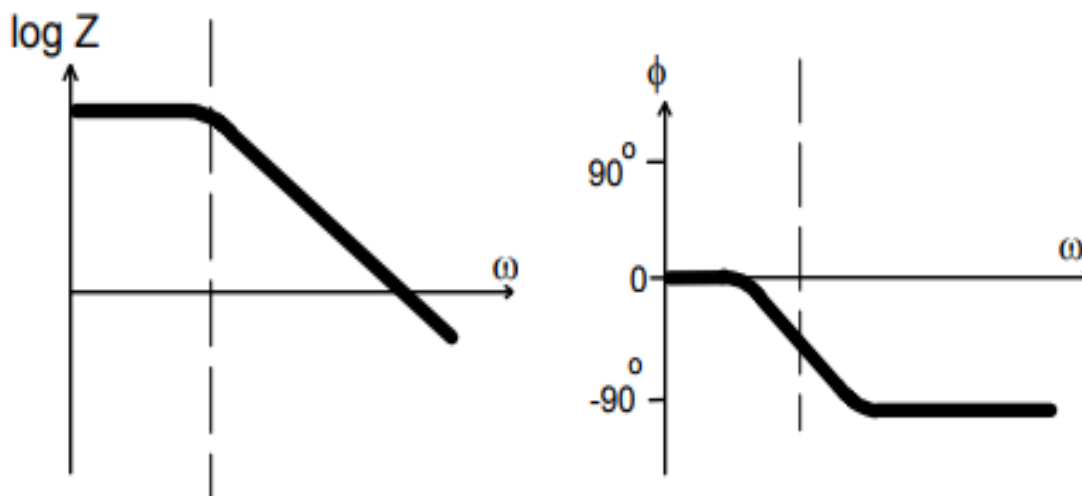


Figure 23. Bode plot with one time constant.

A study of Nyquist and Bode plots from the investigational data is prepared by fitting the experimental curves to a corresponding electrical circuit containing electrical circuit essentials such as resistors, capacitors, and inductors, which should ensure some physical relationship to the EC parameters of the response. For instance, a resistor can be used in places where there are conceivable conductive routes in the EC reaction. Therefore, EC constraints such as R_S (between the reference electrode and the working electrode) and R_p are symbolized by a corresponding resistor in the model circuit. Capacitors and inductors are used as a possible space charge polarization section in the EC process. The impedance of a capacitor has the inverse relationship with frequency, and the current over a capacitor leads the voltage through the capacitor by 90° [87].

These electric circuit elements are connected in a way that signifies the real EC process istaking place. Meanwhile, electrical circuit models can be completed in different formations with dissimilar fundamentals to provide the identical output; that is, there could be more than one conceivable circuit model for a particular EC reaction. Few expertize in the impedance of the

standard circuit components is consequently quite beneficial. Table 1 lists the standard circuit elements, the equation for their current vs. voltage relationship, and their impedance.

TABLE 1
COMMON ELECTRICAL ELEMENTS

Component	Current vs. Voltage	Impedance
Resistor	$E = IR$	$Z = R$
Inductor	$E = L di/dt$	$Z = j\omega L$
Capacitor	$E = C dE/dt$	$Z = 1/j\omega C$

It can be seen that the impedance of a resistor is impartial of frequency and has a real component which is most effective. Because there is no imaginary impedance, the current through a resistor is continuously in phase with the voltage. The impedance increases as frequency rises. Inductors have only an imaginary impedance component. As a result, an inductor's current is phase shifted 90° relative to voltage. Some information about the impedance of standard circuit components follows:

The most shared circuit model is the streamlined Randles cell containing a capacitor and resistors, as shown in Figure 24 [88]. The Randles cell proceeds into deliberation a modest EC reaction with solution resistance (R_S), which is often a significant factor in the impedance of an EC cell. A double-layer capacitance (C_{dl}) exists at the interface between the electrode and its surrounding electrolyte, and charge transfer resistance (R_{ct}) is formed by a single kinetically controlled EC reaction. The C_{dl} is swapped by a capacitor, and the solution resistance and charge transfer resistance are interchanged by resistors R_S and R_{ct} , respectively. In a three-electrode system, the double-layer capacitance lies parallel to the charge transfer resistance.

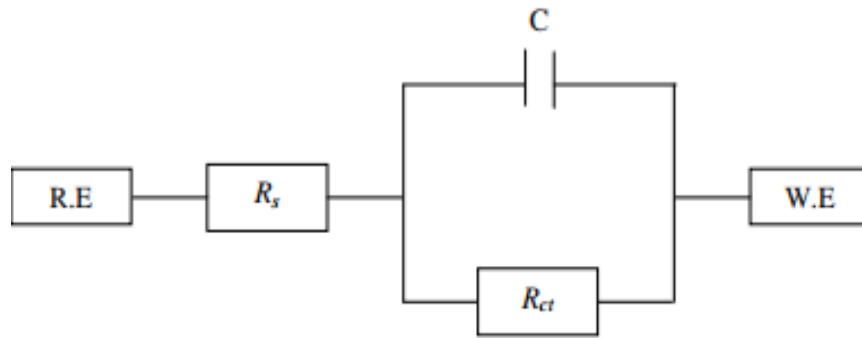


Figure 24. Equivalent circuit of simplified Randles cell [88].

It can be perceived that the Randles cell requires only one time constant. Therefore, a Nyquist plot for a streamlined Randles cell is a continuous semicircle, as shown in Figure 25.

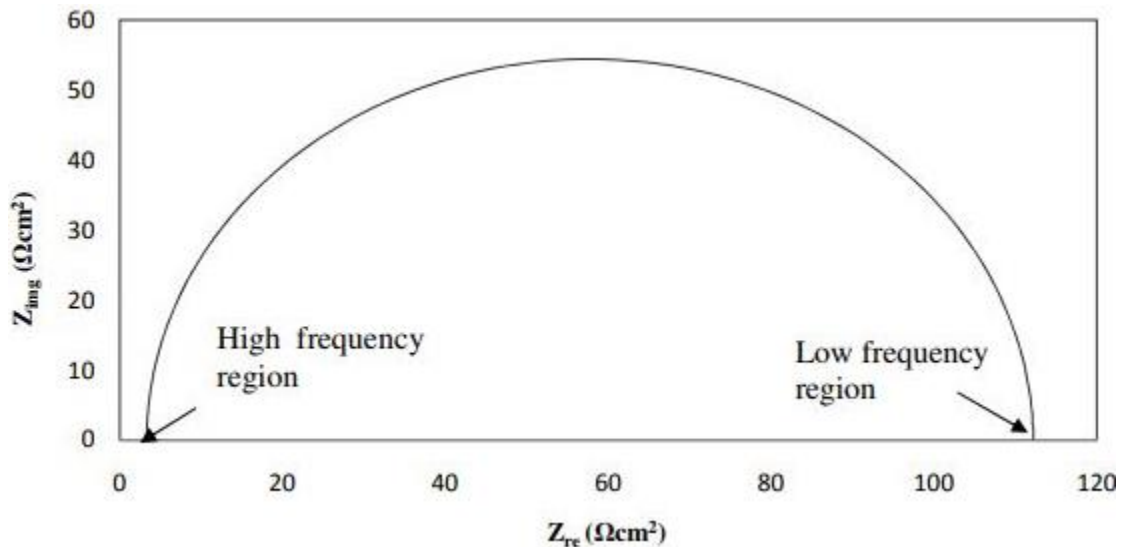


Figure 25. Nyquist plot for simplified Randles cell circuit [88].

The point where the impedance curve meets the real axis in the high-frequency region, i.e., near the origin, provides the solution resistance. The totality of R_{ct} and R_s is considered by making the point where the impedance curve meets the real axis in the low-frequency section. Consequently, the diameter of the impedance curve in a Nyquist plot gives the R_{ct} [89].

The Bode plot used for the Randles cell is shown in Figure 26 [88]. As can be seen, other factors such as frequency versus phase angle and impedance can be used to obtain a good result

on the resistor, capacitor, and inductor, and consequently design the corresponding electric circuit.

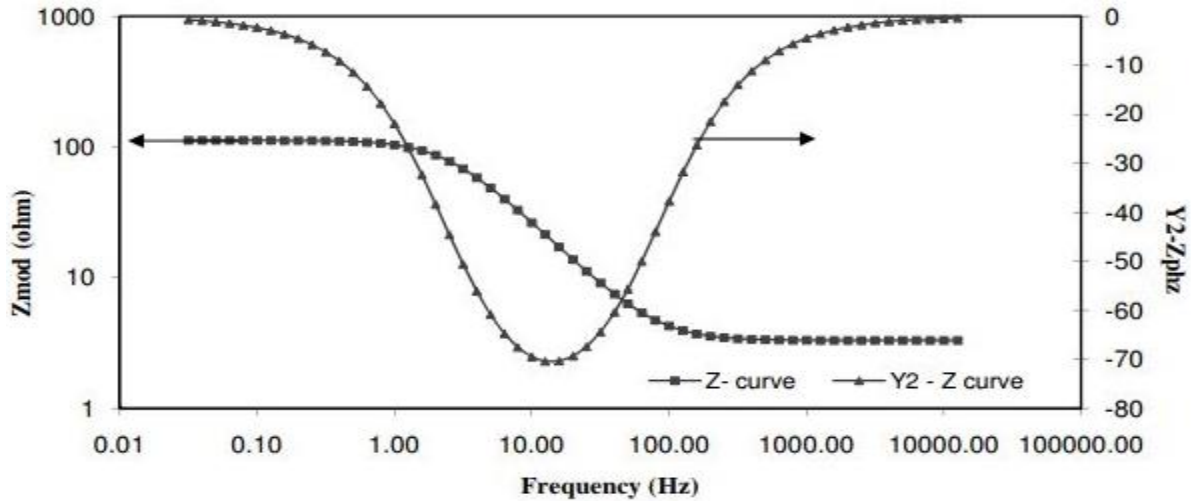


Figure 26. Bode plot for simplified Randles cell circuit [88].

2.5 Principle of Superhydrophobicity

2.5.1 Hydrophilic, Hydrophobic, and Superhydrophobic Surfaces

A surface can be categorized based entirely on the geometry of a water droplet on its surface. In this scenario, the angle where the edge of the water droplet meets the surface is measured, and the surface is categorized as hydrophilic, hydrophobic, or superhydrophobic. Hydrophilic coatings occur where the water droplet spreads along the surface and its contact with the surface increases, thereby covering the maximum surface. This is referred to as a water-loving surface, and in this situation, the contact angle is less than 90° [90].

A hydrophobic surface is referred to as a water-fearing surface. Here, the water droplet creates a spherical form on the surface, which decreases the contact of the water droplet with the surface. The hydrophobic coating has a contact angle higher than 90° and less than 150° [91].

A superhydrophobic surface is extremely fearful of water. Due to its nano-size roughness, this type of surface has a self-cleaning capability, and the contact angle is greater than 150° . The

purpose of this higher contact angle and nano-size roughness results in less contact between the water droplet and the surface. The sliding angle of this surface is less than 10°, which illustrates the self-cleaning capability of this surface. The adhesion between the water droplet and a dirt particle is higher than the adhesion between the water droplet and the surface; consequently, the water droplet eliminates all dirt particles when it rolls off the surface [92]. Fabricating this type of surface requires a polymeric material that has a low surface energy, and surface roughening material can assist in converting the surface geometry. Surface categories are precipitated by their contact angles, which are listed in Table 2; schematic views of these three types of surfaces are shown in Figure 27 [93].

TABLE 2
SURFACE CHARACTERIZATION OF HYDROPHILIC, HYDROPHOBIC, AND SUPERHYDROPHOBIC SURFACES

Surface Nature	Angle	Surface Energy	Effect
Hydrophilic	$\theta < 90$	Increases	Water droplet spreads
Hydrophobic	$\theta > 90$	Decreases	Water droplet beads up
Superhydrophobic	$\theta > 150$	Excellently decreases	Water droplet repels, and jumps off

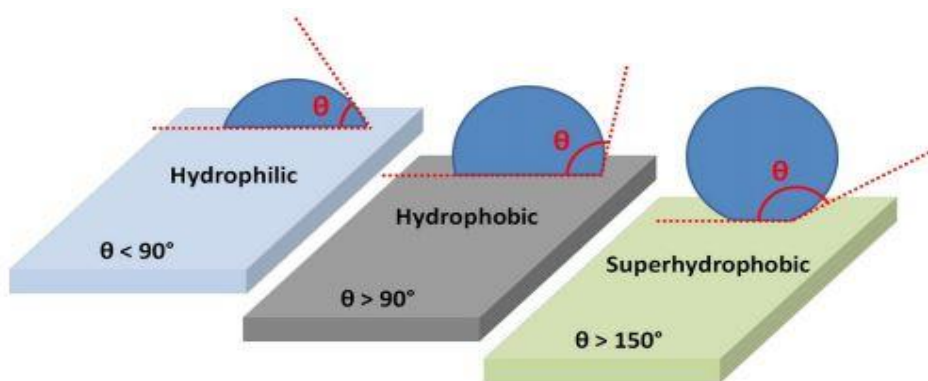


Figure 27. Schematic representation of water droplet on hydrophilic, hydrophobic, and superhydrophobic surfaces [93].

2.5.2 Contact Angle and Wettability of Superhydrophobic Surfaces

Contact angles are measured based on surface tension and wettability, as shown in Figure 28 [95].

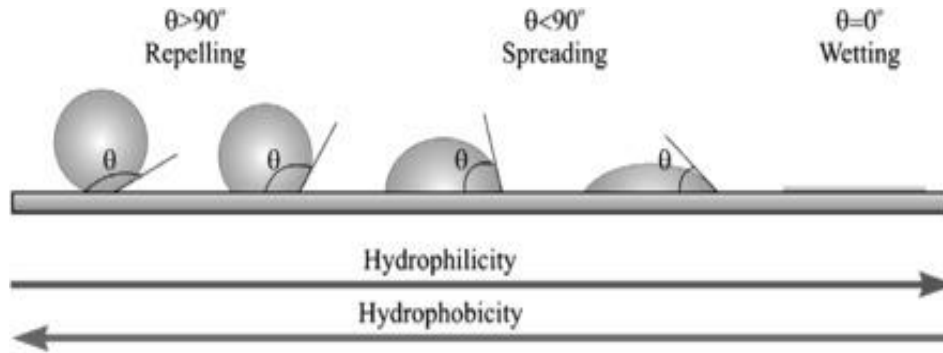


Figure 28. Schematic of contact angle and wettability of water drop placed on surfaces of different hydrophobicity [95].

Although it is difficult to measure the surface tension of a solid at once, it is easy to measure its contact angles. Consequently, the evaluation of surface tension through contact angle measurement has been studied by many researchers. The contact angles of polymers and organic layers can be used to predict the surface tension and wetting behavior of various liquids [94]. This can be described as follows:

The relationship between surface tension and contact angle is achieved by Young's equation [96]:

$$\frac{\gamma_{SG} - \gamma_{SL}}{\gamma_{LG}} = \cos \theta_c \quad (2.12)$$

where γ is the surface tension; and SG , SL , and LG are the solid-gas, solid-liquid, and liquid-gas interfaces, respectively, as shown in Figure 29 [97]. In line with Young's equation, the contact angle is a properly described property that relies upon on the surface tension coefficients of solid, liquid, and gas.

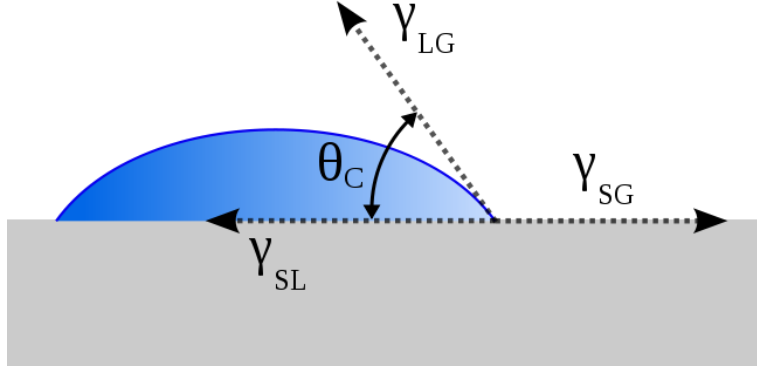


Figure 29. Drop on flat surface [97].

On the right side of equation (2.12), γ_{LG} can be determined by experimental measurement, thereby leaving two unknowns, γ_{SG} and γ_{SL} . When θ_c for a test liquid $> 20^\circ$, it is presumed that $\gamma_{SG} \approx \gamma_S$ and $\gamma_{LG} \approx \gamma_L$ [98]. Therefore, equation (2.12) can be reformulated as

$$\frac{\gamma_S - \gamma_{SL}}{\gamma_L} = \cos \theta_c \quad (2.13)$$

Similarly, the thermodynamic work of adhesion can be described by the Dupre equation:

$$W_{SL}^a = \gamma_S^a + \gamma_L^a - \gamma_{SL}^a \quad (2.14)$$

Since the thermodynamic work of adhesion is the negative of the free energy of adhesion, the free energy of adhesion is given by

$$\Delta G_{SL}^a = \gamma_{SL}^a - \gamma_S^a - \gamma_L^a \quad (2.15)$$

Combining equations (2.13) and (2.14) results in the Dupre-Young equation:

$$W_{SL}^a = \gamma_S^a + \gamma_L^a - \gamma_{SL}^a = \gamma_L^a(1 + \cos \theta) \quad (2.16)$$

From equation (2.16), Lifshitz-van der Waals (LW) interaction energy between a solid and a liquid is given as

$$W_{SL}^{LW} = (\gamma_S^{LW} - \gamma_{SL}^{LW}) + \gamma_L^{LW} = -\Delta G_{SL}^{LW} = \gamma_L^{LW}(1 + \cos \theta_e) \quad (2.17)$$

The term $(\gamma_S - \gamma_{SL})$ from equation (2.17) can be attained from contact angle measurements. Finally, γ_S can be estimated when γ_{SL} is known. The most frequently used method to assess γ_{SL} is the surface tension component approach.

According to Young's equation (2.12), this equation is appropriate for the simplest partial wetting of a solid having a smooth surface. However, real solids are not flawlessly flat. The surface structure impacts its wettability [99]. For instance, liquid droplets are in contact with the upper part of a rough surface, and the lower component is full of air when the surface of the solid is superhydrophobic [100]. Here, it is observed that the apparent contact angle of a drop deposited on a textured surface eventually represents a hydrophobic surface.

Bico et al. mentioned a probable function of roughness when a textured surface is in contact with a liquid. In line with Bico et al., the interfacial energy might be modified as much as dE according to the unit area when the adsorption increases through a small quantity dz , according to equation (2.18) [101]:

$$dE = (\gamma_{SL} - \gamma_S)(r - \Phi_S)dz + \gamma_L(1 - \Phi_S)dz \quad (2.18)$$

where r and Φ_S are the roughness of the textured solid and the area section of a solid surface, in direct contact with the liquid. The term $\Phi_S = 1$ is the situation of a completely wetted surface.

Figure 30 shows a micro-structured rough surface of a liquid reservoir [102]. The entire liquid quantity z decreases through adsorption while dE/dz is positive and increases when dE/dz is negative.

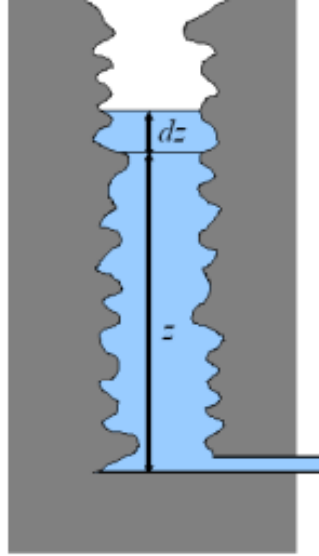


Figure 30. Rough surface of liquid reservoir [102].

Consequently, the liquid can be in equilibrium when

$$(\gamma_{SL} - \gamma_S)(r - \Phi_S) + \gamma_L(1 - \Phi_S) \approx 0 \quad (2.19)$$

Using Young's equation, equation (2.12) can be reformed as

$$\cos \theta_r = \frac{1 - \Phi_S}{r - \Phi_S} \quad (2.20)$$

equation (2.20) defines a critical contact angle between 0 and $\pi/2$, considering that $r \geq 1$ and $\Phi_S \leq 1$. For instance, the surface ought to be completely wet when r approaches 1 because the contact angle becomes 0. However, the contact angle will be near 90° when $r \gg 1$ or $r > 1$ and $\Phi_S \ll 1$.

2.5.3 Wenzel State and Cassie-Baxter Model

Roughness contributes sizeably to the wetting behavior of a surface. Considering that Young's equation is most suitable for a flat surface, different improved approaches are needed to describe the contact angle of a droplet on a rough surface [103]. When a surface is roughened, the minimization of liquid surface free energy results in two possible contact angles, the Wenzel

apparent contact angle or the Cassie-Baxter apparent contact angle [104]. Figure 31 indicates the apparent contact angle on a rough surface [102].

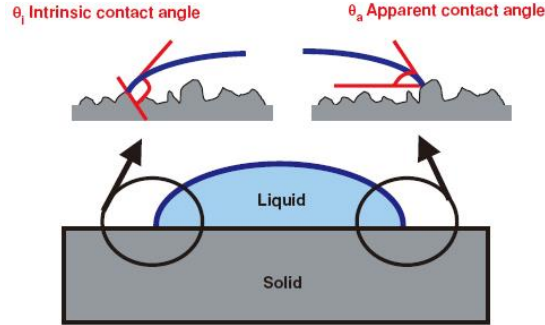


Figure 31. Drop on rough surface [102].

In Wenzel’s method, the liquid fills the indentations on the rough surface, as shown in Figure 32 [93].

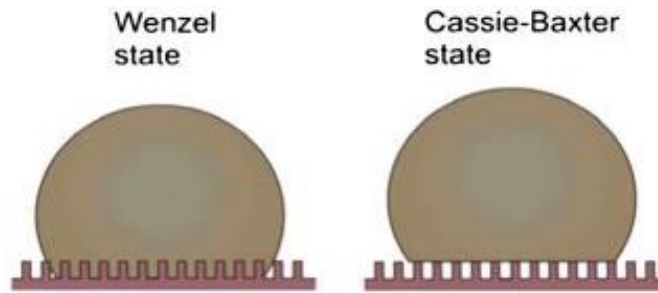


Figure 32. Schematic of water droplet in Wenzel state (left) and Cassie-Baxter state (right)[93]. According to Wenzel, the liquid contact angle at a rough surface can be described as [105]

$$\cos \theta_r^W = r \cos \theta_c \quad (2.21)$$

where r is the ratio of the entire wet region of a rough surface to the apparent surface region in contact with the water droplet ($r > 1$). If the Young’s contact angle is smaller than a critical contact angle θ_c , then the liquid is sucked into contact with the rough surface. By equation (2.21), for large r , the rough surface is dry when the contact angle on a flat surface exceeds 90° .

The Cassie and Baxter model is a modified form of the Wenzel model to define porous surfaces. Here, a liquid sits on a rough surface fabricated from a solid and air. Consequently, the

liquid does not fill the grooves of the rough solid, so the Cassie and Baxter model recommends the following:

$$\cos \theta_r^{CB} = f_1 \cos \theta_c - f_2 \quad (2.22)$$

where f_1 is the surface area of the liquid in contact with the solid divided through the projected region, and f_2 is the surface region of the liquid in contact with air trapped inside the pores of the rough surface divided through the projected region. Consistent with Cassie and Baxter,

$$f_1 = \frac{\text{Area in contact with liquid}}{\text{Projected area}} \quad (2.23)$$

$$f_2 = \frac{\text{Area in contact with air}}{\text{Projected area}} \quad (2.24)$$

When there is no trapped air, f_1 is identical to the value of r in the Wenzel model. Knowing this, equation (2.24) has recently been modified as follows:

$$f_1 = r_f f \quad (2.25)$$

$$f_2 = 1 - f \quad (2.26)$$

$$\cos \theta_r^{CB} = r_f f \cos \theta_c + f - 1 \quad (2.27)$$

where f is the fraction of the projected region of the solid surface in contact with the liquid, and r_f is described as analogous to the Wenzel model [106]. It is critical to note that r_f in equation (2.27) is not the roughness ratio of the entire surface, but rather that which is in contact with the liquid. In this form of the Cassie-Baxter equation, the contributions of surface roughness and trapped air are much clearer than in the other equations.

2.6 Icing Problems and Their Solutions

Icing occurs in nature through a super-cooled droplet from the environment, which is also known as “freezing rain.” Icing is characterized by the size of the droplets, water content, and temperature. Icing may cause harm to a system, loss of property, and damage to human lives.

Icing can severely affect many industries, including aviation, telecommunication, electrical equipment, and transportation. The aircraft industry is one of the leading industries that suffers most from icing. Factors comprising the size of the droplets, water content, and temperature can mainly affect aircraft as they make contact with super-cooled water droplets, both on the ground and in the air. Taking proper care of the icing problem is essential for the aviation industry, due to the fact that ice that inhibits distinctive parts of the aircraft, including propellers, wings, antennas, and so forth. Even while flying in harsh situations, pilot decisions perform an essential role in avoiding dangerous accidents. The risks of icing rely upon both the quantity of ice and kind of aircraft. While ice contamination is detected on the wings of an aircraft, the aircraft can stall at a decreasing temperature and also at higher speed. Likewise, the accumulation of ice will increase the load of an aircraft, decrease its thrust and lift, and possibly increase its drag.

Consequently, icing is one of the predominant problems in the aviation industry, and many types of research to find a feasible solution for elimination of its accumulation or delaying its formation time are being performed. To combat the icing problem while the aircraft is on the ground, the aviation industry has used a mechanical approach, including cleaning off the ice or snow using a broom, employing deicing fluid, and putting the aircraft in a heated hanger until the ice or snow melts. While in the air, some aircraft have a “deicing boot” or a “weeping wing,” which releases anti-icing fluid. Although these systems are available, they are costly and need frequent reapplication because they are chemical and mechanical strategies. An opportunity for modern deicing techniques could be to create a permanent surface that would eliminate or lessen the formation of ice. Superhydrophobic surfaces are a promising technique to contemporary deicing issues.

2.6.1 Atmospheric Icing

Atmospheric icing is a phenomenon that usually takes place while super-cooled water droplets within the surroundings are available to contact the outer surface of a structure and freeze. Ice formation on an aircraft is risky because ice impacts its aerodynamic system. Hydrogen bonding is an extensive function in icing. Icing is divided explicitly into classes based primarily on factors consisting of water, the diameter of water, the velocity of the wind, temperature, and surface in which the ice is taking place. Precipitation icing occurs when rain or snow comes in contact with a surface, and in-cloud icing is the result of cloud or water vapor deposition [107].

2.6.2 In-Cloud Icing

In-cloud icing takes place within a cloud that includes super-cooled droplets, i.e., droplets that stay liquid below 0°C. Here, water droplets within the air freeze on the surface of a structure that is within the clouds. Rime ice, which is the most common kind of in-cloud icing forms an ice vane at the windward side of a structure. Numerous factors affect the intensity and period of in-cloud icing: wind velocity, liquid water content within the cloud, air temperature, drop size distribution, height above cloud base, and dimensions of the exposed object. Hard rime, soft rime, and glaze are variations of in-cloud icing. In-cloud icing forms on aircraft or equipment at high altitude [108]. Dry icing occurs when the water droplet flux is less than that of the freezing rate, that is, when a water droplet freezes before other droplets fall inside the same region. Consequently, when the flux of a water droplet increases, the droplet does not freeze, even if another droplet impinges upon it. This causes wet ice formation. Dry ice forms rimes containing air bubbles, at the same time that wet ice creates a transparent glaze.

2.6.3 Precipitation Icing

Precipitation icing takes place as freezing rain/drizzle or wet snow accumulation. Glaze ice is the most common form of precipitation icing. Critical parameters used to explain precipitation icing are wind velocity and direction, the rate of precipitation, the liquid water content material of snowflakes, air temperature, relative humidity, and visibility. Precipitation icing takes place if water droplets are large enough to fall from the environment at an accelerating rate. This sort of icing can arise anywhere, irrespective of altitude [109].

CHAPTER 3

EXPERIMENTAL MATERIALS AND METHODS

3.1 Experimental Materials

The selection of materials encompassing this research process was comprised of evaluations of materials based on the conformity of their attributes to the possible characteristic improvability that was to be achieved with experimental iterations. A list of the metals was determined from the periodic table, and their physical and chemical properties were gauged and contrasted. Based upon the perceived superiority of the Aluminum 2024-T3 alloy relative to overall durability and, more importantly, its durability in environments that are conducive to corrosion, this material was chosen for the experimental aspect of this research.

3.1.1 Aluminum 2024-T3 Alloy

The classification of various aluminum alloys is to a large extent based on the quantity of their constituent metals. The three primary constituent elements of Aluminum 2024-T3 alloys are copper, magnesium, and iron. Furthermore, the composition percentage of these elements is the greatest in Aluminum 2024-T3 alloy compared to other AAs. Figure 33 shows a pictorial representation of Aluminum 2024-T3 alloy samples. The percentage of element components in Aluminum 2024-T3 alloy sample are listed in Table 3 [110].

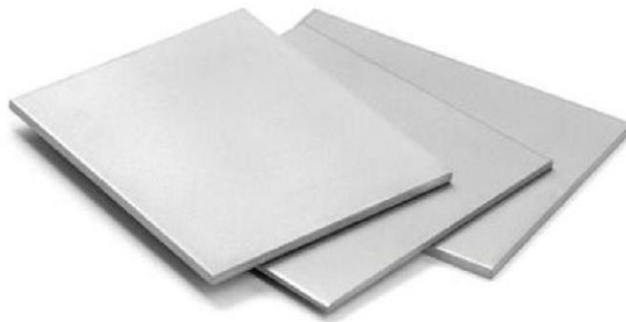


Figure 33. Aluminum 2024-T3 alloy samples.

TABLE 3

ALUMINUM 2024-T3 ALLOY COMPONENT PERCENTAGES

Aluminum 2024-T3 Alloy									
Element	Cu	Cr	Fe	Mg	Mn	Si	Ti	Zn	Others
Percent	3.8-4.9	0.1	0.5	1.2-1.8	0.3-0.9	0.5	0.15	0.25	0.15

3.1.2 Ultrasonic Cleaner

The ultrasonic cleaner is a microprocessor-controlled device that uses ultrasonic or high-frequency sound to clean electronics, medicine, gel materials, machinery, and a hard alloy such as aluminum. Ultrasonic cleaning is based on the cavitation effect caused by high infrasonic wave vibration signals in the fluid. Microscopic bubbles expand and rapidly shrink in the solvent, which in this study is deionized (DI) water and acetone. The impact of an ultrasonic cleaner will peel off stains from a specimen that is immersed in the solvent. The ultrasonic cleaner machine used in this research is located in the Room 125 of Wallace Hall at Wichita State University (WSU) and is shown in Figure 34.



Figure 34. Ultrasonic cleaner.

3.1.3 Mini Sprayer

The mini sprayer utilized in this research is the Ultra-Tech 4122 Mini Sprayer Kit, as shown in Figure 35. This kind of sprayer characteristically is a professional grade spray method that is excessive for many applications. It is disposable, recyclable, easy to clean, and, most advantageously, does not require a compressor. The Ultra-Tech Mini Sprayer uses a venturi vacuum process that pulls coating paint from a refillable compartment and distributes a professional-grade spray stream on any surface. It has a simple replacement and cleanup with interchangeable and disposable parts, is user compatible, has a refillable and reusable container, and offers a professional grade spray stream. The sprayer must be held no less than eight inches from and also perpendicular to the surface that is to be painted. For convenience, the Ultra-Tech Mini Sprayer is sold in a two-pack; therefore, in this research, one was used for the bottom coat and the other for the top coat. This sprayer can be cleaned by spraying a small amount of xylene onto a rag or waste container and allowing the sprayer to dry before reusing the sprayer.



Figure 35. Mini sprayer.

3.1.4 Superhydrophobic Coatings

The coating of the samples was a crucial step during the experimental trials. The coating used for this process consisted of a top coat and a bottom coat. To mitigate any chemical effects or microscopic physical alterations to the aluminum surface during the experiment, reactive inertness was highly listed; therefore, both the bottom and top coats show chemical homogeneity and proximity to each other. Thus, the Ultra-Ever Dry SE brand was used for both coats. The bottom coat consists of xylene, t-butyl acetate, and acetone, whereas the top coat consists of acetone and silica. The inequality in the chemical composition is necessary for the several coats necessary to establish a complementary relationship among their functionalities. The exactly aligned rate of the coat relative to the sample surface and continuous spraying of the coats were assured by thorough cleaning of the mini-sprayer with ethanol and soap. Ultra-Ever Dry SE bottom and top coats are illustrated in Figure 36.



Figure 36. Ultra-Ever Dry SE bottom coat (left) and top coat (right).

3.1.4.1 Bottom Coat

The Ultra-Ever Dry SE Bottom Coat is the first half of the Ultra-Ever Dry coating process, and in conjunction with the top coat prevents moisture-induced corrosion and the formation of ice crystals on the target surface, while maintaining dryness, preventing impurities, and repelling oil and water spills. The bottom coat differs from the top coat because of the presence of xylene among its ingredients. Xylene functions as a solvent to aid the active ingredients in the formation of a thin uniform coat. The bottom coat adheres well to steel, aluminum, plastic, leather, and wood surfaces. It is recommended to shake the can containing the bottom coat for a minimum duration of 5 to 10 minutes. The optimal spraying pattern for the coat to achieve favorable results is a horizontal left-to-right pattern followed by a top-to-bottom pattern on the same surface. A drying period of approximately 30 minutes to 1 hour for the bottom coat is strongly prescribed before applying the top coat.

3.1.4.2 Top Coat

The Ultra-Ever Dry SE Top Coat is the second half of the Ultra-Ever Dry coating process and is sprayed on top of the bottom coat to complete the Ultra-Ever Dry layer for prevention of rust, and aversion of impurities and wetting. The presence of interstitial spaces in the top coat contributes to air molecules being trapped, thus forming a molecular barrier to stop oil and water molecules from filling the coated surface and thereby guaranteeing it remains corrosion-free. The top coat differs from the bottom coat due to the presence of a few nanoparticles among its ingredients. However, nanoparticles with acetone mirror xylene in its function as a solvent to facilitate the active ingredients in the formation of a thin uniform coat. Identical to the bottom coat, the top coat clings well to steel, aluminum, plastic, leather, and wood surfaces. It is recommended to shake the can containing the top coat for a minimum duration of 3 to 5 minutes.

The optimal spraying pattern for the coat to achieve favorable results are thin layers sprayed in a horizontal left-to-right pattern followed by a top-to-bottom pattern on the same surface. Before applying the top coat, a period of one hour should elapse to ensure dryness of the bottom coat. Testing of the sample should commence after a period of 15 to 30 minutes after spraying on the top coat to ensure its dryness. Furthermore, average utilization of the sample requires a drying time of two hours.

3.1.5 Plasma Cleaner Used for Preparing Sample Surface

The main apparatus used to prepare the surfaces of the samples in this research was a plasma cleaner. The precise cleanliness of the sample surface can only be realized by using this piece of equipment. This rectangular device has a centerpiece including a vacuum chamber in which the sample is placed. An important component of this process is gas, typically oxygen, although other types may be used, at an initial low pressure. The plasma is the heat source that eliminates impurities from the surface of the sample. Once the device is initialized, a continuously varying electromagnetic field is induced via radio frequency (RF), which stimulates only a partial number of oxygen molecules. The highly energetic molecules collide with the molecules possessing low kinetic energy and convey an effective momentum to dislocate electrons from their atoms, thus producing an ionizing effect that ionizes the gas and produces plasma. Once the surface of the sample is exposed to the plasma, the process of debris eradication becomes sensitive to the interplay of many variable parameters, namely, the intensity of the plasma, which in turn varies with the level of gas ionization; the type of sample material that is subject to change, which can alter the required plasma intensity for surface purification; and the exposure time of the sample to the plasma radiation. Oxygen was the gas used in the plasma cleaner for this research. This equipment, which operates very easily, includes a compact,

economical, active fan for cooling, and a better-quality metering regulator for minimal range surface cleaning and initiation of small samples. The plasma cleaner used in this research is illustrated in Figure 37.



Figure 37. Plasma cleaner.

3.1.6 Industrial Oven Used for Heat Treatment

The heat treatment of the plasma-treated SH-coated AA 2024-T3 sample is a different challenge. The procedure requires the samples to be heated at a very high-temperature range while preventing the potential temperature variations initiated by the originating heat to alter the room temperature. The machine that was found to be an appropriate solution to this problem was the industrial oven. The industrial oven selected for the heat treatment process had the following attributes: a high triple-digit heating range, accurate measurement calibration accredited to a digital display, and interior panels lined throughout with insulation to ensure room temperature constancy about the time elapsed. The industrial oven used during the heat treatment process is located in Room 125 of Wallace Hall at WSU and is shown in Figure 38.



Figure 38. Industrial oven.

3.1.7 Optical Contact Angle Goniometer

An essential physical parameter of this research is the measurement of the contact angle. Contact angles of the water droplets with detail relative to the incident surface of the plasma-treated SH-coated AA 2024-T3 samples were measured using an optical contact angle goniometer (model CAM 100 series from KSV Instruments Limited and located in Room 139 of the WSU bay area). This contact angle measurement system consists of a high-resolution camera, which vividly captures the moment of droplet incidence, and an advanced software package coupled with the camera to evaluate the generated images, translate the pictorial data by computing the critical contact points, and consequently calculate the contact angle. It is worth mentioning here that the importance of this software is enormous since all critical variables are quantified and calculated solely by automated algorithms. User interference and neglect are at a minimum. The optical contact angle goniometer used in this research is shown in Figure 39.

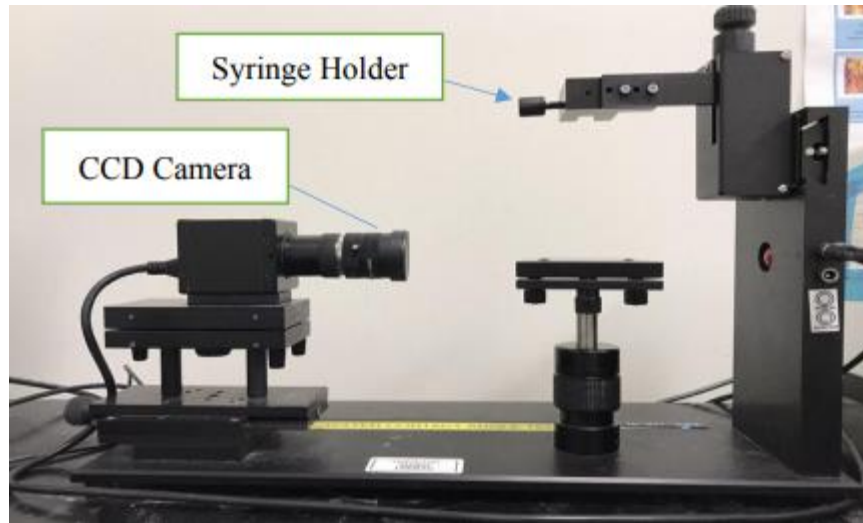


Figure 39. Optical contact angle goniometer.

3.1.8 3M Adhesion Tape

3M adhesion tape was used mainly to help protect surrounding surfaces from overspray, to provide clean paint lines, and to be removed quickly and cleanly when finished. 3M adhesion tape adheres well, resists solvents or water from the paint, and is strong enough to hang plastic sheeting, yet be removed neatly without damaging the subsurface. In this study, this adhesive tape was used to perform the tape adhesive test, which was executed on the plasma-treated SH-coated AA 2024-T3 sample in order to define the adhesion property of coating layers on the surface. This straightforward process is used to test the adhesion of a thin layer of coating attached to a substrate.

3.1.9 Sodium Chloride Solution

In this research, corrosion in metals and alloys is a primary factor. Corrosion occurs on metals and alloys because of the uncertain surrounding environment such as sea water or a chemical environment, where seawater is very severe solution to corrosion. In this study, instead of sea water, a 3% or 0.5M NaCl solution was used. The preparation of this NaCl solution is a simple process; however, great caution must be practiced from the beginning to the end of the

process, since it is salt that can accentuate unwanted chemical reactions with the plasma-treated SH-coated AA 2024-T3 samples. First, uniformly unbroken NaCl crystals weighing in at 29.22 g were carefully selected. Second, these NaCl crystals were diluted into precisely-measured 1000 ml of DI water, thus producing a 3% or 0.5M NaCl solution.

3.1.10 Deionized Water

The solvent chosen for producing the NaCl solution was DI water, as mentioned previously. The reason for its selection was to prevent any assisting active chemical reactions from taking place, the derivatives of which can obstruct the precise measurement and analysis of relevant parameters such as the contact angle. Deionized water attains these inert characteristics due to the vigorous filtering process it undergoes (filtered to 0.05 microns), which removes any metallic and inorganic ions, the primary markers of reactionary interference. This type of water was also utilized to implement the electrochemical analysis in the later phases of the research. Plasma-treated SH-coated AA 2024-T3 alloy samples were immersed in the DI water for 30 days to verify how water that has no ions or that cannot assist with any chemical reactions help prevent corrosion.

3.1.11 Gamry Reference 600 Potentiostat

A Gamry Reference 600 Potentiostat was used to actualize the polarization curve at a scan rate of 50 mV/s for the plasma-treated SH-coated AA 2024-T3 sample. This hardware was also used to determine the impedance spectra of the plasma-treated SH-coated AA 2024-T3 sample gathered at the open-circuit potential of the working electrode and counter electrode. The experimental setup for the electrochemical corrosion test is shown in Figure 40.

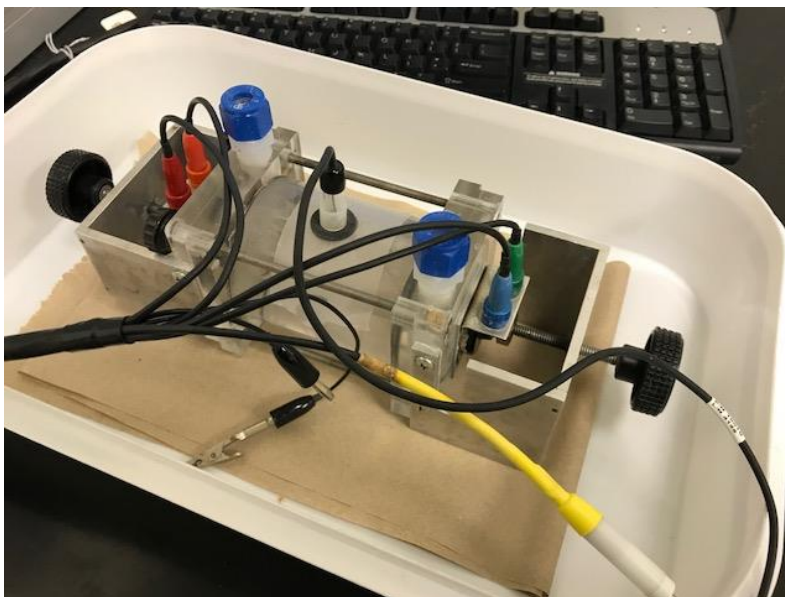


Figure 40. Experimental setup for electrochemical corrosion test.

Corrosion rates were also estimated for the plasma-treated SH-coated AA 2024-T3 samples by using the Gamry Reference 600 Potentiostat and Gamry Corrosion Cell. The aluminum samples were manufactured in small pieces (1" x 2") so they could fit in the Gamry cell. Aluminum samples surfaces were correctly cleaned, as mentioned above, and pertinent steps were taken to ensure that the bare AA 2024-T3 surface was plasma-treated and superhydrophobic coated. A three-electrode system in a conventional glass-made corrosion cell was used for the EC measurements: a plasma-treated SH-coated AA 2024-T3 sample, 3 mm in diameter, as a working anode electrode, graphite as a counter cathode electrode, and a saturated calomel reference electrode. All the potential values testified are given concerning this reference electrode. Testing solutions, i.e., the NaCl solution, was distributed into the Gamry corrosion cells up to the black marked level. All sensor connections were given between the Gamry Corrosion Cell and Gamry Reference 600 Potentiostat as per the machine setup by following the sensor color code, as shown in Figure 41.

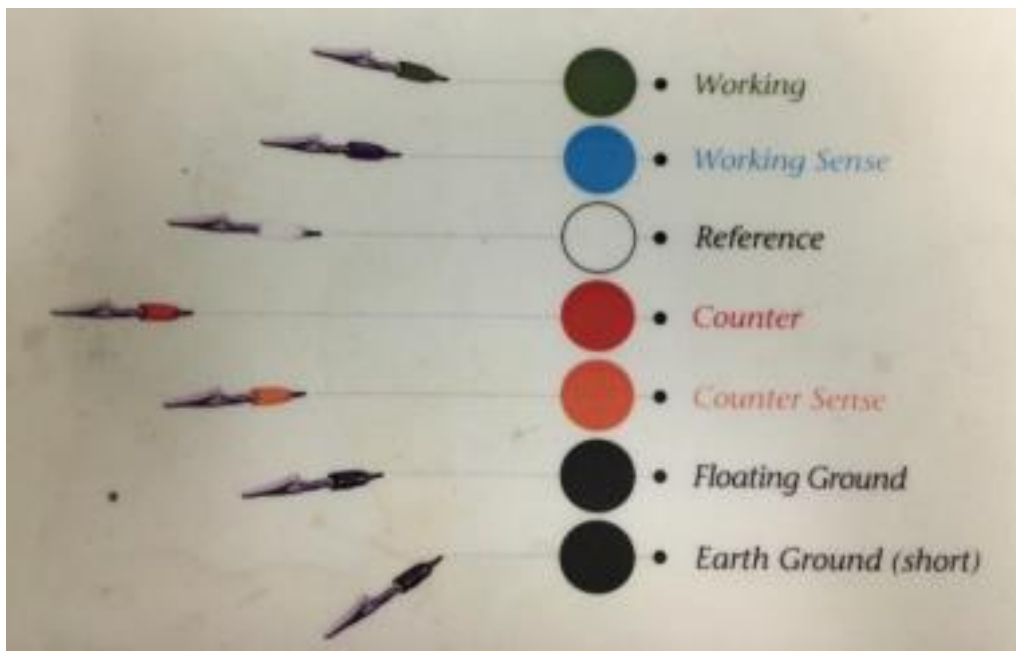


Figure 41. Color code for sensors connections with Gamry cell.

Electrochemical impedance spectroscopy results were analyzed by fitting the experimental impedance information to electrical equivalent circuit models. Parameters of the electrical equivalent circuits were obtained by fitting the impedance function to the deliberate Bode and Nyquist plots. Furthermore, the results of EIS can be investigated to regulate the rate-controlling steps. An EIS measurement was directed during a three-day period by the corrosion-measurement system using this equipment. With this device, the amplitude of the sinusoidal signal was 10 mV, and the frequency span was 1 MHz to 1 Hz. The EIS tests were always conducted from high frequency to low frequency, and Gamry Framework software was used for data fitting of the impedance spectra.

3.1.12 Fourier Transform Infrared Spectrometry

After the EIS test, plasma-treated SH-coated AA 2024-T3 samples, which were immersed in 3% 0.5M NaCl solution for 30 days and SH-coated AA 2024-T3 samples were at a diagnostic point for reaffirming the adhesive durability of the coating with respect to its

adherence to the substrate. The only comprehensive and reliable method for evaluating the adhesive durability was by utilizing Fourier transform infrared (FTIR) spectrometry. The FTIR spectrometer emits infrared radiation that when it strikes the surface of the sample reflects the atomic chemistry profile relating to the sample's chemical composition. The intramolecular atomic bonds between the functional groups on either end of the adhesive, coating, and substrate are identified, as well as the intermolecular bonds between the functional groups of the coat and the adhesive. The forces keeping the bonds intact are instrumental in relaying information about the adhesive strength.

In this analysis, the plasma-treated SH-coated AA 2024-T3 sample was kept in contact with the ATS crystal of the FTIR machine. The ATS crystal moves along the internal surface of the aluminum sample in a way that it is redirected from the infrared beam. FTIR images were taken of plasma-treated SH-coated AA 2024-T3 samples at 0 days and also samples that were immersed in a 3% 0.5M NaCl solution for 30 days. The plasma-treated SH-coated AA 2024-T3 samples were kept on the equipment surface to standardize the amount of light immersed by the compounds at changing wavelengths and to classify the different types of bonds that exist in the compound at specific wavelengths of light.

The EZ-OMNIC software used in FTIR analysis helps in interpreting the infrared patterns generated for each identified bond by producing a mathematical model, assigning magnitude values to vital bond forces such as Van der Waals forces, and computing the wavelength-to-transmittance ratio. FTIR spectra were engaged for a few samples in a range of more than 400 to 4,000 cm^{-1} . The model designation of the FTIR spectrometer used was a Nicolet Magna 850R from the WSU chemistry department, as depicted in Figure 42.



Figure 42. FTIR spectrometer.

3.1.13 Vickers Hardness Test

After the FTIR test, of the Vickers hardness number (HV) was computed for the bare AA 2024-T3 samples and plasma-treated SH-coated AA 2024-T3 samples. The American Standard for Testing Materials (ASTM) E92 is the standard used for this method. This test checks the mechanical properties of the plasma-treated SH-coated AA 2024-T3 samples, indicating and how the plasma surface cleaning technique affects the mechanical properties of the samples. The advantage of the process is that it can be used for thin and superficially hardened materials for which other methods are not suitable. A diamond in the form of a square-based pyramid forms the Vickers indenter, as shown in Figure 43. The hardness number is a derivative indicating the relationship between the applied load and the surface area of the indentation.

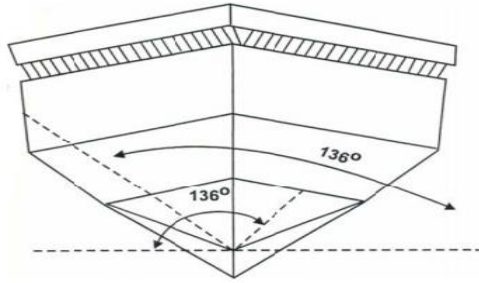


Figure 43. Vickers's pyramidal indenter.

Vickers hardness number measurements were performed on every sample using a Vickers's hardness test machine (MicroMet® 5124 Micro-indentation Hardness Tester), as shown in Figure 44, at room temperature with 1 kg load. This equipment adjusts the sample and permits the indenter to contact easily beneath the predetermined load, which is in contact for a fixed period. The essential element of this equipment is a measuring microscope mounted on the machine to compute the hardness value of the indented specimen located in the optical field.

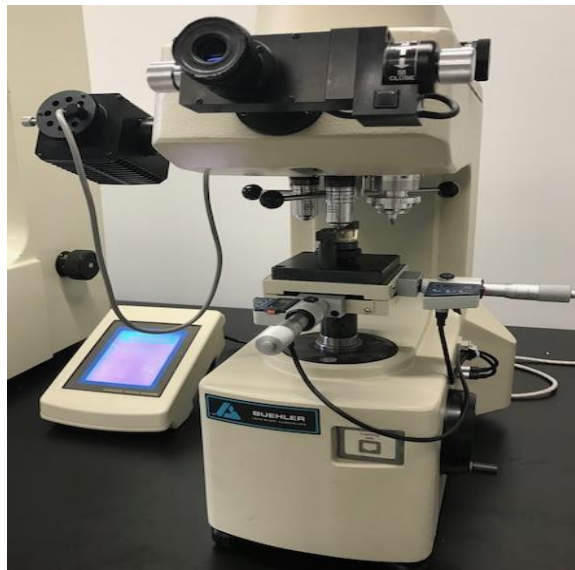


Figure 44. Vickers microhardness test machine.

A square-based pyramidal diamond indenter was used to make five indentations in each specimen: middle center, top left, top right, bottom left, and bottom right. All indentations were equally spaced, therefore contributing to the sample's value based on the standard deviation of

the samples. The two diagonals of the indentations were denoted to the closest 0.1- μm with a filer micrometer, and the mean was intended. Hardness was engaged as the maximum force divided by the area of contact. The HV WAS calculated using the following formula:

$$HV = \frac{1.8544P}{d^2} \quad (3.1)$$

where the load P is in kg, and the average diagonal d is in mm (this produces the hardness number units of kg/ mm²; in practice, the numbers are reported without suggestion of the units).

3.1.14 Ice Cube

In this study, an ice cube, as shown in Figure 45, was primarily used to produce ice on top of the plasma-treated SH-coated AA 2024-T3 samples. Being lightweight, the base of the ice cube is attached by means of super-cooled water, which is frictionless and compatible.



Figure 45. Ice cube.

3.1.15 Inclinometer

This study including deicing and self-cleaning tests, whereby an inclinometer, as shown in Figure 46, was utilized as the central apparatus to discover the angle of tilt or the elevation as respects gravity. The reason for using an inclinometer in this study was to locate the sliding angle of the ice, and how much sliding angle and time were required to clean dust off the surface

of the plasma-treated SH-coated AA 2024-T3 samples. This equipment has a base plate with four built-in magnets for attaching with metal surfaces, which were extremely useful in this study.



Figure 46. Inclinometer.

3.1.16 Digital Anemometer

The digital anemometer, as shown in Figure 47, was utilized to determine the blown air velocity, in anticipating of the wind velocity around an aircraft. This equipment is user-friendly and ultimately employed to measure the wind speed. The temperature also can be measured from fast air movement for exploring critical environment circumstances. The jackknife design shelters the equipment and permits holding the case while taking specific temperature measurements, thereby preventing false interpretations for measuring the temperature by hand.



Figure 47. Digital anemometer.

3.1.17 Electric Blower

An electric blower, as shown in Figure 48, propels air out of a nozzle and is controlled by electric or gasoline motors. This typically independent handheld unit or backpack-mounted unit with a handheld wand provides a maximum air speed of 225 mph and air volumes up to 150 cfm for increased efficiency. The lightweight design makes it easy to handle and maneuver.



Figure 48. Electric blower.

3.1.18 Water Sprayer

A water sprayer, as shown in Figure 49, was used to sprinkle water on the plasma-treated SH-coated AA 2024-T3 sample's surface, which was covered with graphene powder, from a distance of 50 cm to find the best sliding angle to use in the self-cleaning test.



Figure 49. Water sprayer.

3.2 Experimental Methods

An objective of this research was to comprehensively study the effects of electrochemical corrosion. However, it was important to determine which plasma radio frequency level would be appropriate for the superhydrophobic coating by analyzing the contact angle measurement and patterns produced from the experimentation. Thus, SH-coated AA 2024-T3 samples that were plasma-treated with variable radio RF levels and heat treated at different temperatures were used in this study. A total of 27 samples were used, and then the contact angle measurements for all 27 samples were obtained, as shown in Figure 50.

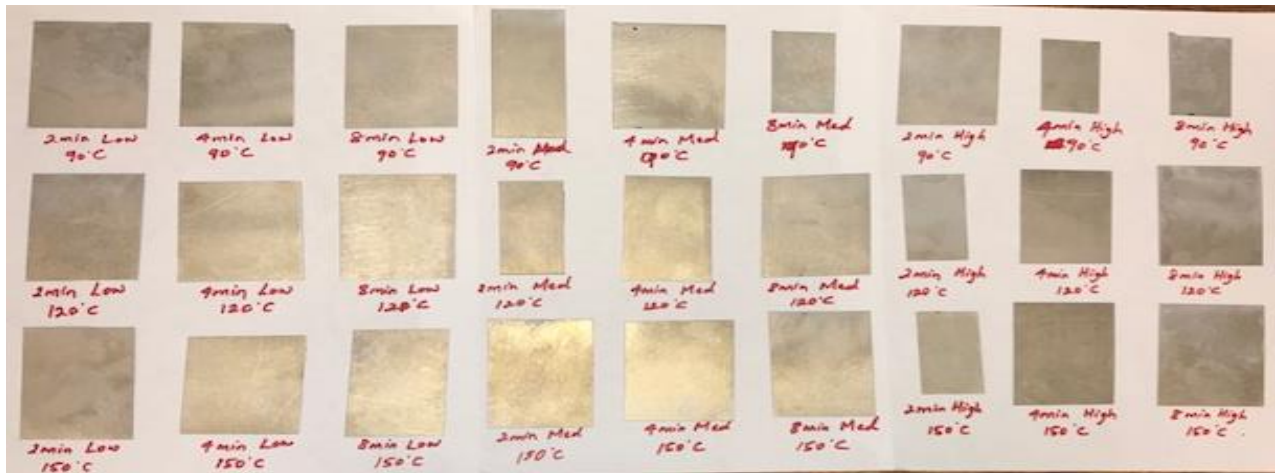


Figure 50. Twenty-seven samples plasma-treated with various RF levels and heat treated at different temperatures.

The 27 samples used for this experiment and the treatments they were subjected to are listed below:

- AA 2024-T3 surface, plasma-treated at low RF level for 2, 4, and 8 minutes, and heat-treated for 60 minutes at 90° Celsius.
- AA 2024-T3 surface, plasma-treated at low RF level for 2, 4, and 8 minutes, and heat-treated for 60 minutes at 120° Celsius.

- AA 2024-T3 surface, plasma-treated at low RF level for 2, 4, and 8 minutes, and heat-treated for 60 minutes at 150° Celsius.
- AA 2024-T3 surface, plasma-treated at medium RF level for 2, 4, and 8 minutes, and heat-treated for 60 minutes at 90° Celsius.
- AA 2024-T3 surface, plasma-treated at medium RF level for 2, 4, and 8 minutes, and heat-treated for 60 minutes at 120° Celsius.
- AA 2024-T3 surface, plasma-treated at medium RF level for 2, 4, and 8 minutes, and heat-treated for 60 minutes at 150° Celsius.
- AA 2024-T3 surface, plasma-treated at high RF level for 2, 4, and 8 minutes, and heat-treated for 60 minutes at 90° Celsius.
- AA 2024-T3 surface, plasma-treated at high RF level for 2, 4, and 8 minutes, and heat-treated for 60 minutes at 120° Celsius.
- AA 2024-T3 surface, plasma-treated at high RF level for 2, 4, and 8 minutes, and heat-treated for 60 minutes at 150° Celsius.

From these 27 samples, those with the four best contact angles were identified. After that, the tape adhesive test was performed to check the robustness of the superhydrophobic coating, and then the four best samples were immersed in 3% 0.5M NaCl solution for 30-day time periods. The 3% 0.5M NaCl solution was used to simulate the maximum and minimum threshold of a corrosive environment. Once those experiments were concluded, the difference in corrosion resistivity of the plasma-treated SH-coated AA 2024-T3 samples was contrasted against untreated, uncoated AA 2024-T3 samples, and the essential causes in their different responses to corrosion were theoretically studied.

In the post-immersion analytic evaluation of the plasma-treated SH-coated AA 2024-T3 samples, the surfaces were diligently observed, and the critical parameters were measured. The measured variables were tabulated to generate a Tafel curve, Nyquist plot, and Bode plot. The Tafel curve, when plotted was the basis for computing the corrosion rate, based on the Tafel equation. The determination of the corrosion penetration rate (CPR) about the time elapsed was made possible by an allowance of idle intervals between the immersion and redemption of plasma-treated SH-coated AA 2024-T3 samples and untreated AA 2024-T3 samples. The corrosion patterns associated with the immersion of the samples in 3% 0.5M NaCl solution were determined from the Nyquist and Bode plots.

Following the EC analysis, an FTIR spectrometry test was done to reaffirm the adhesive durability of the coating corresponding to its adherence to the substrate; this test replicates the atomic profile involving the samples' chemical composition. The intramolecular atomic bonds between the functional groups for the adhesive, coating, and substrate were recognized. The forces keeping these bonds together are instrumental in transmitting information about the adhesive strength.

Then the Vickers hardness test was done to show that the plasma surface cleaning treatment on the AA 2024-T3 samples was not disturbing their mechanical properties. Next, the deicing test and self-cleaning test were performed to check the superhydrophobicity of the plasma-treated SH-coated AA 2024-T3 samples. The deicing test explains how a superhydrophobic surface can withstand ice that has formed on it and can be detached without difficulty. The self-cleaning test shows the significance of the self-cleaning mechanism on tilted plasma-treated SH-coated AA 2024-T3 sample surfaces that hold dust particles. The more the

plasma-treated SH-coated AA 2024-T3 sample surface is tilted, the less time and water needed to self-clean the dust particles from the plasma-treated surface.

The last few minutes of each test involved the salt soaking test, freezing time test, and super-cooled water test to check the superhydrophobicity of the plasma-treated SH-coated AA 2024-T3 samples. The following sections thoroughly explain the experimental methods used in this research.

3.2.1 Aluminum 2024-T3 Alloy Division

The AA 2024-T3 samples are the primary source in the experimental process. Their nature necessitates that congruency is applied. Therefore, all samples were machined in an identical rectangular shape and with the same 1-inch by 2-inch dimensions.

3.2.2 Cleaning of Aluminum 2024-T3 Alloy

Before the testing phase, the AA 2024-T3 samples were exposed to continuously varying environments, which resulted gradual microscopic debris and carbon buildup on the sample surfaces. The appropriate cleaning solvents for proper removal of this debris were chosen to be dish liquid detergent, ethanol, and acetone, which are depicted in Figure 51.



Figure 51. Dish liquid detergent, ethanol, and acetone.

After cleaning with all three solvents, the AA 2024-T3 samples were dried in the industrial oven for 5 minutes at 80°C. Then the samples were placed inside the ultrasonic cleaner filled with acetone for 10 minutes. After cleaning ultrasonically, the AA 2024-T3 samples were again dried in the industrial oven for 5 minutes at 80°C. Then the AA 2024-T3 samples were placed inside the ultrasonic cleaner filled with DI water for 10 minutes. After the ultrasonic cleaning, the AA 2024-T3 samples were again dried in the industrial oven for 5 minutes at 80°C.

3.2.3 Preparation of Bottom Coat

Before the application of the bottom coat, the AA 2024-T3 samples were thoroughly cleaned to ensure a minimum of dust particles and carbon. Then, the bottom-coat ingredients were mixed for 10 minutes. The Ultra-Tech 4122 Mini Sprayer was filled with the freshly prepared bottom coat, and the AA 2024-T3 samples were laid on a fume hood, oriented so that the line of incidence of the spray when the mini sprayer was handheld in their proximity was perpendicular to the panel surface.

3.2.4 Application of Bottom Coat

The two prerequisites before commencement of the bottom coating are the right-angled line of incidence of spray respective of the mini sprayer to the panel surface and more than half a foot linear distance. Once these requirements were met, a push to the trigger of the mini sprayer withdrew the bottom coat from the attached container into the nozzle of the sprayer, and ejected it onto the AA 2024-T3 samples surface, as shown in Figure 52. Caution was taken during the spraying to ensure orientation and distance from the surface was within the pre-set constraints. A medium magnitude of force was exerted on the trigger in order to regulate the spray and attain a uniform thickness for the double-layered bottom coat on the panel surface. After the bottom

coating was applied, the AA 2024-T3 samples were air dried at room temperature for two hours, before proceeding to plasma treatment.



Figure 52. Application of bottom coat.

3.2.5 Plasma Surface Cleaning Treatment

Oxygen plasma was used for plasma treating the SH-coated surface of the AA 2024-T3 samples. The primary goal here was to convey a significant quantity of activation energy to the samples' surface in order to develop corrosion resistivity between the coating and the substrate. The following procedure was used to perform the plasma treatment, as shown in Figure 53:

- First, a clean cloth, carefully inspected for any crust, was used for cleaning the plasma chamber in order to eliminate dust particles.
- The plasma chamber door against the vacuum chamber was unlocked, and the bottom coated AA 2024-T3 sample was placed in it. The plasma chamber door was closed using a needle valve.
- Then a vacuum pump switch was actuated from its switch. As a result, the air in the chamber was withdrawn gradually, and then transmuted into a widespread vacuum after a couple of minutes.
- Very low-pressure gases which are initiated by low flow rates were subjected to RF electromagnetic radiation embed plasma to be generated.

- The 27 AA 2024-T3 samples were then subjected to various predetermined levels of radio frequency—namely low, medium, and high. Nine samples were treated for two minutes, nine samples for four minutes, and then another nine samples for eight minutes.
- The plasma and surface impact varies with changes in intensity and frequency of the RF power utilized to stimulate the plasma, and affected by the types of ionized gases, the type of sample that is exposed to the plasma, and the period of exposure to the plasma.
- Once plasma treatment was completed, the plasma cleaner and vacuum pump were turned off.
- Then the plasma chamber was examined by keeping the chamber door open and deliberately rotating the needle valve to let air enter the chamber.
- The sample was then taken out and prepared for the top-coating process.



Figure 53. Plasma surface cleaning treatment procedure.

3.2.6 Preparation of Top Coat

After the plasma bottom-coating treatment, AA 2024-T3 samples were dried at room temperature for few minutes. The top-coat application was mixed for five minutes. Then the top coat was applied on the AA 2024-T3 samples using the Ultra-Tech 4122 Mini Sprayer. The samples were then patterned for any abnormalities and placed to rest on a table in the proper

alignment and linear distance of the line for the frequency of spray identical to that used in the bottom-coating process.

3.2.7 Application of Top Coat

In a few minutes, the prepared top coat was sprayed on the rested AA 2024-T3 samples. As shown in Figure 54, the samples were top coated using the Ultra-Tech 4122 Mini Sprayer. This sprayer was maintained at a constant pressure in order to generate the preferred smooth thickness. Two top coats were sprayed on the AA 2024-T3 samples with a fluid turn out of one and a half. Then the sprayed samples were dried at room temperature for two hours.



Figure 54. Application of top coat.

3.2.8 Heat Treatment of Aluminum 2024 T-3 Alloy

After top coating the AA 2024-T3 samples, they were heat treated using an industrial oven, which is available in Room 125 of Wallace Hall at WSU. All samples were heat treated for 60 minutes at temperatures of 90° Celsius, 120° Celsius, and 150° Celsius.

3.2.9 Measuring Contact Angle

The water droplet contact angles were measured using the CAM 100 series optical contact angle goniometer from KSV Instruments Limited, which is available in Room 139 of Beggs Hall at WSU. DI water was used for computing the contact angle. All contact angle tests were implemented at room temperature.

3.2.10 Tape Adhesion Test on Plasma-Treated SH Coated Samples

3M adhesive tape was used to execute the tape adhesion test on the four best plasma-treated SH-coated AA 2024-T3 samples. The purpose of this adhesion test was to determine the robustness of the highly superhydrophobic coating on the metal surface. This test also illustrates the strength of the coating and how well it adheres to the metal. Steps in the tape adhesion test are as follows:

- Plasma-treated SH-coated AA 2024-T3 samples were prepared to the equivalent procedure as mentioned previously in section 3.2.2.
- The contact angles of the plasma-treated SH-coated AA 2024-T3 samples were before applying tape.
- The 3M tape was pasted on the plasma-treated SH-coated AA 2024-T3 samples and then peeled entirely in the opposite direction at an angle of 180° to the plasma-treated SH-coated AA 2024-T3 samples, as shown in Figure 55.
- Then the contact angle was measured close to the region that had been tapped and peeled.
- This method was repetitive ten times, and the contact angle was recorded after each peeling test.

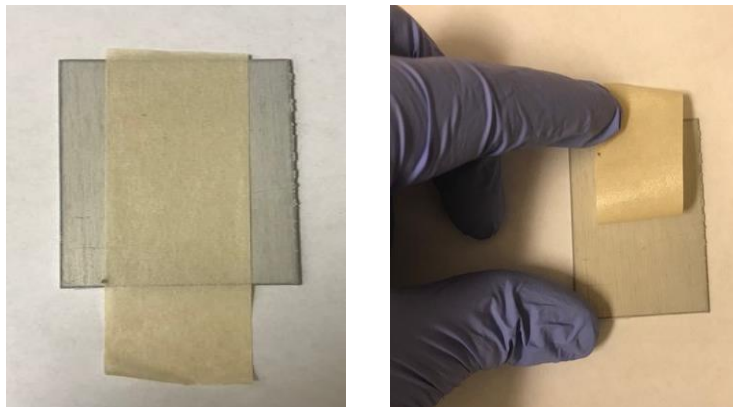


Figure 55. Tape adhesion test procedure.

3.2.11 Immersion in 3% 0.5M NaCl Solution

The plasma-treated SH-coated AA 2024-T3 samples were immersed in 3% 0.5M NaCl solution, as shown in Figure 56. Contact angles within 30 days of immersion in the solution were measured, especially with a three-day time interval, using the optical contact angle goniometer.



Figure 56. Plasma-treated aluminum samples immersed in 3% 0.5M NaCl solution.

The standard used to immerse the plasma-treated SH-coated AA 2024-T3 samples in 3% 0.5M NaCl solution was ASTM D870-15, which is the standard preparation for analyzing the corrosion resistance of a coating using saltwater immersion. The primary objective here was to immerse the samples in saltwater to define the dissimilarity between the corrosion resistance of the AA 2024-T3 samples that were plasma-treated SH-coated AA 2024-T3 samples and the AA 2024-T3 samples that were not treated, in order to distinguish how saltwater influences the corrosion-resistance properties of the substrate and coating. To perform the salt soaking test, one set of plasma-treated SH-coated AA 2024-T3 samples was immersed for 30 days in 3% 0.5M NaCl solution, and the other set of plasma-treated SH-coated AA 2024-T3 samples was immersed for 90 days in the same solution.

3.2.12 Measuring Corrosion Rate Using Polarization Curves

The corrosion rate tests were obtained for the best plasma-treated SH-coated AA 2024-T3 samples using the Gamry Reference 600 Potentiostat and Gamry Corrosion Cell, as shown in

Figure 57. This equipment was computerized using Gamry Framework, which made the work simple by generating the polarization curve to fit the corrosion rate. This machine is available in Room 139 of Beggs Hall at WSU.

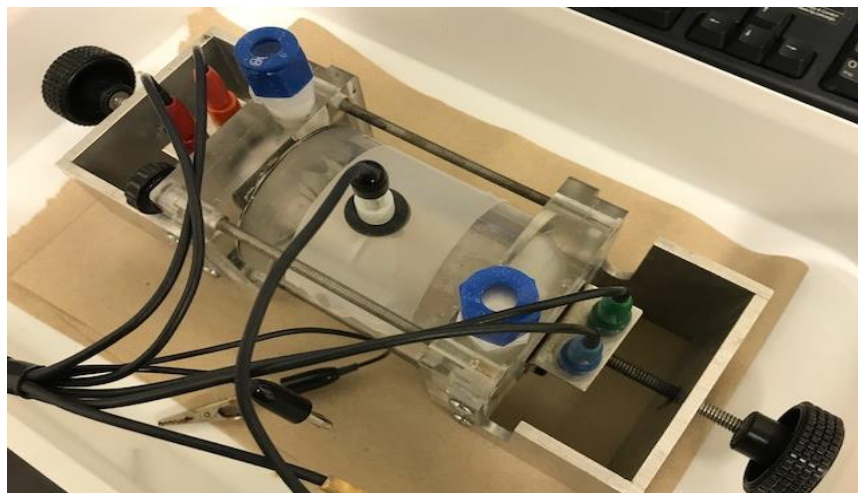


Figure 57. Plasma-treated aluminum samples using Gamry reference 600 potentiostat.

The following procedure was used to perform to obtain the PC to measure the corrosion rate:

- First, one of the plasma-treated SH-coated AA 2024-T3 samples was placed into the working counter of the Gamry Corrosion Cell.
- The 3% 0.5M NaCl testing solution was dispensed into the Gamry Corrosion Cell up to the black-marked level.
- All sensor connections were connected between the Gamry Cell and the Gamry Reference 600 to ensure the sensor color code.
- Then the separate saturated calomel reference electrode was added into the Gamry Corrosion Cell.
- The Gamry Cell Framework software was opened, the potentiodynamic test option was selected, and all parameters were input, including limit voltages, density and equivalent

weight of AA 2024-T3 material, scan rate, sample period, Gamry Corrosion Cell hole area of 4.89 cm², etc., in order to obtain the PC, which is known as the Tafel curve.

- Using the analysis section of the software and from the Tafel curve, the corrosion penetration rates were obtained automatically by fitting the Tafel curve from its first and last points correctly.
- The corrosion rates of particular plasma-treated SH-coated AA 2024-T3 samples were immersed in 3% 0.5M NaCl solution and tested every three days by utilizing all of the above testing measures, in order to obtain the Tafel curves.

3.2.13 Electrochemical Analysis Using Electrochemical Impedance Spectroscopy

The EIS results were achieved for best plasma-treated SH-coated AA 2024-T3 samples using the Gamry Reference 600 Potentiostat. This equipment's Gamry Framework software is very convenient for generating Nyquist and Bode plots, which are the primary plots to demonstrate the EC analysis of the plasma-treated SH-coated AA 2024-T3 samples.

The following procedure was used to execute the Nyquist and Bode plots to analyze the electrochemical impedance spectroscopy:

- First, one of the plasma-treated SH-coated AA 2024-T3 samples was placed into the working counter of the Gamry Corrosion Cell.
- The 3% 0.5M NaCl testing solution was dispensed into the Gamry Corrosion Cell up to the black-marked level.
- All sensor connections were connected between the Gamry Corrosion Cell and Gamry Reference 600 to ensure the sensor color code.
- In the Gamry Framework software, the potentiostatic option was opened, and after given the input parameters, i.e., frequency range, similar to the Tafel curve, the test was

performed, and Nyquist and Bode plots were drawn, which sustained a dependability test of the corrosion performance.

- The EIS analysis for each plasma-treated SH-coated AA 2024-T3 sample involved immersion in a 3% 0.5M NaCl solution and tested every three days by utilizing all of the above testing measures, in order to obtain the Nyquist and Bode plots.
- After the EC corrosion tests, the best samples were immersed in DI water to further study the corrosion rate relative to time. These EC corrosion tests of each particular sample in each solution were done every three days for 30 days by following all of the above testing procedures in order to obtain the Tafel curves. The same procedures were developed for all samples in order to also obtain the Nyquist and Bode plots.

3.2.14 Performing Fourier Transform Infrared Analysis

Fourier transform infrared spectroscopy analysis was used for the characterization of plasma-treated SH-coated AA 2024-T3 samples and only the bare uncoated AA 2024-T3 sample. FTIR spectroscopy utilizes infrared radiation that is passed through a sample. Initially, the wavenumber is measured with respect to background sample, in this case the bare uncoated AA 2024-T3 sample. Then the resulting reflectance, transmission or absorption peaks, were obtained to clarify the molecular identification of the samples. Attenuated total reflectance (ATR) spectroscopy, one of the FTIR reflectance techniques was utilized to characterize the structure of the samples, and spectra were collected between the wavenumbers of 400 and 4000 cm^{-1} .

3.2.15 Measuring Vickers Hardness Number

The Vickers hardness test was performed to show that the plasma-treated SH-coated AA 2024-T3 samples are mechanically stable. The plasma cleaning technique does not change the

samples' mechanical properties. In this test, the hardness of the sample was measured at the microscopic level. This test involved the following steps:

- The Vickers hardness testing machine was turned on, and the plasma-treated SH-coated AA 2024-T3 sample was placed on the anvil.
- The centering light was set up on the sample, lining it up to the lower magnification (50M). While adjusting the magnification, the sample is examined to find a region that is free of abrasions and secondary phases.
- The two black lines seen must be merged using the eyepiece to make only one line.
- The base with the sample was moved up to the indenter, and the “indent” button was pressed in order to indent the sample with less force.
- Then the base was lowered so the sample would fit within the larger magnification, which was close to 10M, as shown in Figure 58.
- The sample and diamond indent were centered, and the two black lines were placed at the side ends of the diamond from the vertical direction.
- The black button on the eyepiece was pressed, and the eyepiece was revolved to 90°.
- The two black lines were placed at the top ends of the diamond in the horizontal direction, and again the black button on the eyepiece was pressed.
- Following these procedures, the Vickers hardness testing machine automatically formulated the Vickers hardness number, which was displayed on the screen.

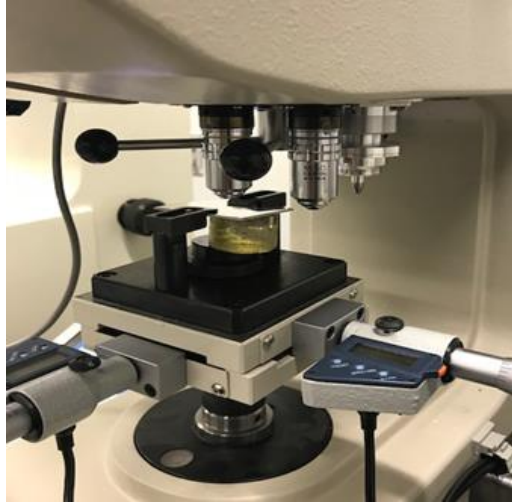


Figure 58. Plasma-treated AA 2024-T3 sample within magnification close to 10M.

3.2.16 Preparing Ice Cubes for Deicing Test

The deicing test shows how a superhydrophobic surface can withstand ice that has molded on it and can be detached without difficulty. In this research, ice was formed on top of the plasma-treated SH-coated AA 2024-T3 samples using ice cubes. Next, the same samples were kept in a freezer, which is located in the Room 139 of Beggs Hall at WSU, for nearly 30 minutes. Then the sliding angles of the ice were measured using an inclinometer and the contact angle of the AA 2024-T3 sample. The following procedure was used to form the ice for the deicing test:

- A plastic tray full of water was kept in the freezer in order to change the water into super-cooled water so that it would freeze rapidly. This step was done for two hours, and ice cubes were obtained.
- Then one ice cube was placed on top of the plasma-treated SH-coated AA 2024-T3 sample, and a small amount of super-cooled water was dispensed onto the ice cube to increase the adhesiveness of the ice cube to the AA 2024-T3 sample.

- Finally, the AA 2024-T3 sample was kept in the freezer for 30 minutes with the ice forming on top of it, and then this sample was used to run the tests.

3.2.17 Performing Deicing Test with Ice Cubes

The prepared ice cube was placed on top of the plasma-treated SH-coated AA 2024-T3 sample and positioned on a base composite plate with the inclinometer, as shown in Figure 59. The inclinometer was used to find different angles on the AA 2024-T3 sample until the formed ice cube fell away from the plasma-treated SH-coated AA 2024-T3 sample and the sliding angles were obtained. The contact angle measurement was taken on the plasma-treated SH-coated AA 2024-T3 sample after each deicing test.



Figure 59. Ice cube kept on top of plasma-treated AA 2024-T3 sample.

3.2.18 Performing Air Blower Test on Formed Ice Cube at Different Angles (0°, 5°, 10°, and 20°)

The plasma-treated SH-coated AA 2024-T3 sample with the formed ice cube on top of it was taped to the ground, and air was blown across it using the electric blower at a speed of 55.15 m/s at a temperature of 23.7°C, as shown in Figure 60. From this test, the time it took for the ice to be removed from the AA 2024-T3 sample after turning on the electric air blower was measured at three different angles 0°, 5°, 10°, and 20°. The contact angle was measured on the plasma-treated SH-coated AA 2024-T3 sample after each air blower test.



Figure 60. Electric air blower for removing ice.

3.2.19 Performing Salt Soaking Test

This test was used to check the electrochemical analysis of the plasma-treated SH-coated AA 2024-T3 samples by entirely immersing them into a glass beaker with a 3% 0.5 M NaCl solution for 90 days at room temperature, as shown in Figure 61. After 90 days, the samples were taken from their glass beakers and evaluated for contact angle measurement, polarization curve measurement, and EIS measurement.



Figure 61. Plasma-treated AA 2024-T3 samples immersed in glass beaker with 3% 0.5 M NaCl solution for 90 days.

3.2.20 Performing Freezing Time Test

One drop of water droplet was dropped on both the plasma-treated SH-coated AA 2024-T3 sample and uncoated AA 2024-T3 sample, as shown in Figure 62, and both samples were kept in the freezer for 30 minutes. Then the AA 2024-T3 samples were taken from the freezer, snapped, and visually assessed for comparison between the plasma-treated SH-coated AA 2024-T3 sample and uncoated AA 2024-T3 sample.



Figure 62. One drop of water applied to both plasma-treated AA 2024-T3 sample (left) and uncoated AA 2024-T3 sample (right).

3.2.21 Performing Super-Cooled Water Test

This test was performed to demonstrate how the super-cooled water stays on the plasma-treated SH-coated AA 2024-T3 sample. As mentioned, the super-cooled water was dispensed on both the plasma-treated SH-coated AA 2024-T3 sample and uncoated AA 2024-T3 sample. After that, images were recorded and the comparison between the plasma-treated SH-coated AA 2024-T3 sample and uncoated AA 2024-T3 sample were evaluated.

3.2.22 Performing Self-Cleaning Test

The self-cleaning test demonstrates the importance of the self-cleaning mechanism on tilted plasma-treated SH-coated AA 2024-T3 sample surfaces relative to dust particles. In this

study, graphene powder was used as dust particles. The more the plasma-treated SH-coated AA 2024-T3 sample surface is tilted, the less time and water is used to self-clean the dust particles from the surface. This experiment took the following steps, as shown in Figure 63:

- A water sprayer was utilized to apply the water to the plasma-treated SH-coated AA 2024-T3 sample surface, at a separated distance of 50 cm, to check the best sliding angle for self-cleaning.
- Graphene was used in place of dirt in this research because it remained on the AA 2024-T3 sample's surface. Graphite powder was peppered on top of the AA 2024-T3 sample surface.
- After water touched the AA 2024-T3 sample surface, it rolled off, moving the graphite powder along with it.
- The number of times that had been water sprayed on the AA 2024-T3 sample's surface was recorded, and the same process on the same surface at different tilt angles (5°, 10°, 20°, 40° and 60°) was repeated.



Figure 63. Self-cleaning test method.

CHAPTER 4

RESULTS AND DISCUSSION

4.1 Contact Angle Measurement

The contact angles of all plasma-treated SH-coated AA 2024-T3 samples were measured using the CAM 100 goniometer. This machine has a compacted charge coupled device camera, which documented the picture of the AA 2024-T3 samples. After the AA 2024-T3 samples were placed on goniometer's platform, a droplet of DI water was positioned on the aluminum sample surface using a syringe needle.

4.1.1 CA Results of All 27 Plasma-Treated SH-Coated AA 2024-T3 Samples

The contact angles of all initial 27 plasma-treated SH-coated AA 2024-T3 samples were measured to determine which plasma RF level would be suitable for a superhydrophobic coating. These measurements are shown in Table 4.

TABLE 4

INITIAL CONTACT ANGLE MEASUREMENT FOR ALL 27 PLASMA-TREATED SH-COATED AA 2024-T3 SAMPLES

Heat Temp.	Time (min)	RF Level	Middle Center	Top Left	Top Right	Bottom Left	Bottom Right	Average	Rank
90	2	Low	153.43	128.75	141.94	162.31	148.21	146.93	26
120	2	Low	151.26	138.26	142.56	160.20	149.89	148.43	25
150	2	Low	159.56	143.51	152.05	167.82	153.12	155.21	22
90	4	Low	166.49	152.83	161.46	156.52	157.75	159.01	12
120	4	Low	164.26	154.12	159.56	154.26	158.42	158.12	15
150	4	Low	164.36	143.15	159.38	152.41	143.81	152.62	23

TABLE 4 (continued)

Heat Temp.	Time (min)	RF Level	Middle Center	Top Left	Top Right	Bottom Left	Bottom Right	Average	Rank
90	8	Low	161.67	156.66	152.66	146.57	163.29	156.17	19
120	8	Low	159.24	154.23	154.89	148.63	161.23	155.64	21
150	8	Low	152.42	163.80	161.75	155.42	163.44	159.37	10
90	2	Medium	164.92	131.99	161.99	135.41	156.07	150.08	24
120	2	Medium	162.84	135.46	158.54	138.56	158.46	150.77	23
90	4	Medium	158.78	156.52	160.05	156.13	159.56	158.21	14
120	4	Medium	156.78	158.42	161.50	155.21	158.51	158.08	16
150	4	Medium	165.19	160.66	161.68	164.01	163.07	162.92	4
90	8	Medium	159.86	162.09	158.82	158.14	160.68	159.92	6
120	8	Medium	159.25	161.25	161.23	156.23	159.65	159.52	9
150	8	Medium	172.77	167.15	172.42	155.89	166.74	166.99	3
90	2	High	152.32	158.03	163.73	159.00	165.10	159.64	8
120	2	High	151.23	159.43	161.23	160.25	163.25	159.08	11
150	2	High	158.45	158.77	146.32	161.04	154.52	155.82	20
90	4	High	156.59	156.07	157.67	156.73	157.88	156.99	18
120	4	High	157.26	157.05	156.46	156.23	158.64	157.13	17
150	4	High	169.43	166.30	162.69	168.32	169.96	167.34	2
90	8	High	156.76	164.30	159.12	158.13	161.10	159.88	7
120	8	High	158.46	163.41	161.23	160.23	162.15	161.10	5
150	8	High	171.96	167.30	164.69	168.32	170.43	168.54	1

From Table 4, it can be seen that all of the plasma-treated SH-coated AA 2024-T3 samples are superhydrophobic. However, for experimental purposes, only four samples were chosen for further investigation. The 8 minutes high and medium plasma-treated and 4 minutes high and medium plasma-treated AA 2024-T3 samples were chosen with a heat treatment temperature of 150°C. As shown in Table 4, the 8 minutes high and 8 minutes medium plasma-treated SH-coated AA 2024-T3 samples showed the highest contact angle of 168.54° and second highest contact angle of 166.99°, respectively.

4.1.2 CA Results of Four Best Plasma-Treated SH-Coated AA 2024-T3 Samples

The contact angles of the four best plasma-treated SH-coated AA 2024-T3 samples were measured, and the results indicate that the plasma surface cleaning treatment makes the AA 2024-T3 surface exceptionally superhydrophobic, as shown in Figure 64. These four best AA 2024-T3 samples were used for further testing.

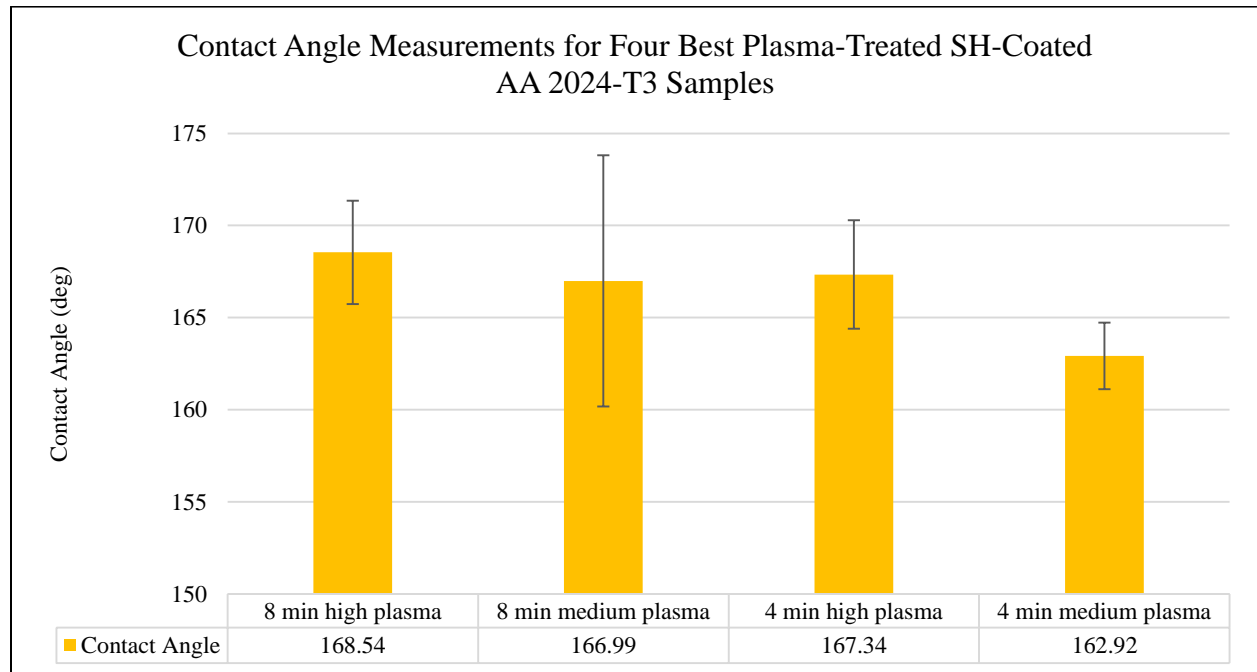


Figure 64. Contact angle measurements for four best plasma-treated SH-coated AA 2024-T3 samples.

4.1.3 CA Results of Four Best Plasma-Treated SH-Coated AA 2024-T3 Samples After Tape Adhesive Test

The contact angles of the four best plasma-treated SH-coated AA 2024-T3 samples were measured before and after the tape adhesive test, which helps to measure the adhesion of a coating on the surface. Figure 65 shows that the contact angles of these four best plasma-treated SH-coated AA 2024-T3 samples marginally decreased after ten peel tests. However, the contact angle results after ten peel tests show that these samples had a highly robust superhydrophobic coating on their surfaces. The contact angle measurements of the four best plasma-treated SH-coated AA 2024-T3 samples after the tape adhesive test are shown in Table 5.

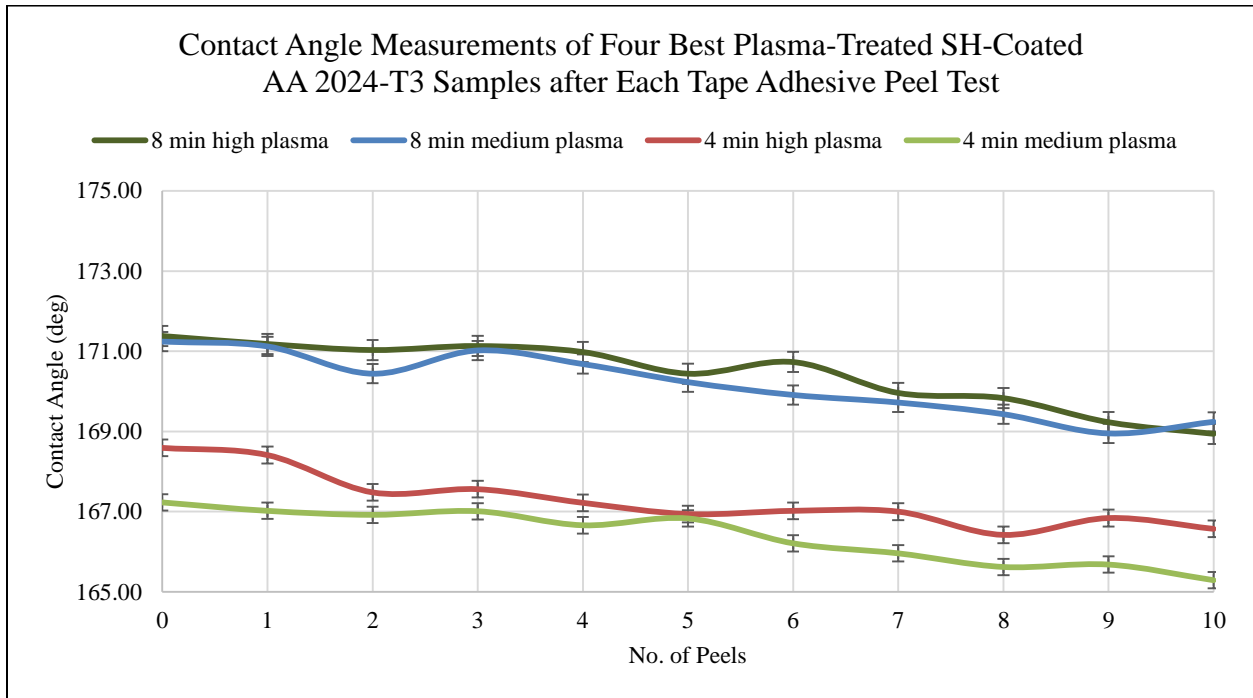


Figure 65. Contact angle measurements of four best plasma-treated SH-coated AA 2024-T3 samples after each tape adhesive peel test.

TABLE 5

CONTACT ANGLE MEASUREMENTS OF FOUR BEST PLASMA-TREATED SH-COATED AA 2024-T3 SAMPLES AFTER EACH TAPE ADHESIVE PEEL TEST

No. of Peels	8 min High Plasma	8 min Medium Plasma	4 min High Plasma	4 min Medium Plasma
0	171.38	171.24	168.59	167.23
1	171.18	171.12	168.41	167.02
2	171.03	170.44	167.48	166.92
3	171.13	171.02	167.56	167.01
4	170.98	170.68	167.22	166.66
5	170.44	170.23	166.94	166.83
6	170.73	169.91	167.02	166.21
7	169.96	169.72	167.00	165.96
8	169.83	169.43	166.42	165.62
9	169.23	168.95	166.84	165.68
10	168.94	169.24	166.57	165.29

4.1.4 CA Results of Plasma-Treated SH-Coated AA 2024-T3 Samples Immersed in 3% 0.5M NaCl Solution for 30 Days

The contact angles results of the plasma-treated SH-coated AA 2024-T3 samples immersed in 3% 0.5M NaCl solution for 30 days are shown in Table 6.

TABLE 6

CONTACT ANGLE MEASUREMENTS OF FOUR BEST PLASMA-TREATED SH-COATED AA 2024-T3 SAMPLES IMMERSED IN 3% 0.5M NaCl SOLUTION FOR 30 DAYS

Immersion Days	8 min High Plasma	8 min Medium Plasma	4 min High Plasma	4 min Medium Plasma
0	168.54	166.99	167.34	162.92
3	167.87	168.18	161.64	161.36
6	166.00	165.81	161.86	157.67
9	164.44	167.36	160.39	156.24
12	163.74	163.24	160.36	154.75
15	163.07	162.17	159.54	153.62
18	161.13	160.61	158.57	151.01
21	160.72	160.26	156.18	149.23
24	160.43	158.25	155.26	148.17
27	160.72	158.12	155.66	145.40
30	157.36	156.15	154.84	144.10

From Figure 66, it can be seen that the plasma-treated SH-coated AA 2024-T3 samples had very little difference in contact angles as the immersion time in 3% 0.5M NaCl solution was increased. From the results, the 8 minutes high and medium plasma-treated SH-coated AA 2024-T3 sample retained their superhydrophobic coated surfaces when immersed in 3% 0.5M NaCl solution for 30 days. The contact angle value of the 8 minutes high plasma-treated SH-coated AA 2024-T3 sample at 0 days is 168.54° and after 30 days drops to 157.36°, which reflects that the contact angle dropped only 10° in 30 days.

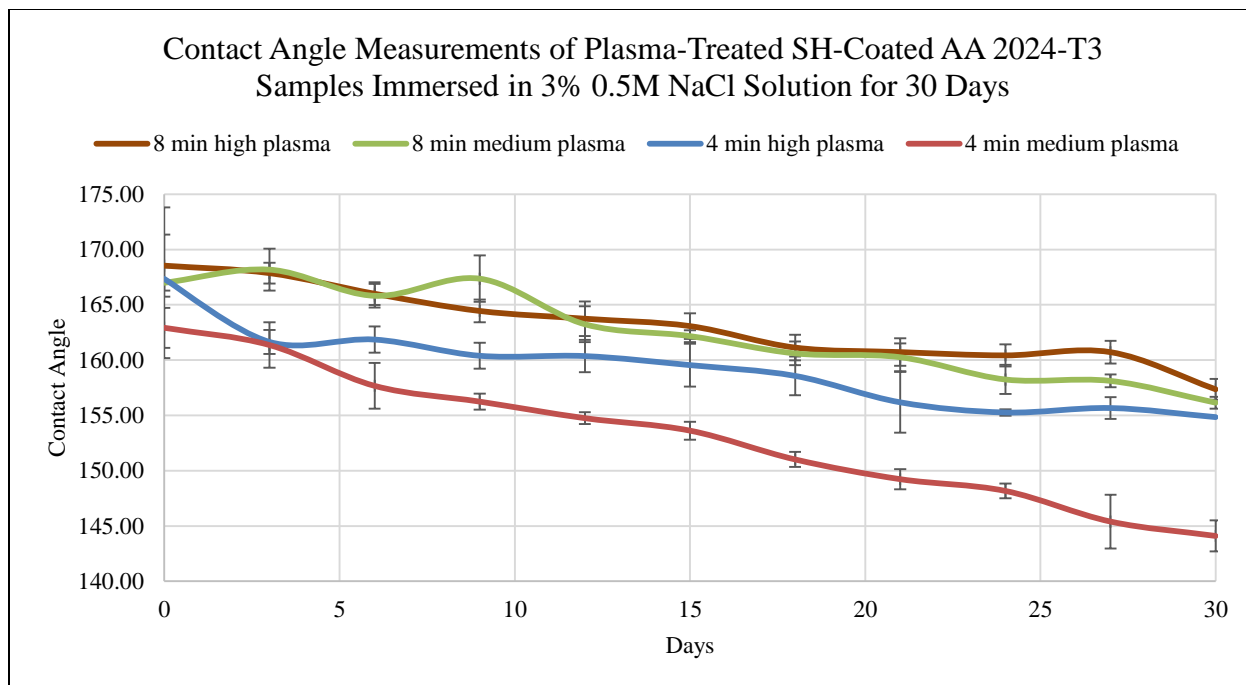


Figure 66. Contact angle measurements of plasma-treated SH-coated AA 2024-T3 samples immersed in 3% 0.5M NaCl solution for 30 days.

4.1.5 CA Results of Plasma-Treated SH-Coated AA 2024-T3 Samples Immersed in DI Water for 30 days

The contact angles results of the plasma-treated SH-coated AA 2024-T3 samples immersed in DI water for 30 days are shown in Table 7.

TABLE 7

CONTACT ANGLE MEASUREMENTS OF FOUR BEST PLASMA-TREATED SH-COATED AA 2024-T3 SAMPLES IMMERSSED IN DI WATER FOR 30 DAYS

Immersion Days	8 min High Plasma	8 min Medium Plasma	4 min High Plasma	4 min Medium Plasma
0	171.82	171.62	168.09	167.09
3	170.94	171.28	167.96	166.58
6	171.16	171.33	167.02	166.19
9	170.65	170.63	166.56	165.06

TABLE 7 (continued)

Immersion Days	8 min High Plasma	8 min Medium Plasma	4 min High Plasma	4 min Medium Plasma
12	170.08	168.41	166.47	164.62
15	168.31	168.02	165.77	163.88
18	168.56	167.32	164.55	163.00
21	168.46	166.95	165.31	161.31
24	167.89	166.71	162.44	160.78
27	167.23	167.05	162.37	160.56
30	167.04	165.10	161.54	160.19

As shown in Figure 67, the plasma-treated SH-coated AA 2024-T3 samples had little difference in contact angles as the immersion time in DI water was increased. These results indicate that the superhydrophobic coated surface was not affected by the DI water. From the results, the 8 minutes high and medium plasma-treated SH-coated AA 2024-T3 samples and 4 minutes high and medium plasma-treated SH-coated AA 2024-T3 samples retained their superhydrophobic coated surfaces when immersed in DI water for 30 days. The contact angle value of the 8 minutes high plasma-treated SH-coated AA 2024-T3 sample at 0 days is 171.82° and after 30 days drops to 167.04°, which reflects that the contact angle dropped only 4° in 30 days, which is minimal compared contact angle results of samples exposed to the aggressive NaCl solution.

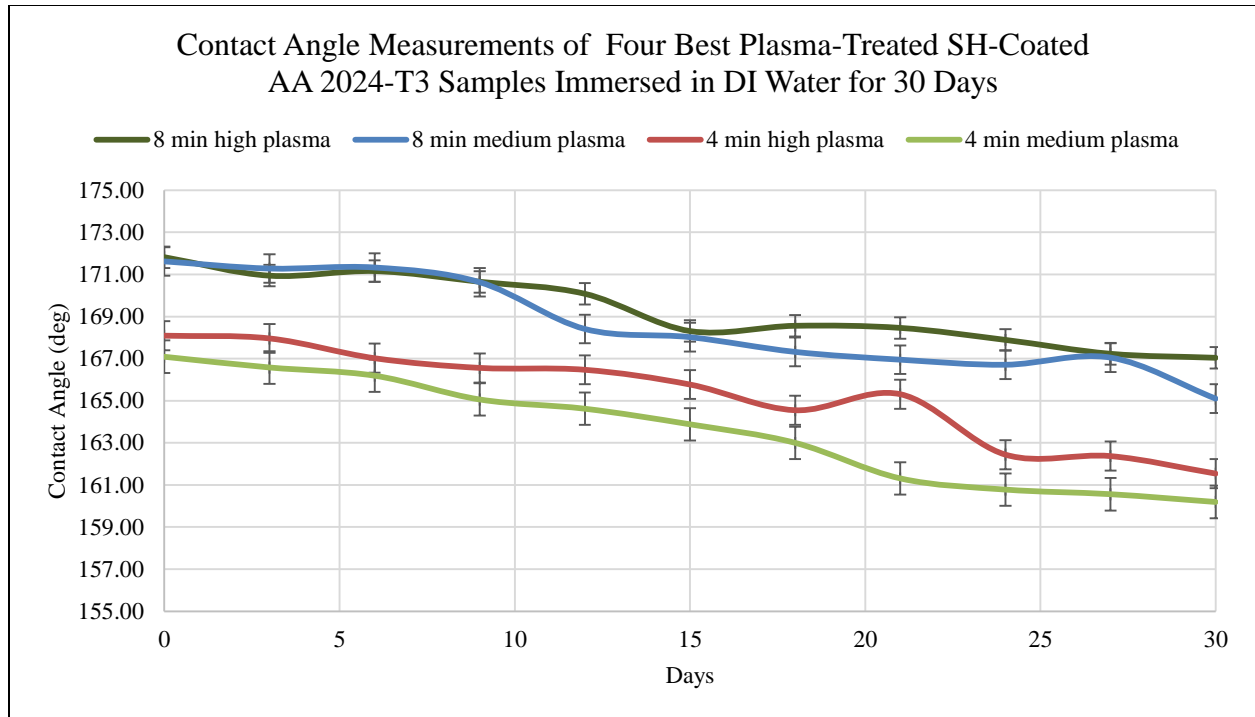


Figure 67. Contact angle measurements of four best plasma-treated SH-coated AA 2024-T3 samples immersed in DI water for 30 days.

4.1.6 Comparison of CA Results of Uncoated, SH-Coated, and Plasma-Treated SH-Coated AA 2024-T3 Samples

The comparison of contact angle results of uncoated, SH-coated, and plasma-treated SH-coated AA 2024-T3 samples are shown in Figure 68, which indicates that plasma-treated SH-coated AA 2024-T3 samples have maximum contact angle results compared to SH-coated, and uncoated AA 2024-T3 samples, which is the primary objective of this study. The plasma-treated SH-coated AA 2024-T3 samples replicate the best contact angle result of 168.54° , which is nearly 16° higher than the SH-coated AA 2024-T3 sample and 100° higher than the uncoated AA 2024-T3 sample.

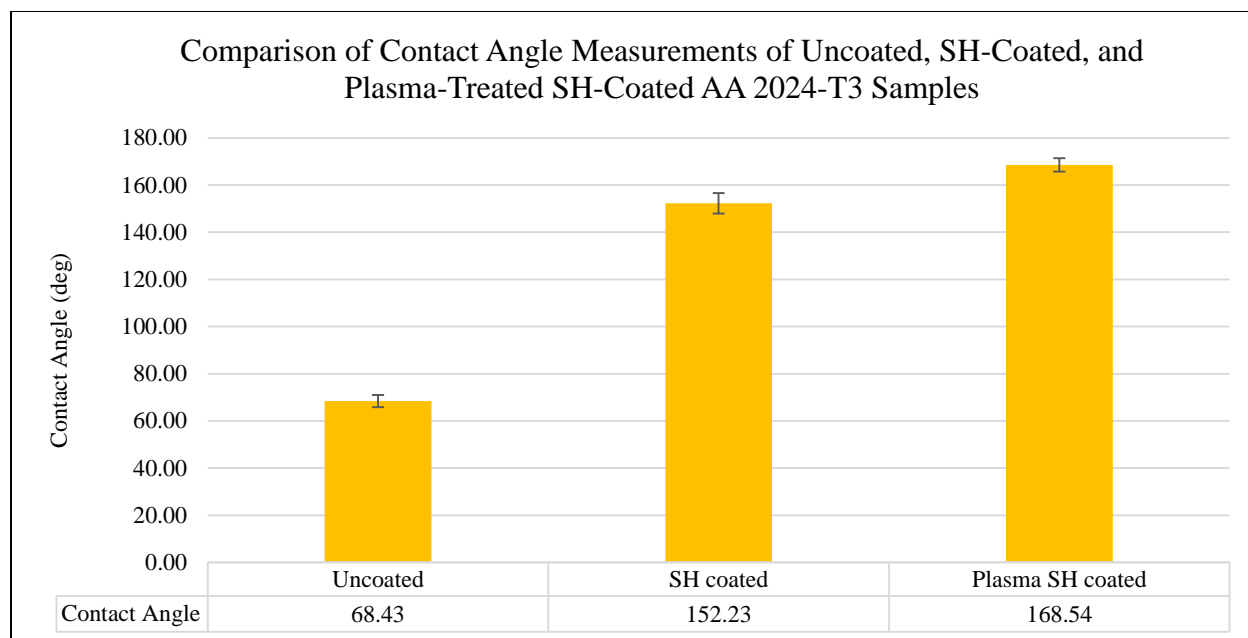


Figure 68. Comparison of contact angle measurements of uncoated, SH-coated, and plasma-treated SH-coated AA 2024-T3 samples.

4.2 Electrochemical Analysis Using Polarization Curves

Electrochemical analysis using polarization curves was done periodically on plasma-treated SH-coated AA 2024-T3 samples immersed in the 3% 0.5M NaCl solution for the increasingly extended period over 30 days. EC analysis using PCs is informal and accurate for defining the corrosion behavior as well as corrosion rate of the plasma-treated SH-coated AA 2024-T3 samples in 3% 0.5M NaCl solution to determine their life expectancy. Evaluating the corrosion rate helps decide about the life of the sample, and can be compared with a substantial amount of time and money based on its usage.

4.2.1 PC Results of Four Best Plasma-Treated SH-Coated AA 2024-T3 Samples

Polarization curve results of the four best plasma-treated SH-coated AA 2024-T3 samples show the impact of plasma surface cleaning treatment on preventing corrosion. From these four samples, the 8 minutes high plasma-treated SH-coated AA 2024-T3 sample has the highest value. Corrosion rates along with E_{corr} and I_{corr} obtained from Tafel curves are shown in

Table 8 for four best plasma-treated SH-Coated AA 2024-T3 samples. Figure 69 shows Tafel curves for the four best plasma-treated SH-coated AA 2024-T3 samples.

TABLE 8
CORROSION RATE PARAMETERS OF FOUR BEST PLASMA-TREATED SH-COATED AA 2024-T3 SAMPLES

Category	CR (mpy)	E _{corr} (V)	I _{corr} (A)
8 min High Plasma	9.534E-07	2.240	1.090E-11
8 min Medium Plasma	1.712E-06	3.770	1.950E-11
4 min High Plasma	2.261E-06	3.770	2.580E-11
4 min Medium Plasma	8.033E-05	3.720	9.150E-10

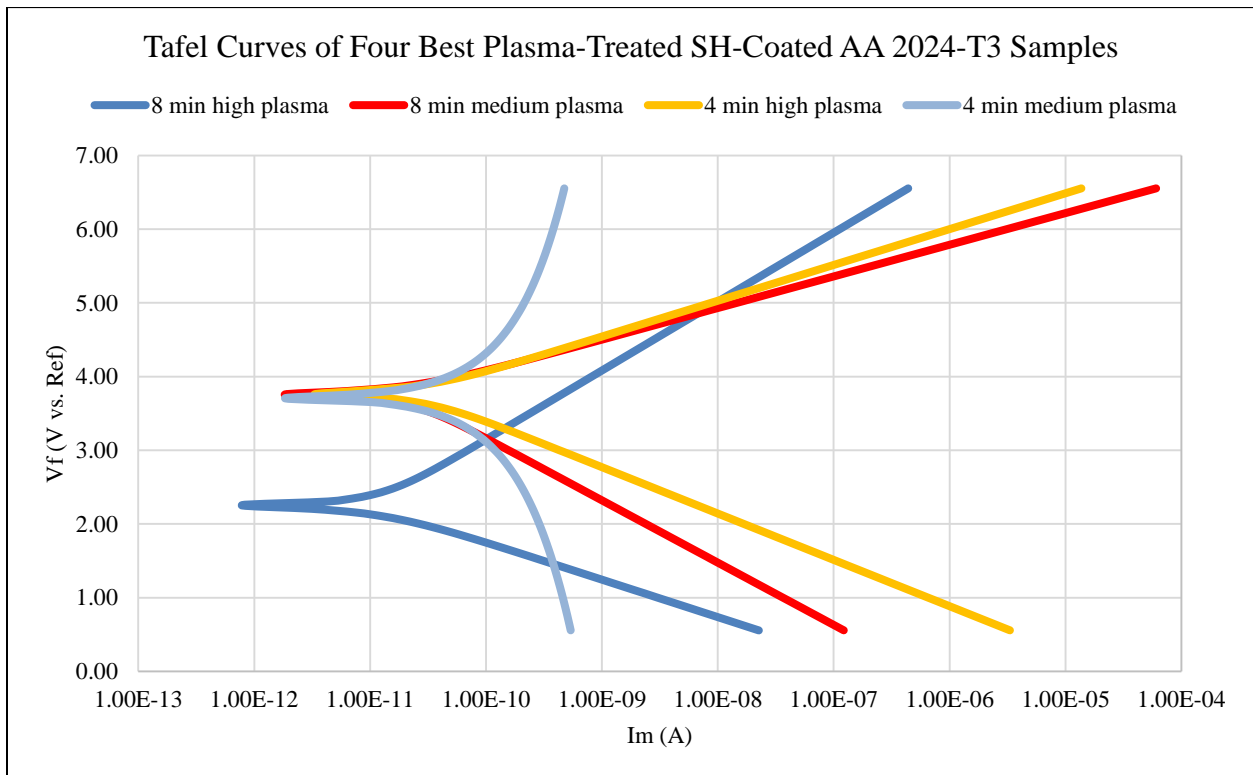


Figure 69. Tafel curves of four best plasma-treated SH-coated AA 2024-T3 samples.

4.2.2 PC Results of 8 Minutes High RF Level Plasma-Treated SH-Coated AA 2024-T3 Samples Immersed in 3% 0.5M NaCl Solution for 30 Days

PC results after the plasma-treated SH-coated AA 2024-T3 sample immersed in 3% 0.5M NaCl solution for 30 days clearly demonstrate that the 8 minutes high plasma-treated SH-coated AA 2024-T3 sample has the greatest corrosion performance at the beginning of the immersion time, which has a maximum corrosion rate of $4.492\text{E-}07$ mpy was found 0 days of immersion in the 3% 0.5M NaCl solution, and $3.774\text{E-}03$ mpy was found after 30 days of immersion. As the immersion time extends to 30 days, this sample rarely begins to lose their coating performance, which shows that there is no some degree of degradation in the coating materials, when immersed in 3% 0.5M NaCl solution for 30 days. Figure 70 shows the 8 minutes high plasma-treated SH-coated AA 2024-T3 sample's Tafel curve for the 30 days. Corrosion rates along with E_{corr} and I_{corr} is obtained from Tafel curves are shown in Table 9 for the 8 minutes high plasma-treated SH-coated AA 2024-T3 sample immersed in 3% 0.5M NaCl solution for 30 days.

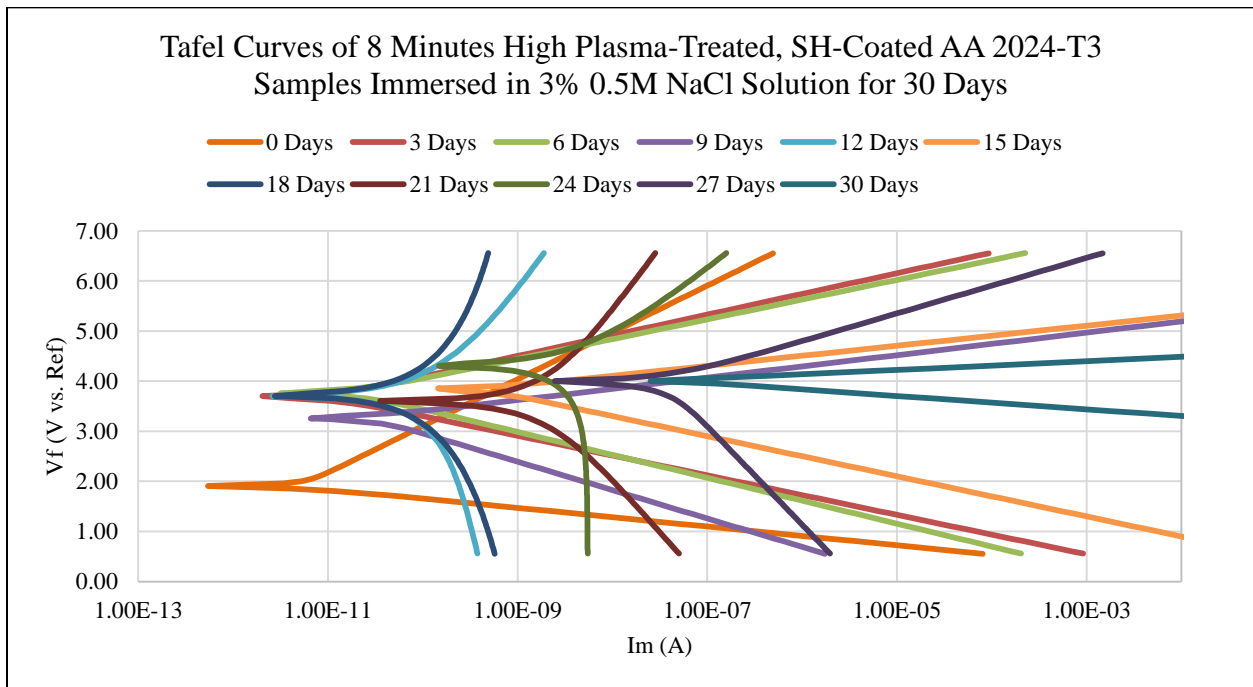


Figure 70. Tafel curves of 8 minutes high plasma-treated SH-coated AA 2024-T3 samples immersed in 3% 0.5M NaCl solution for 30 days.

TABLE 9

CORROSION RATE PARAMETERS OF 8 MIN HIGH PLASMA-TREATED SH-COATED AA 2024-T3 SAMPLES IMMERSSED IN 3% 0.5M NACL SOLUTION FOR 30 DAYS

Immersion Days	CR (mpy)	E _{corr} (V)	I _{corr} (A)
0	4.492E-07	1.900	5.120E-12
3	9.336E-07	3.690	1.060E-11
6	1.711E-06	3.770	1.950E-11
9	2.449E-06	3.270	2.790E-11
12	1.578E-05	3.720	1.800E-10
15	4.050E-05	3.840	4.610E-10
18	7.979E-05	3.720	9.090E-10
21	1.672E-04	3.590	1.900E-09
24	4.827E-04	4.320	5.500E-09
27	3.103E-03	3.990	3.530E-08
30	3.774E-03	4.020	4.300E-08

4.2.3 PC Results of 8 Minutes Medium RF Level Plasma-Treated SH-Coated AA 2024-T3 Samples Immersed in 3% 0.5M NaCl Solution for 30 Days

PC results after the plasma-treated SH-coated AA 2024-T3 sample immersed in 3% 0.5M NaCl solution for 30 days clearly demonstrate that the 8 minutes medium plasma-treated SH-coated AA 2024-T3 sample has the second highest corrosion performance with respect to the immersion time, which has a maximum corrosion rate of 8.747E-06 mpy was found 0 days of immersion in the 3% 0.5M NaCl solution, and 7.862E-03 mpy was found after 30 days of immersion. As the immersion time extends to 30 days, this sample initiates to lose their coating, which displays that there is some grade of delamination in the coating materials, when immersed

in 3% 0.5M NaCl solution for 30 days. Figure 71 shows the 8 minutes medium plasma-treated SH-coated AA 2024-T3 sample's Tafel curve for the 30 days. Corrosion rates along with E_{corr} and I_{corr} is obtained from Tafel curves are shown in Table 10 for the 8 minutes medium plasma-treated SH-coated AA 2024-T3 sample immersed in 3% 0.5M NaCl solution for 30 days.

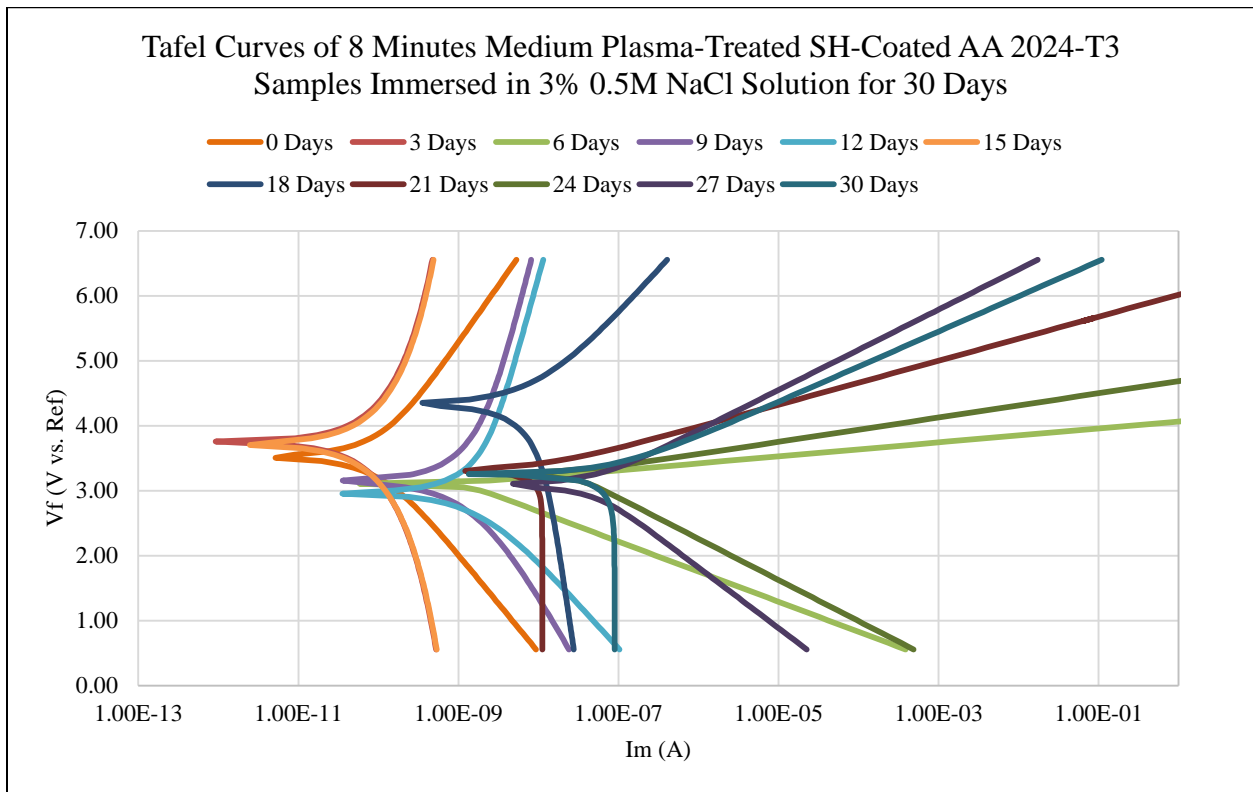


Figure 71. Tafel curves of 8 minutes medium plasma-treated SH-coated AA 2024-T3 samples immersed in 3% 0.5M NaCl solution for 30 days.

TABLE 10

CORROSION RATE PARAMETERS OF 8 MINUTES MEDIUM PLASMA-TREATED SH-COATED AA 2024-T3 SAMPLES IMMERSERD IN 3% 0.5M NACL SOLUTION FOR 30 DAYS

Immersion Days	CR (mpy)	E_{corr} (V)	I_{corr} (A)
0	8.747E-06	3.520	9.960E-11
3	6.782E-05	3.750	7.730E-10

TABLE 10 (continued)

Immersion Days	CR (mpy)	E _{corr} (V)	I _{corr} (A)
6	1.056E-04	3.110	1.200E-09
9	1.415E-04	3.140	1.610E-09
12	1.581E-04	2.960	1.800E-09
15	1.798E-04	3.720	2.050E-09
18	8.578E-04	4.340	9.770E-09
21	9.792E-04	3.320	1.120E-08
24	2.255E-03	3.270	2.570E-08
27	3.819E-03	3.090	4.350E-08
30	7.862E-03	3.260	8.950E-08

4.2.4 Corrosion Rate Behavior of Four Best Plasma-Treated SH-Coated AA 2024-T3 Samples Immersed in 3% 0.5M NaCl Solution for 30 days

The corrosion rate behavior of the 8 minutes high and medium plasma-treated, and 4 minutes high and medium plasma-treated SH-coated AA 2024-T3 samples increased with immersion time in the 3% 0.5M NaCl solution. Figure 72 shows the corrosion rate behavior concerning immersion time. According to the Table 11, the corrosion rate rises slightly in the 8 minutes medium plasma-treated SH-coated AA 2024-T3 sample compared to the 8 minutes high plasma-treated SH-coated AA 2024-T3 sample that have the same immersion period. Throughout the experiment, it was seen that the corrosion rate rarely increases with the 8 minutes high plasma-treated SH-coated AA 2024-T3 sample as the immersion time increases, but it was gradually steady in first 20 days of the experiment. Furthermore, the corrosion rate of the 8 minutes high plasma-treated SH-coated AA 2024-T3 sample after immersion in the 3% 0.5M

NaCl solution did not rise as much as the corrosion rate of the 8 minutes medium plasma-treated SH-coated AA 2024-T3 sample, which directs that the corrosion resistivity of the 8 minutes high plasma-treated SH-coated AA 2024-T3 sample is better than the corrosion resistivity of the 8 minutes medium plasma-treated SH-coated AA 2024-T3 sample, accordingly amassed the lifetime of the samples.

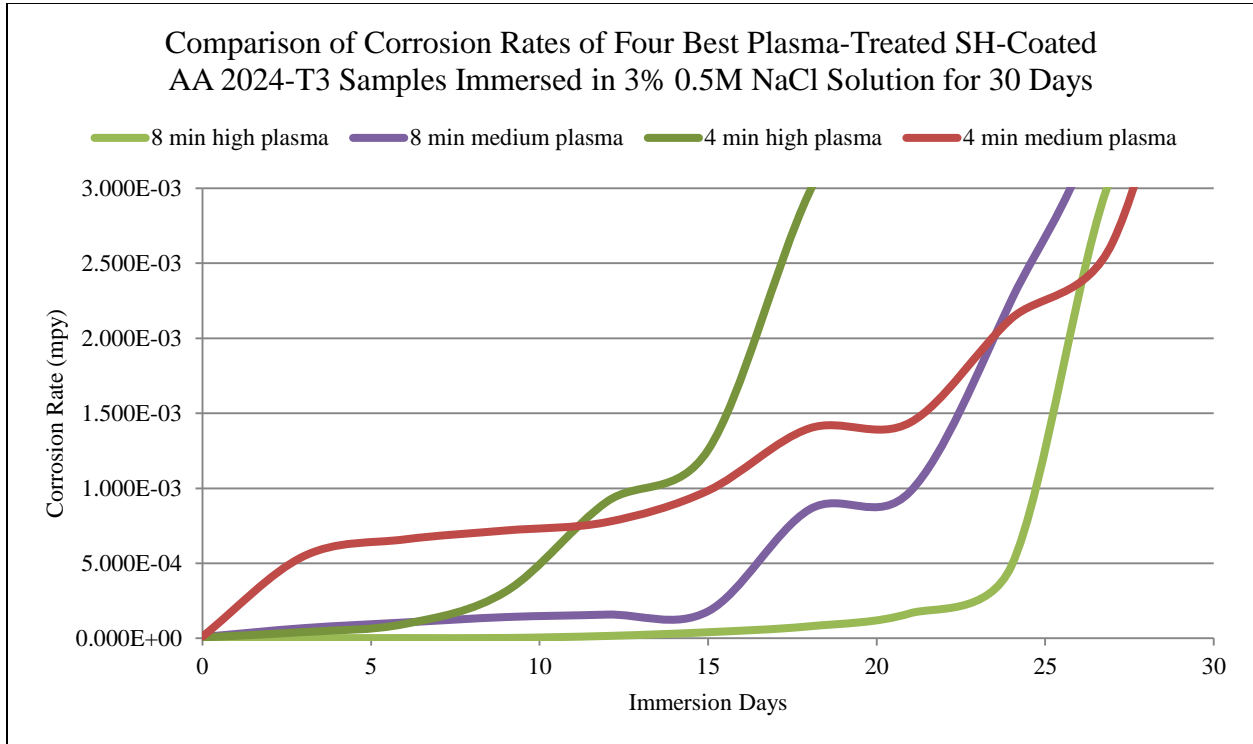


Figure 72. Comparison of corrosion rates of four best plasma-treated SH-coated AA 2024-T3 samples immersed in 3% 0.5M NaCl solution for 30 days.

TABLE 11

CORROSION RATES OF FOUR BEST PLASMA-TREATED SH-COATED AA 2024-T3 SAMPLES IMMERSSED IN 3% 0.5M NACL SOLUTION FOR 30 DAYS

Immersion Days	8 min High Plasma	8 min Medium Plasma	4 min High Plasma	4 min Medium Plasma
0	4.492E-07	8.747E-06	6.122E-06	1.213E-05
3	9.336E-07	6.782E-05	4.166E-05	5.470E-04

TABLE 11 (continued)

Immersion Days	8 min High Plasma	8 min Medium Plasma	4 min High Plasma	4 min Medium Plasma
6	1.711E-06	1.056E-04	9.569E-05	6.593E-04
9	2.449E-06	1.415E-04	3.121E-04	7.188E-04
12	1.578E-05	1.581E-04	9.111E-04	7.749E-04
15	4.050E-05	1.798E-04	1.255E-03	9.845E-04
18	7.979E-05	8.578E-04	2.970E-03	1.399E-03
21	1.672E-04	9.792E-04	4.124E-03	1.439E-03
24	4.827E-04	2.255E-03	4.722E-03	2.132E-03
27	3.103E-03	3.819E-03	5.860E-03	2.638E-03
30	3.774E-03	7.862E-03	8.647E-03	4.969E-03

4.2.5 PC Results of 8 Minutes High RF Level Plasma-Treated SH-Coated AA 2024-T3 Samples Immersed in DI Water for 30 Days

PC results after the plasma-treated SH-coated AA 2024-T3 sample immersed in DI water for 30 days clearly demonstrate that the 8 minutes high plasma-treated SH-coated AA 2024-T3 sample has the greatest corrosion performance at the beginning of the immersion time, which has a maximum corrosion rate of 2.802E-07 mpy was found 0 days of immersion in the 3% 0.5M NaCl solution, and 2.409E-04 mpy was found after 30 days of immersion. As the immersion time extends to 30 days, this sample nearly remains constant with their coating performance, which shows that there is no some degree of degradation in the coating materials, when immersed in DI water for 30 days. Figure 73 shows the 8 minutes high plasma-treated SH-coated AA 2024-T3 sample’s Tafel curve for the 30 days. For different corrosion currents, there are different corrosion potentials, which are obtained from the same Tafel curves. Corrosion rates

along with E_{corr} and I_{corr} is obtained from Tafel curves are shown in Table 12 for the 8 minutes medium plasma-treated SH-coated AA 2024-T3 sample immersed in DI water for 30 days.

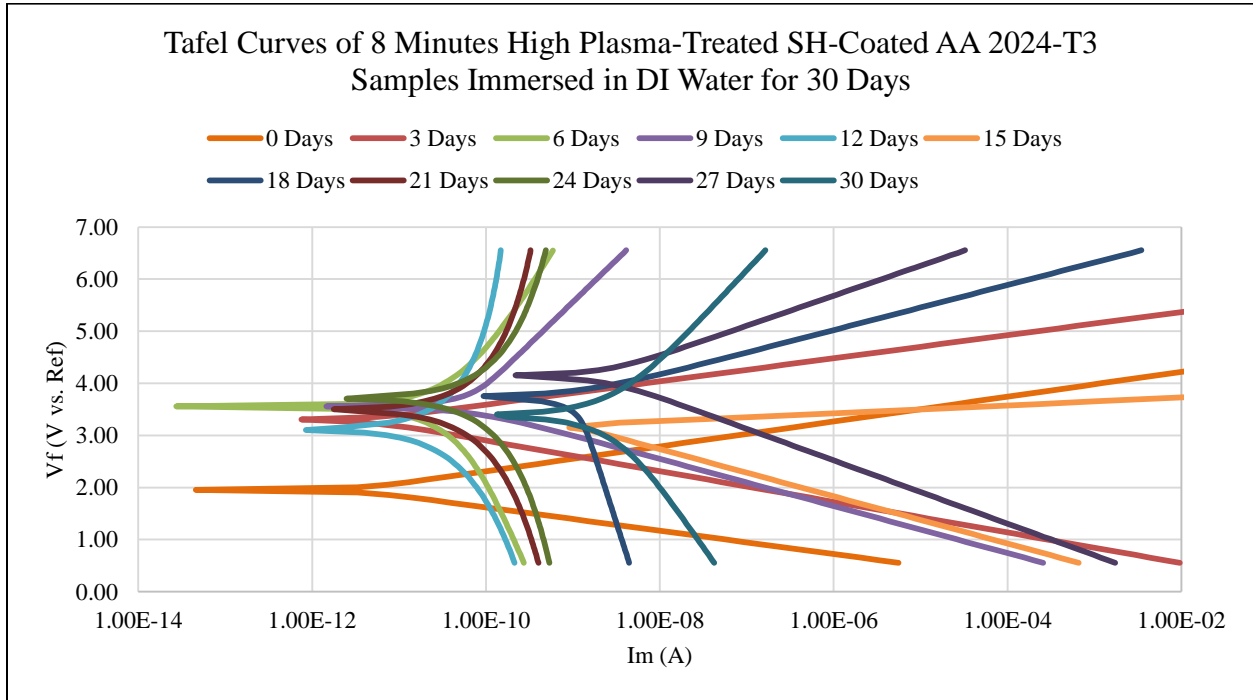


Figure 73. Tafel curves of 8 minutes high plasma-treated SH-coated AA 2024-T3 samples immersed in DI water for 30 days.

TABLE 12

CORROSION RATE PARAMETERS OF 8 MINUTES HIGH PLASMA-TREATED SH-COATED AA 2024-T3 SAMPLES IMMERSSED IN DI WATER FOR 30 DAYS

Immersion Days	CR (mpy)	E_{corr} (V)	I_{corr} (A)
0	2.802E-07	1.950	3.190E-12
3	4.023E-07	3.300	4.580E-12
6	4.246E-06	3.560	4.840E-11
9	5.097E-06	3.560	5.810E-11
12	2.436E-05	3.120	2.770E-10
15	8.579E-05	3.190	9.770E-10

TABLE 12 (continued)

Immersion Days	CR (mpy)	E_{corr} (V)	I_{corr} (A)
18	9.515E-05	3.740	1.080E-09
21	1.263E-04	3.490	1.440E-09
24	1.798E-04	3.720	2.050E-09
27	1.866E-04	4.140	2.130E-09
30	2.409E-04	3.380	2.740E-09

4.2.6 PC Results of 8 Minutes Medium RF Level Plasma-Treated SH-Coated AA 2024-T3 Samples Immersed in DI Water for 30 days

PC results after the plasma-treated SH-coated AA 2024-T3 sample immersed in DI water for 30 days clearly demonstrate that the 8 minutes medium plasma-treated SH-coated AA 2024-T3 sample has the second highest corrosion rate with respect to the immersion time, which has a maximum corrosion rate of 2.804E-06 mpy was found 0 days of immersion in the 3% 0.5M NaCl solution, and 8.919E-04 mpy was found after 30 days of immersion. As the immersion time extends to 30 days, this sample initiates to lose few of their coating properties, but not same as NaCl solution, when immersed in DI water for 30 days. Figure 74 shows the 8 minutes medium plasma-treated SH-coated AA 2024-T3 sample's Tafel curve for the 30 days. The shape of the curve is altered than the NaCl solution's Tafel curve because immersion in DI water displays a meager corrosion rate compared to NaCl solution. For different corrosion currents, there are different corrosion potentials, which are obtained from the same Tafel curves. Corrosion rates along with E_{corr} and I_{corr} is obtained from Tafel curves are shown in Table 13 for the 8 minutes medium plasma-treated SH-coated AA 2024-T3 sample immersed in DI water for 30 days.

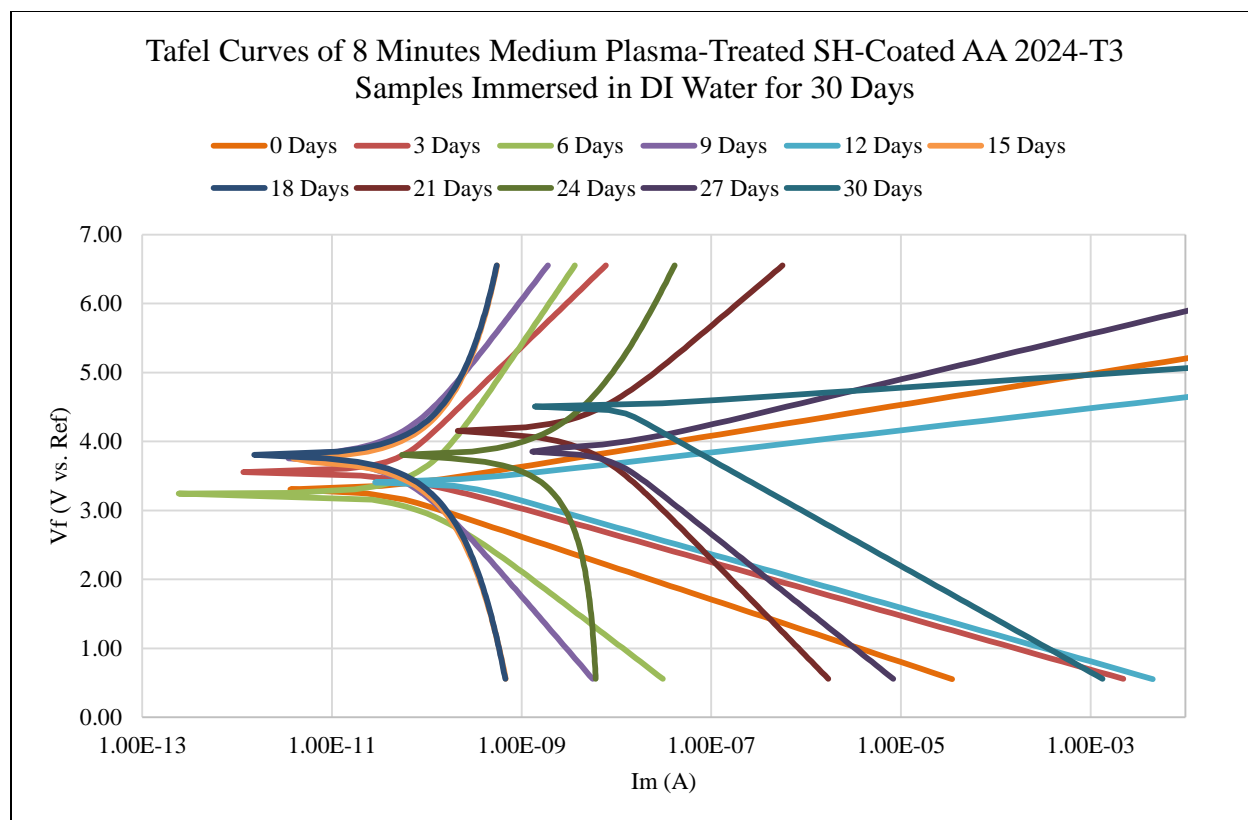


Figure 74. Tafel curves of 8 minutes medium plasma-treated SH-coated AA 2024-T3 samples immersed in DI water for 30 days.

TABLE 13

CORROSION RATE PARAMETERS OF 8 MINUTES MEDIUM PLASMA-TREATED SH-COATED AA 2024-T3 SAMPLES IMMERSSED IN DI WATER FOR 30 DAYS

Immersion Days	CR (mpy)	E_{corr} (V)	I_{corr} (A)
0	2.804E-06	3.300	3.190E-11
3	3.852E-06	3.560	4.390E-11
6	7.603E-06	3.240	8.660E-11
9	4.830E-06	3.780	5.500E-11
12	1.777E-05	3.410	2.020E-10
15	7.564E-05	3.730	8.610E-10

TABLE 13 (continued)

Immersion Days	CR (mpy)	E _{corr} (V)	I _{corr} (A)
18	2.126E-04	3.800	2.420E-09
21	4.297E-04	4.140	4.890E-09
24	5.896E-04	3.790	6.720E-09
27	6.824E-04	3.870	7.770E-09
30	8.919E-04	4.500	1.020E-08

4.2.7 Corrosion Rate Behavior of Four Best Plasma-Treated SH-Coated AA 2024-T3 Samples Immersed in DI Water for 30 days

The corrosion rate behavior of the 8 minutes high and medium plasma-treated, and 4 minutes high and medium plasma-treated SH-coated AA 2024-T3 samples increased with immersion time in the DI water. Figure 75 shows the corrosion rate behavior in detail to immersion phase in the DI water. According to the Table 14, the corrosion rate develops steadily after ten days of immersion; the corrosion rate roughly stays constant in the 8 minutes medium plasma-treated SH-coated AA 2024-T3 sample compared to the 8 minutes high plasma-treated SH-coated AA 2024-T3 sample that have the same immersion period. Throughout the experiment, it was seen that the corrosion rate remains constant with the 8 minutes high plasma-treated SH-coated AA 2024-T3 sample as the immersion time increases. This is endorsed to that the higher corrosion resistivity of the 8 minutes high plasma-treated SH-coated AA 2024-T3 sample, also with detail to immersion time in DI water. All these corrosion rates of plasma-treated SH-coated AA 2024-T3 samples immersed in DI water, are low compared to immersed in NaCl solution, which is anticipated due to the molarity of the NaCl solution.

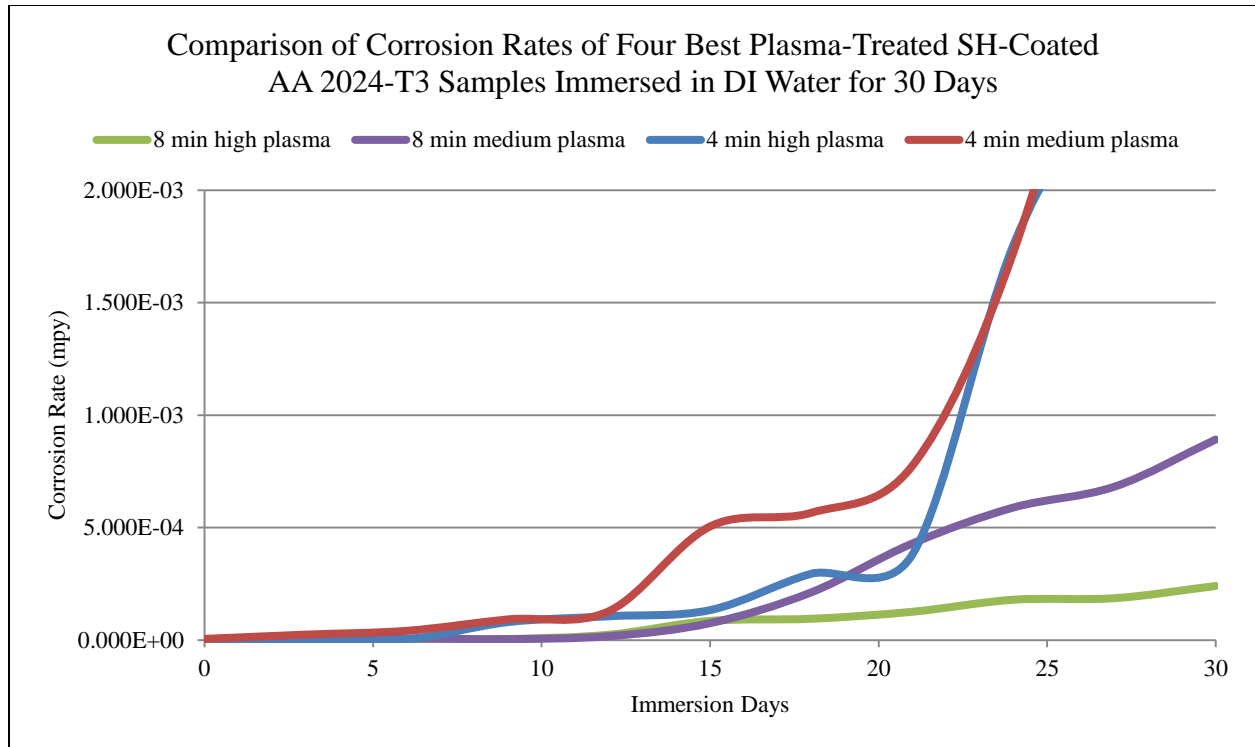


Figure 75. Comparison of corrosion rates of four best plasma-treated SH-coated AA 2024-T3 samples immersed in DI water for 30 days.

TABLE 14

CORROSION RATES OF FOUR BEST PLASMA-TREATED SH-COATED AA 2024-T3 SAMPLES IMMERSSED IN DI WATER FOR 30 DAYS

Immersion Days	8 min High Plasma	8 min Medium Plasma	4 min High Plasma	4 min Medium Plasma
0	1.043E-06	5.707E-06	2.802E-07	2.804E-06
3	5.355E-06	2.472E-05	4.023E-07	3.852E-06
6	4.421E-06	4.166E-05	4.246E-06	7.603E-06
9	8.033E-05	9.238E-05	5.097E-06	4.830E-06
12	1.062E-04	1.291E-04	2.436E-05	1.777E-05
15	1.336E-04	5.055E-04	8.579E-05	7.564E-05
18	2.952E-04	5.663E-04	9.515E-05	2.126E-04

TABLE 14 (continued)

Immersion Days	8 min High Plasma	8 min Medium Plasma	4 min High Plasma	4 min Medium Plasma
21	3.801E-04	7.749E-04	1.263E-04	4.297E-04
24	1.757E-03	1.725E-03	1.798E-04	5.896E-04
27	2.570E-03	3.337E-03	1.866E-04	6.824E-04
30	3.375E-03	5.326E-03	2.409E-04	8.919E-04

4.2.8 Comparison of PC Results of Uncoated, SH-Coated, and Plasma-Treated SH-Coated AA 2024-T3 Samples

The PC results comparison of uncoated, SH-coated, and plasma-treated SH-coated AA 2024-T3 samples are shown in Figure 76.

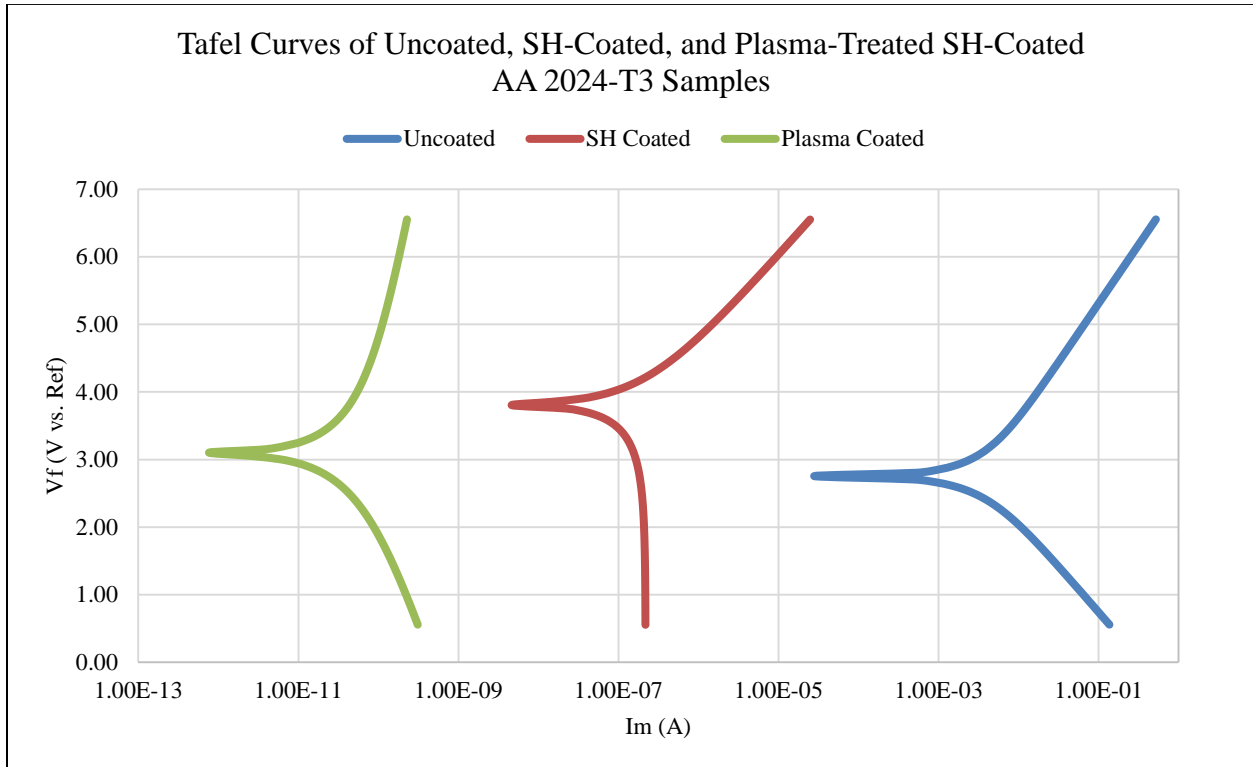


Figure 76. Tafel curves of uncoated, SH-coated, and plasma-treated SH-coated AA 2024-T3 samples.

The Table 15 shows that plasma-treated SH-coated AA 2024-T3 samples have the maximum corrosion rate results compared to SH-coated, and uncoated AA 2024-T3 samples, this is the primary outcome accepted in this study. The plasma-treated SH-coated AA 2024-T3 samples replicate the best corrosion rate result of 5.551E-06 mpy; it is nearly 0.0001 mpy lower than the formal company based SH-coated AA 2024-T3 sample, and 0.00001 mpy lower than the uncoated AA 2024-T3 sample.

TABLE 15

COMPARISON OF CORROSION RATE PARAMETERS OF UNCOATED, SH-COATED, AND PLASMA-TREATED SH-COATED AA 2024-T3 SAMPLES

Category	CR (mpy)	E _{corr} (V)	I _{corr} (A)
Uncoated	9.540E+00	2.750	3.390E-03
SH-Coated	1.916E-02	3.820	2.180E-07
Plasma-Coated	5.551E-06	3.090	6.320E-10

4.3 Electrochemical Analysis Using Electrochemical Impedance Spectroscopy

For the EIS tests, the prepared 3% 0.5M NaCl solution was used. The potential is relatively low to avoid any damage to the film surface. The impedance data were collected at the open-circuit potential on specimens held in the 3% 0.5 M NaCl solution for various periods of time. It is expected that the EIS scans of the coated specimens give higher values of polarization resistance and lower values of double layer capacitance than for the uncoated specimens given the lower dielectric properties of the organic coating materials. The EIS data were analyzed by using an electrical circuit element called Randles cell circuit, which fits the experimental impedance data received from EIS measurements to the electronic-circuit models.

4.3.1 EIS Results of Four Best Plasma-Treated SH-Coated AA 2024-T3 Samples

EIS results of the best four plasma-treated SH-coated aluminum samples, as shown in Figures 77 and 78, indicate similar styles of Nyquist and Bode plots, respectively, for different immersion time periods to attain the corrosion parameters that were assigned from the Randles cell circuit. Randles cell parameters' values obtained from the Nyquist plot and Bode plot are shown in Table 16. It is obtained that from the EIS scans of the 8 minutes high plasma-treated SH-coated AA 2024-T3 sample give higher values of polarization resistance and lower values of double layer capacitance, as expected, and the 8 minutes high plasma-treated SH-coated AA 2024-T3 sample remains second in this electrochemical analysis. This indicates that data were more reliable to explain corrosion properties.

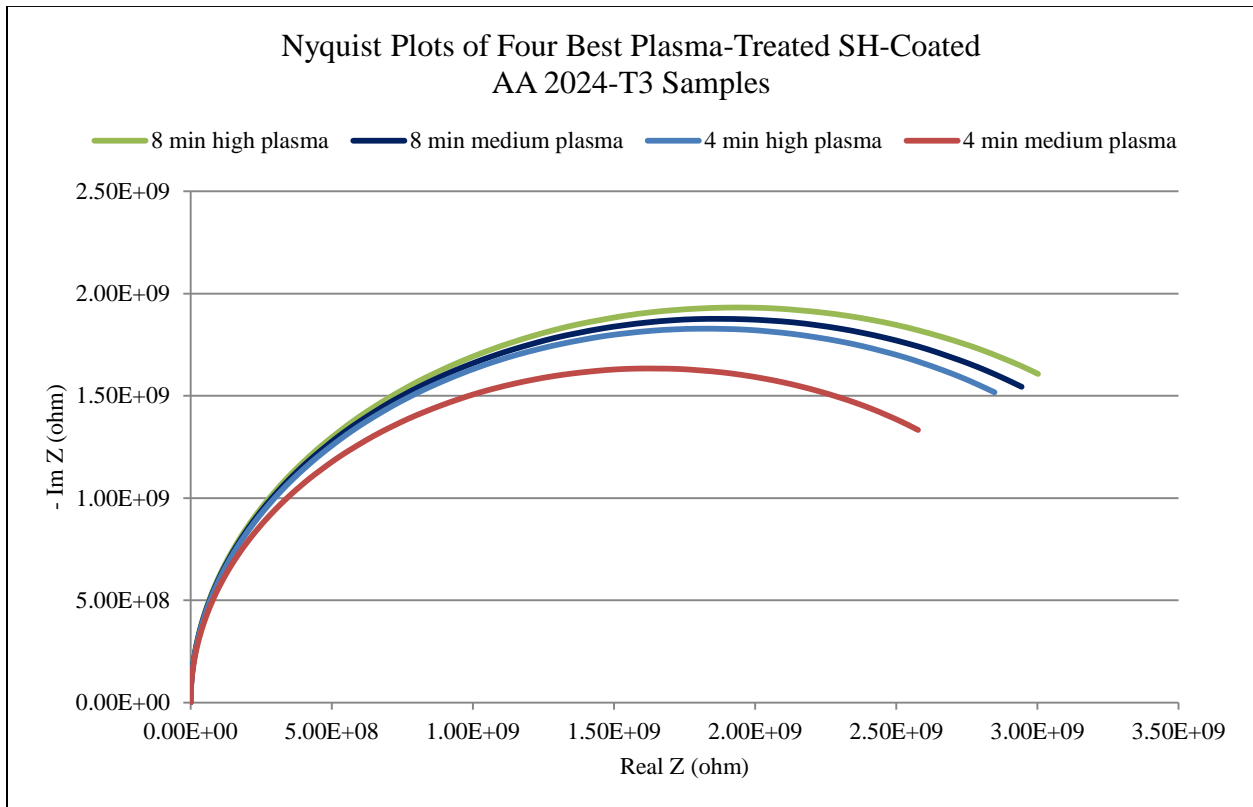


Figure 77. Nyquist plots of four best plasma-treated SH-coated AA 2024-T3 samples.

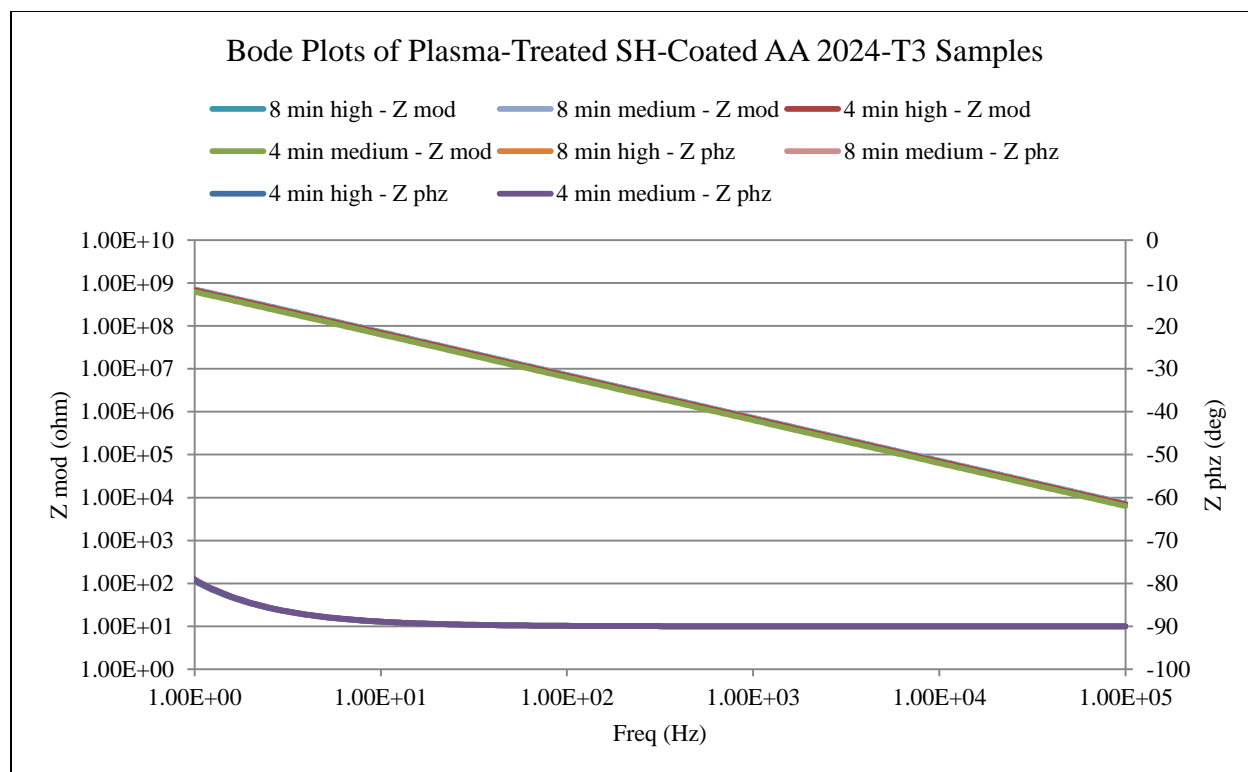


Figure 78. Bode plots of plasma-treated SH-coated AA 2024-T3 samples.

TABLE 16

RANDLES CELL PARAMETERS OF FOUR BEST PLASMA-TREATED SH-COATED AA 2024-T3 SAMPLES

Category	Rp (ohm)	Ru (ohm)	Cdl (F)
4 min High Plasma	3.66E+09	0.00E+00	2.32E-10
4 min Medium Plasma	3.27E+09	0.00E+00	2.52E-10
8 min High Plasma	3.86E+09	0.00E+00	2.21E-10
8 min Medium Plasma	3.75E+09	0.00E+00	2.22E-10

4.3.2 EIS Results of 8 Minutes High RF Level Plasma-Treated SH-Coated AA 2024-T3 Sample Immersed in 3% 0.5M NaCl Solution for 30 days

EIS results after the 8 minutes high plasma-treated SH-coated AA 2024-T3 sample immersed in 3% 0.5M NaCl solution for 30 days evidently show that the 8 minutes high plasma-

treated SH-coated AA 2024-T3 samples have the highest corrosion performance at the beginning of the immersion time as shown in Figure 79 and 80. Using the Randles cell circuit as the electric circuit element, polarization resistance, solution resistance, and double layer capacitance value obtained from the Nyquist plot and Bode plot are shown in Table 17. The dependence of imaginary impedance on frequency reveals that the 8 minutes high plasma-treated SH-coated AA 2024-T3 sample exhibits the highest values of real impedance. It is believed that the modulus of real impedance decreases as the time of immersion in the aggressive solution increases due to the loss of the protective properties of the coatings. It looks like that the polarization resistance is $7.50\text{E}+09$ ohm in 0 days as the 8 minutes high plasma-treated SH-coated AA 2024-T3 sample immersed in 3% 0.5M NaCl solution and decreased up to a value of only $1.86\text{E}+05$ ohm after 30 days, and the double layer capacitance increases with respect to immersion time in the 3% 0.5M NaCl solution.

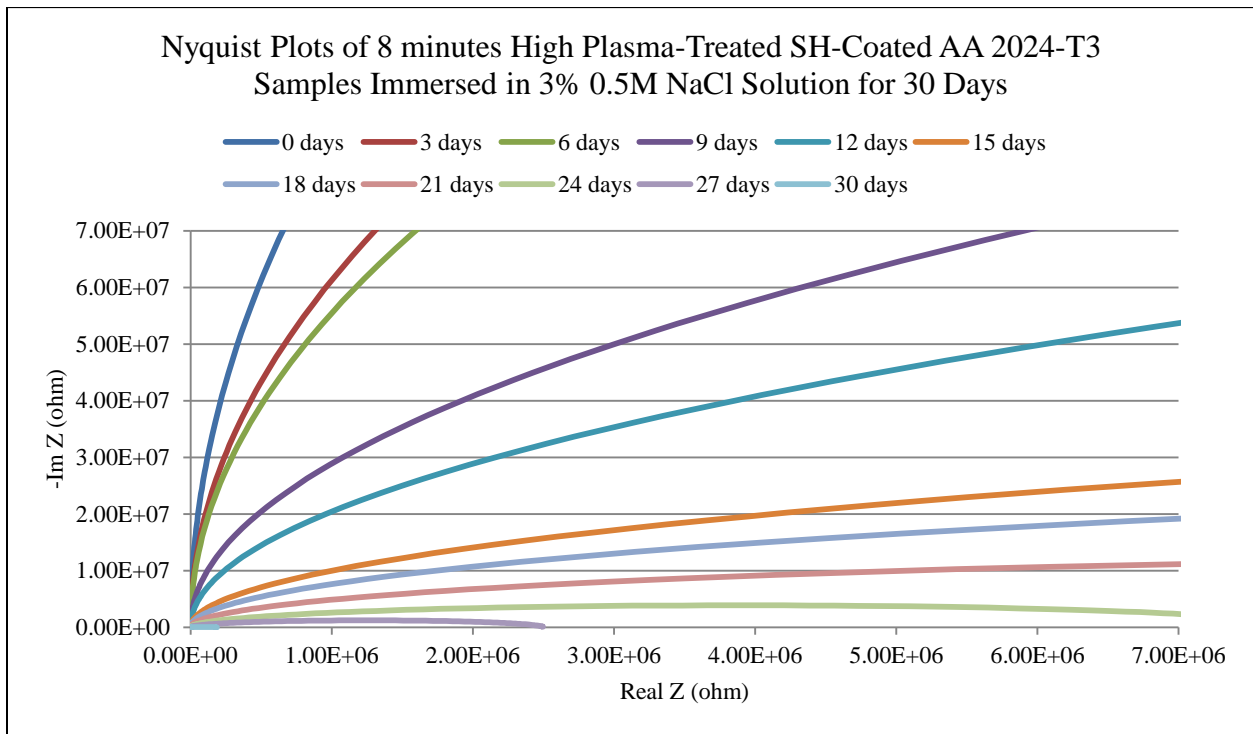


Figure 79. Nyquist plots of 8 minutes high plasma-treated SH-coated AA 2024-T3 samples immersed in 3% 0.5M NaCl solution for 30 days.

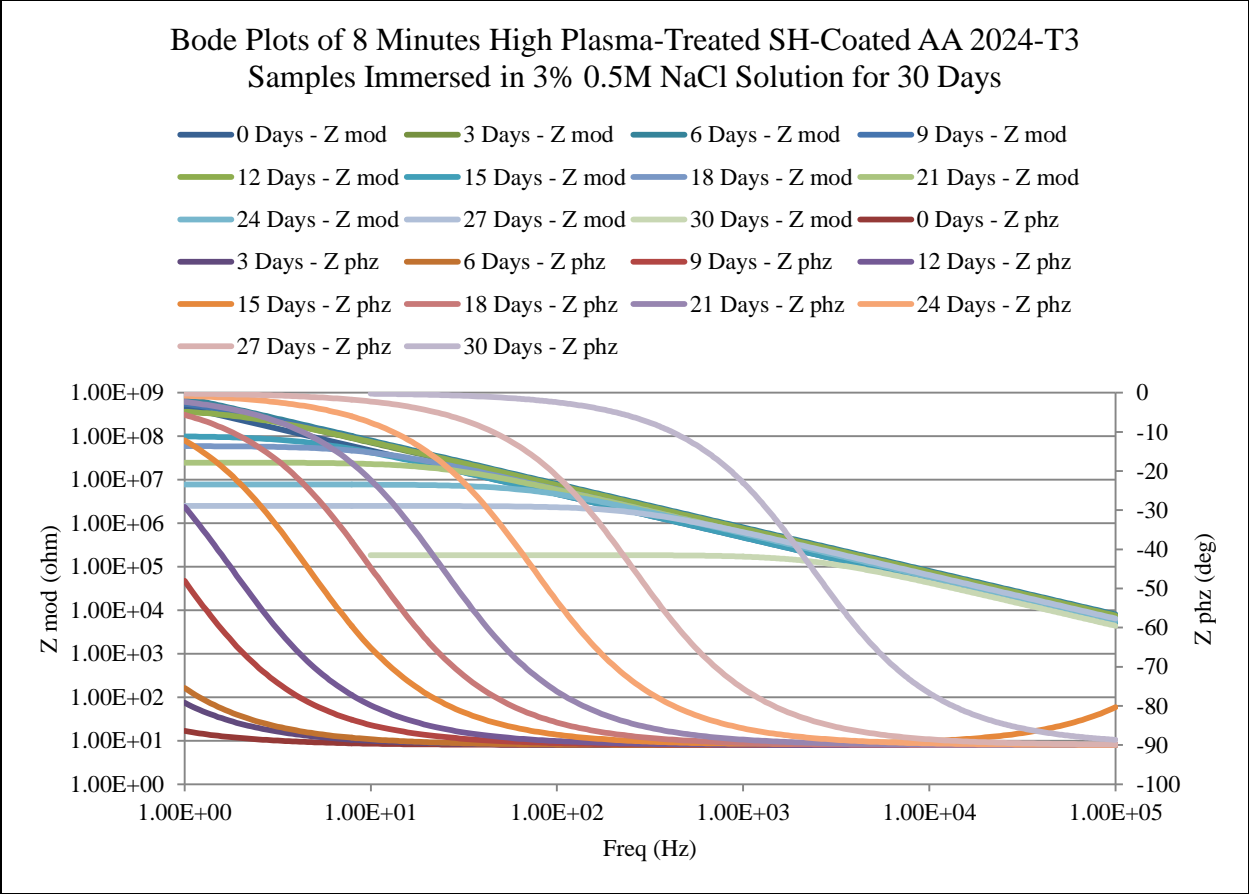


Figure 80. Bode plots of 8 minutes high plasma-treated SH-coated AA 2024-T3 samples immersed in 3% 0.5M NaCl solution for 30 days.

TABLE 17

RANGLES CELL PARAMETERS OF 8 MINUTES HIGH PLASMA-TREATED SH-COATED AA 2024-T3 SAMPLES IMMERSIED IN 3% 0.5M NACL SOLUTION FOR 30 DAYS

Immersion Days	Rp (ohm)	Rs (ohm)	Cdl (F)
0	7.50E+09	2.22E-01	3.37E-10
3	3.75E+09	0.00E+00	2.22E-10
6	3.08E+09	0.00E+00	1.98E-10
9	8.36E+08	7.36E-01	2.12E-10
12	4.19E+08	1.31E-01	2.12E-10

TABLE 17 (continued)

Immersion Days	Rp (ohm)	Rs (ohm)	Cdl (F)
15	1.01E+08	8.00E+00	3.39E-10
18	5.96E+07	2.12E-02	2.64E-10
21	2.49E+07	1.58E-01	2.62E-10
24	7.81E+06	8.27E-01	2.73E-10
27	2.50E+06	4.15E-01	2.48E-10
30	1.86E+05	6.44E-03	3.63E-10

4.3.3 EIS Results of 8 Minutes Medium RF Level Plasma-Treated SH-Coated AA 2024-T3 Sample Immersed in 3% 0.5M NaCl Solution for 30 days

EIS results of the 8 minutes medium plasma-treated SH-coated AA 2024-T3 sample immersed in 3% 0.5M NaCl solution for 30 days show this sample has the second highest corrosion performance at the beginning of the immersion time after the 8 minutes high plasma-treated SH-coated AA 2024-T3 sample. Using the Randles cell circuit as the electric circuit element, polarization resistance, solution resistance, and double layer capacitance value obtained from the Nyquist plot and Bode plot are shown in Table 18 for the 8 minutes medium plasma-treated SH-coated AA 2024-T3 sample. Figure 80 and 81 show the Nyquist plot and Bode plot for the 8 minutes medium plasma-treated SH-coated AA 2024-T3 sample immersed in 3% 0.5 M NaCl solution for 30 days respectively.

TABLE 18

RANGLES CELL PARAMETERS OF 8 MINUTES MEDIUM PLASMA-TREATED SH-COATED AA 2024-T3 SAMPLES IMMERSSED IN 3% 0.5M NAACL SOLUTION FOR 30 DAYS

Immersion Days	Rp (ohm)	Rs (ohm)	Cdl (F)
0	3.86E+09	0.00E+00	2.21E-10
3	3.75E+09	0.00E+00	2.22E-10
6	3.08E+09	0.00E+00	1.98E-10
9	1.59E+09	2.80E+00	2.39E-10
12	1.06E+09	1.96E+00	2.39E-10
15	9.61E+08	2.97E-01	2.12E-10
18	5.24E+08	8.27E+00	2.39E-10
21	3.36E+07	0.00E+00	2.52E-10
24	7.35E+06	3.22E-01	2.05E-10
27	7.44E+05	6.72E-02	1.43E-10
30	1.55E+05	6.93E-03	3.62E-10

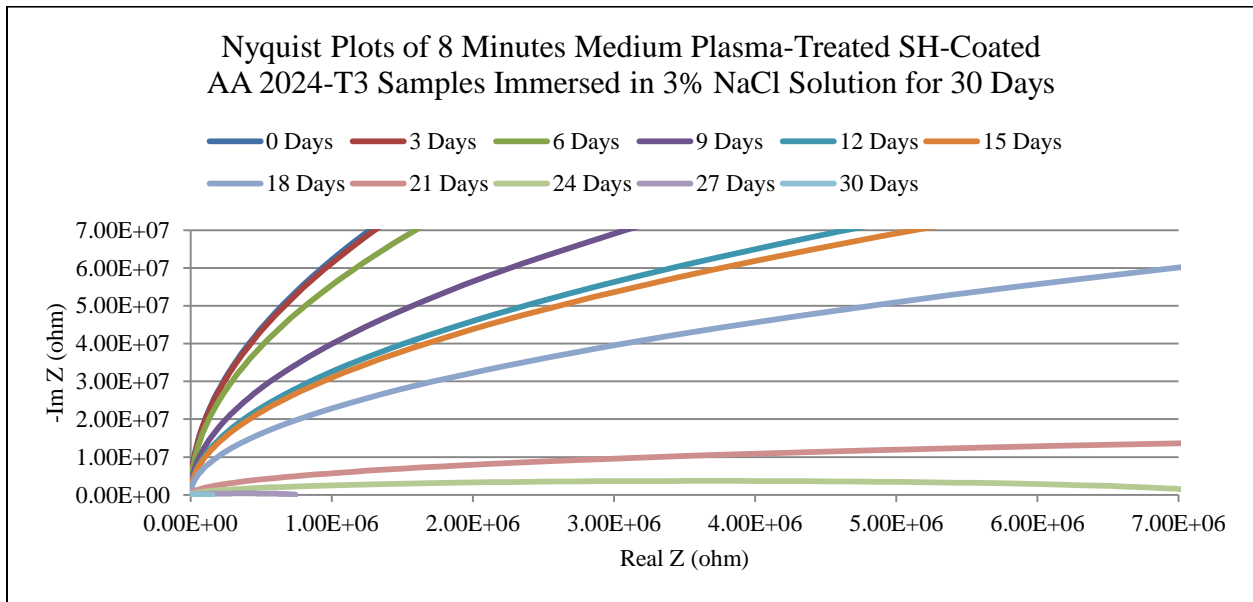


Figure 81. Nyquist plots of 8 minutes medium plasma-treated SH-coated AA 2024-T3 samples immersed in 3% 0.5M NaCl solution for 30 days.

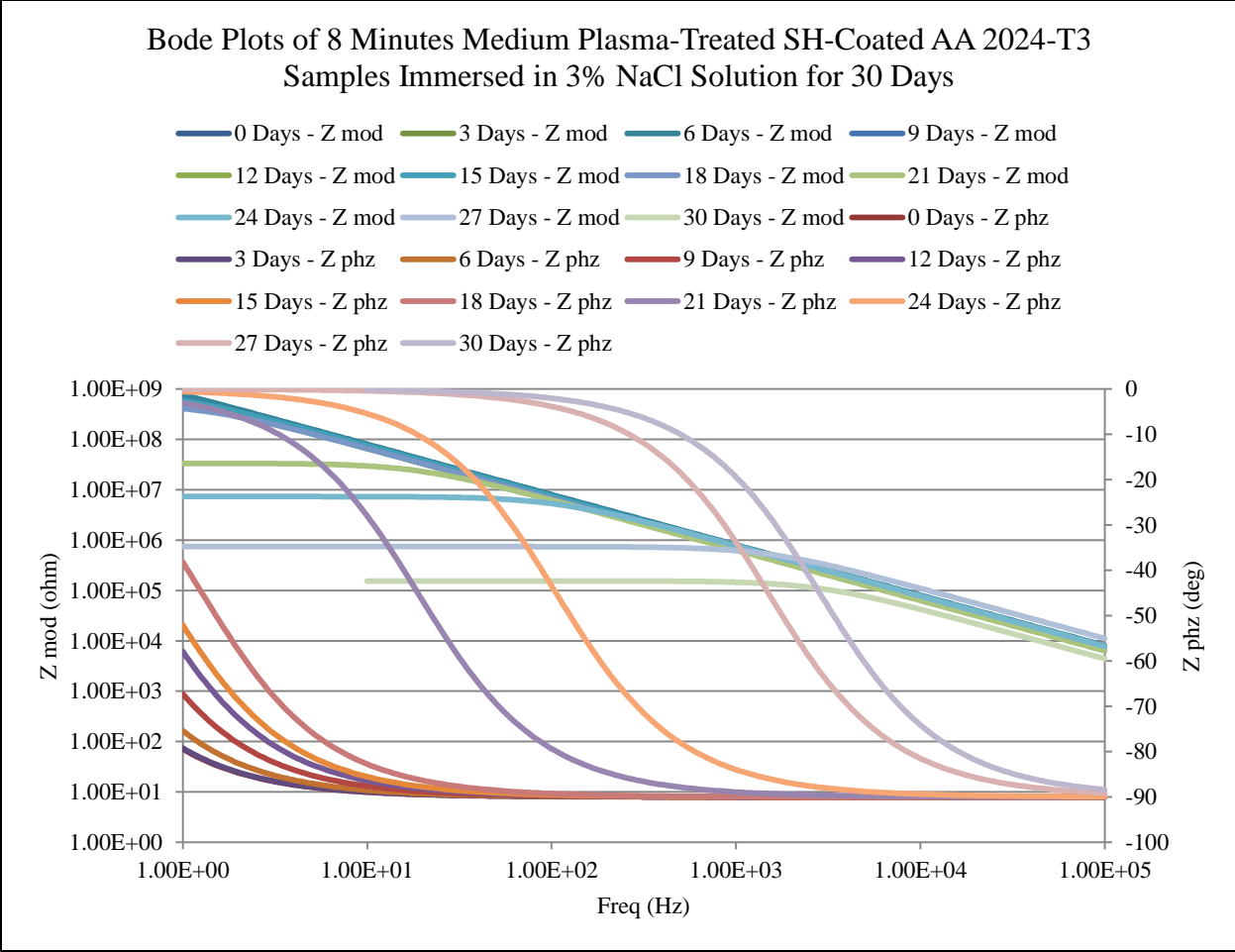


Figure 82. Bode plots of 8 minutes medium plasma-treated SH-coated AA 2024-T3 samples immersed in 3% 0.5M NaCl solution for 30 days.

4.3.4 EIS Results of 8 Minutes High RF Level Plasma-Treated SH-Coated AA 2024-T3 Sample Immersed in DI Water for 30 days

EIS results after the 8 minutes high plasma-treated SH-coated AA 2024-T3 sample immersed in DI water for 30 days evidently show that the 8 minutes high plasma-treated SH-coated AA 2024-T3 samples have the highest corrosion performance at the beginning of the immersion time. It seems that the polarization resistance is $7.50E+09$ ohm in 0 days as the 8 minutes high plasma-treated SH-coated AA 2024-T3 sample immersed in DI water and decreases up to a value of only $5.96E+07$ ohm after 30 days, and the double layer capacitance increases concerning immersion time in the DI water. Figure 83 and 84 show the Nyquist plot

and Bode plot for the 8 minutes high plasma-treated SH-coated AA 2024-T3 sample immersed in DI water for 30 days respectively. Using the Randles cell circuit as the electric circuit element, polarization resistance, solution resistance, and double layer capacitance value obtained from the Nyquist plot and Bode plot are shown in Table 19.

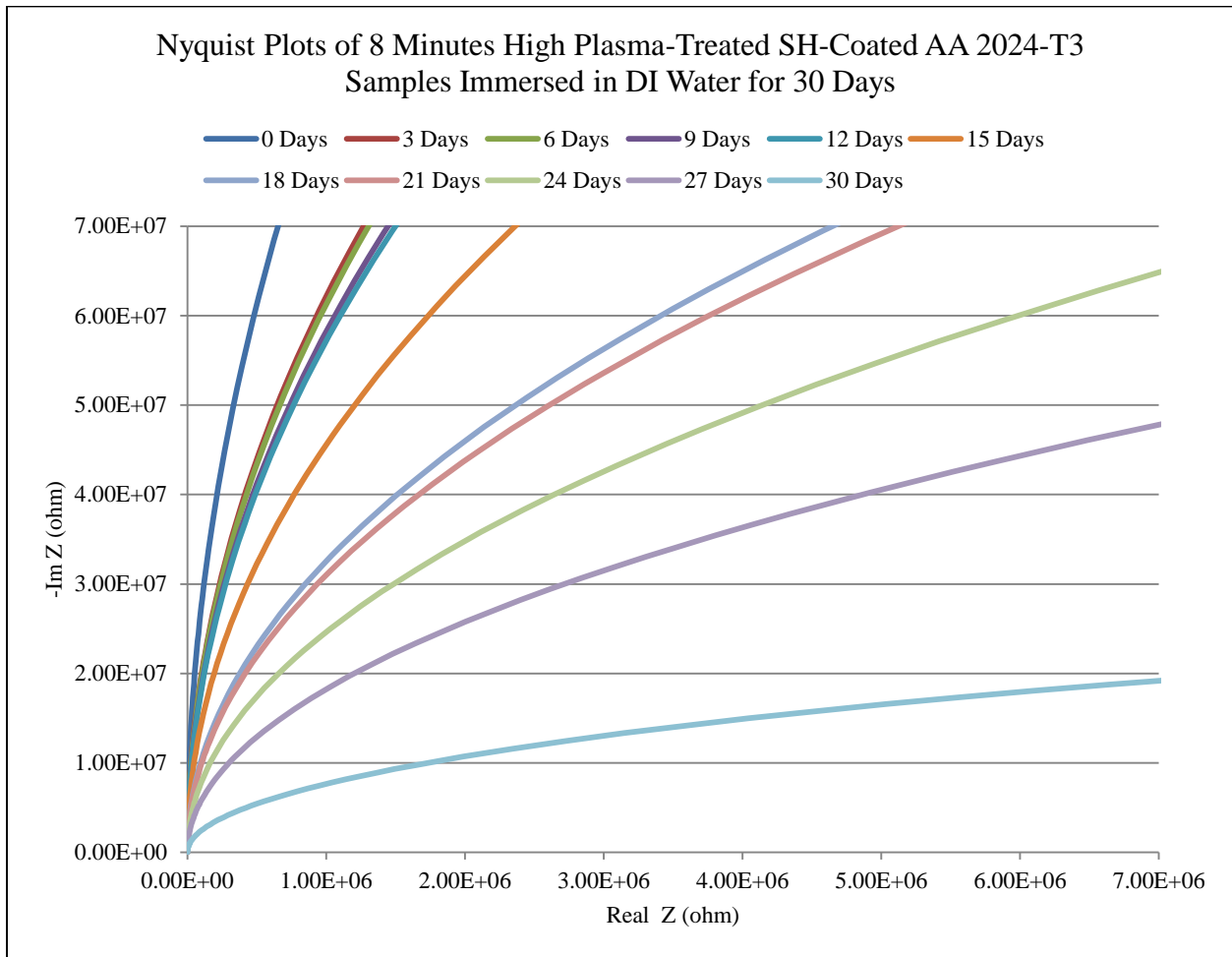


Figure 83. Nyquist plots of 8 minutes high plasma-treated SH-coated AA 2024-T3 samples immersed in DI water for 30 days.

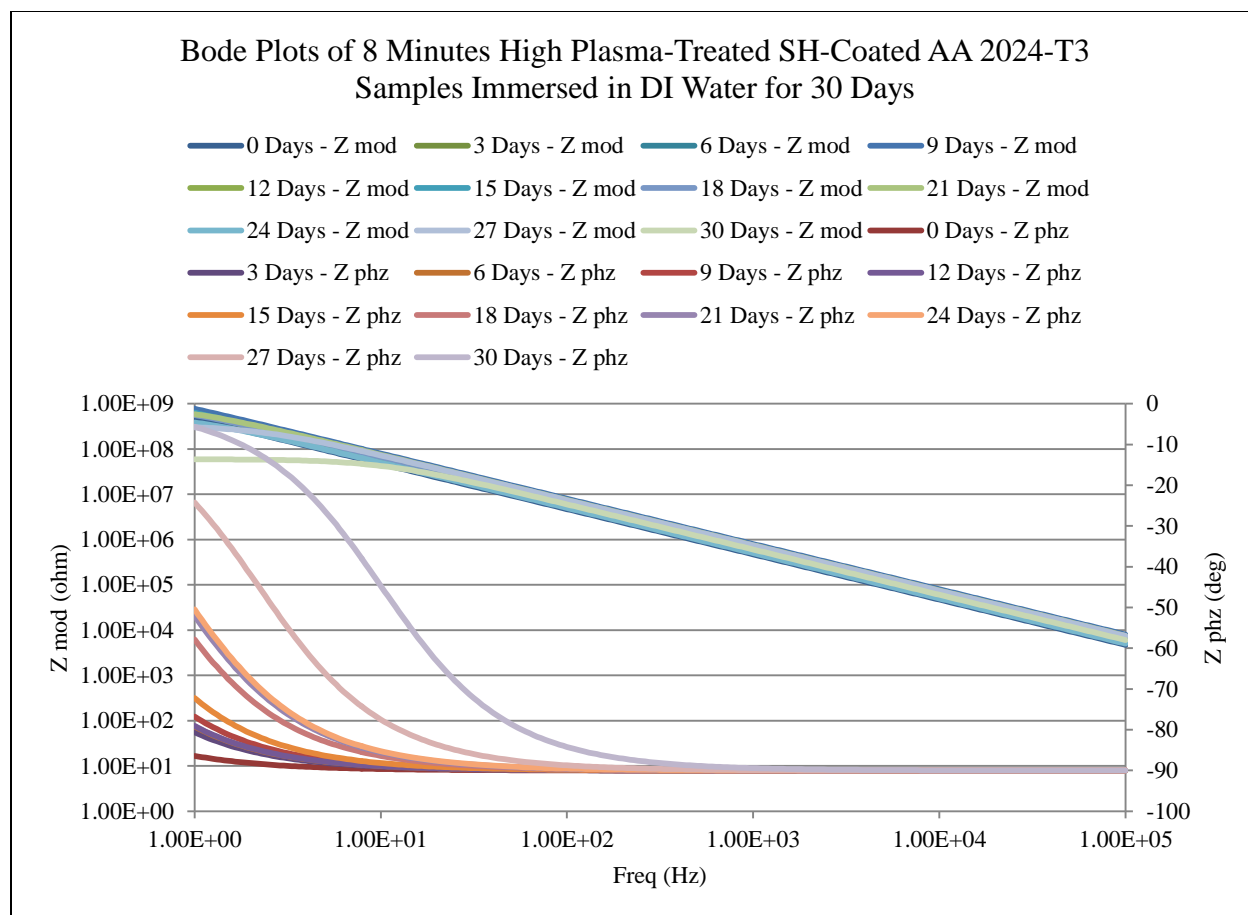


Figure 84. Bode plots of 8 minutes high plasma-treated SH-coated AA 2024-T3 samples immersed in DI water for 30 days.

TABLE 19

RANGLES CELL PARAMETERS OF 8 MINUTES HIGH PLASMA-TREATED SH-COATED AA 2024-T3 SAMPLES IMMERSSED IN DI WATER FOR 30 DAYS

Immersion Days	R_p (ohm)	R_s (ohm)	Cdl (F)
0	$7.50E+09$	$2.22E-01$	$3.37E-10$
3	$3.86E+09$	$0.00E+00$	$2.49E-10$
6	$3.75E+09$	$0.00E+00$	$2.22E-10$
9	$3.39E+09$	$0.00E+00$	$1.99E-10$
12	$3.27E+09$	$0.00E+00$	$2.52E-10$

TABLE 19 (continued)

Immersion Days	Rp (ohm)	Rs (ohm)	Cdl (F)
15	2.08E+09	1.79E+00	2.39E-10
18	1.06E+09	1.96E+00	2.39E-10
21	9.61E+08	2.97E-01	2.12E-10
24	6.08E+08	0.00E+00	3.18E-10
27	3.34E+08	3.86E-01	2.15E-10
30	5.96E+07	2.12E-02	2.64E-10

4.3.5 EIS Results of 8 Minutes Medium RF Level Plasma-Treated SH-Coated AA 2024-T3 Sample Immersed in DI Water for 30 days

EIS results of the 8 minutes medium plasma-treated SH-coated AA 2024-T3 sample immersed in DI water for 30 days show this sample has the second highest corrosion parameters at the beginning of the immersion time after the 8 minutes high plasma-treated SH-coated AA 2024-T3 sample. According to Table 20, there is no much significant difference between the 8 minutes high and medium plasma-treated SH-coated AA 2024-T3 samples immersed in DI water for 30 days. Figure 85 and 86 show the Nyquist plot and Bode plot for the 8 minutes medium plasma-treated SH-coated AA 2024-T3 sample immersed in DI water for 30 days respectively. It appears that the polarization resistance is 3.86E+09 ohm in 0 days as the 8 minutes medium plasma-treated SH-coated AA 2024-T3 sample immersed in DI water and decreased up to a value of only 7.96E+06 ohm after 30 days, and the double layer capacitance also increases by the immersion time increases in the DI water.

TABLE 20

RANGLES CELL PARAMETERS OF 8 MINUTES MEDIUM PLASMA-TREATED SH-COATED AA 2024-T3 SAMPLES IMMERSSED IN DI WATER FOR 30 DAYS

Immersion Days	Rp (ohm)	Rs (ohm)	Cdl (F)
0	3.86E+09	0.00E+00	2.21E-10
3	3.86E+09	0.00E+00	2.49E-10
6	2.41E+09	4.24E+00	2.39E-10
9	1.59E+09	2.80E+00	2.39E-10
12	8.36E+08	7.36E-01	2.12E-10
15	4.19E+08	1.31E-01	2.12E-10
18	3.34E+08	3.86E-01	2.15E-10
21	6.26E+07	1.55E-02	2.65E-10
24	5.96E+07	2.12E-02	2.64E-10
27	4.47E+07	0.00E+00	2.35E-10
30	7.96E+06	3.10E-01	2.07E-10

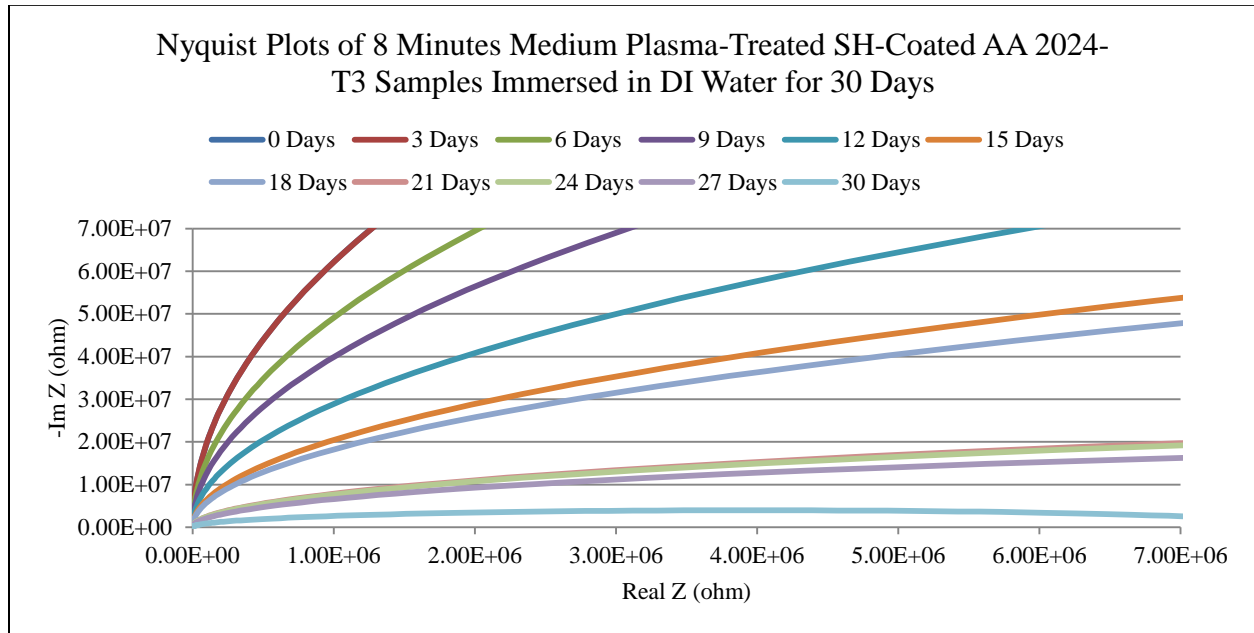


Figure 85. Nyquist plots of 8 minutes medium plasma-treated SH-coated AA 2024-T3 samples immersed in DI water for 30 days.

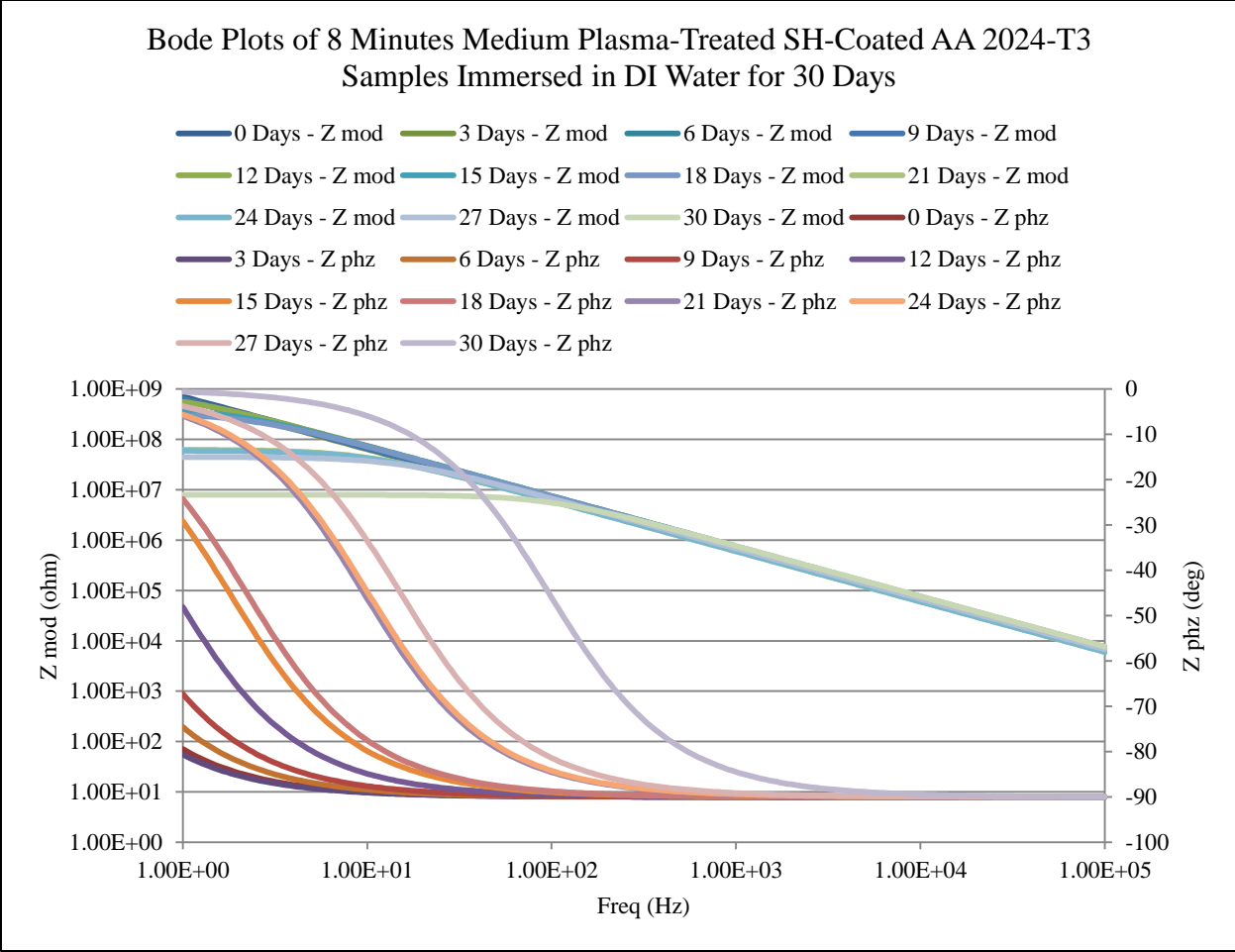


Figure 86. Bode plots of 8 minutes medium plasma-treated SH-coated AA 2024-T3 samples immersed in DI water for 30 days.

4.3.6 Comparison of EIS Results of Uncoated, SH-Coated, and Plasma-Treated SH-Coated AA 2024-T3 Samples

The Table 21 shows that plasma-treated SH-coated AA 2024-T3 samples have the maximum polarization resistance results compared to SH-coated, and uncoated AA 2024-T3 samples, this indicates the plasma-treated SH-coated AA 2024-T3 sample can withstand a long time compared to SH-coated, and uncoated AA 2024-T3 samples. The EIS results comparison of uncoated, SH-coated, and plasma-treated SH-coated AA 2024-T3 samples are shown in Figure 87 and 88. Figure 87 shows a comparison of uncoated, SH-coated, and plasma-treated SH-coated AA 2024-T3 samples in Nyquist plot, and Figure 88 shows a comparison of uncoated, SH-

coated, and plasma-treated SH-coated AA 2024-T3 samples in Bode plot. The plasma-treated SH-coated AA 2024-T3 sample produces the best polarization resistance result of $3.753\text{E}+09$ ohms; it is nearly 10000 ohm higher than the formal company based SH-coated AA 2024-T3 sample.

TABLE 21

COMPARISON OF RANDES CELL PARAMETERS OF UNCOATED, SH-COATED, AND PLASMA-TREATED SH-COATED AA 2024-T3 SAMPLES

Category	Rp (ohm)	Rs (ohm)	Cdl (F)
Uncoated	1.251E+01	1.706E-05	1.752E-07
SH Coated	1.950E+05	1.144E-01	1.523E-10
Plasma Coated	3.753E+09	0.000E+00	2.224E-10

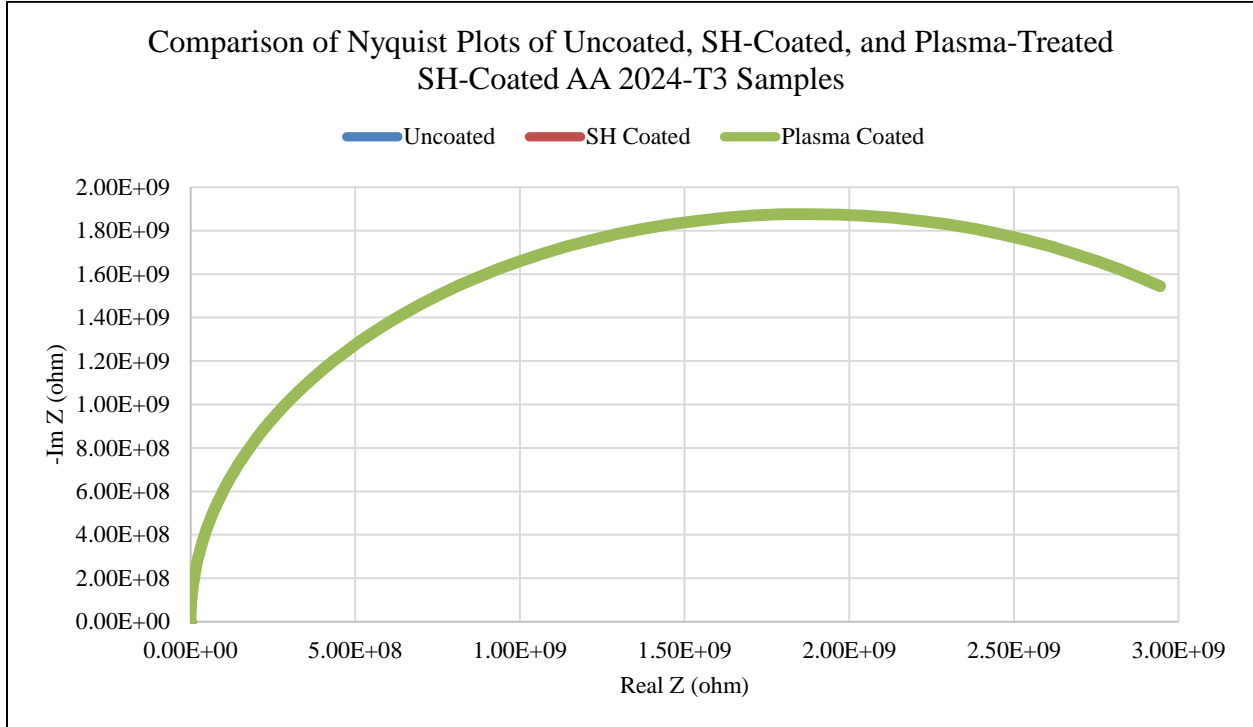


Figure 87. Comparison of Nyquist plots of uncoated, SH-coated, and plasma-treated SH-coated AA 2024-T3 samples.

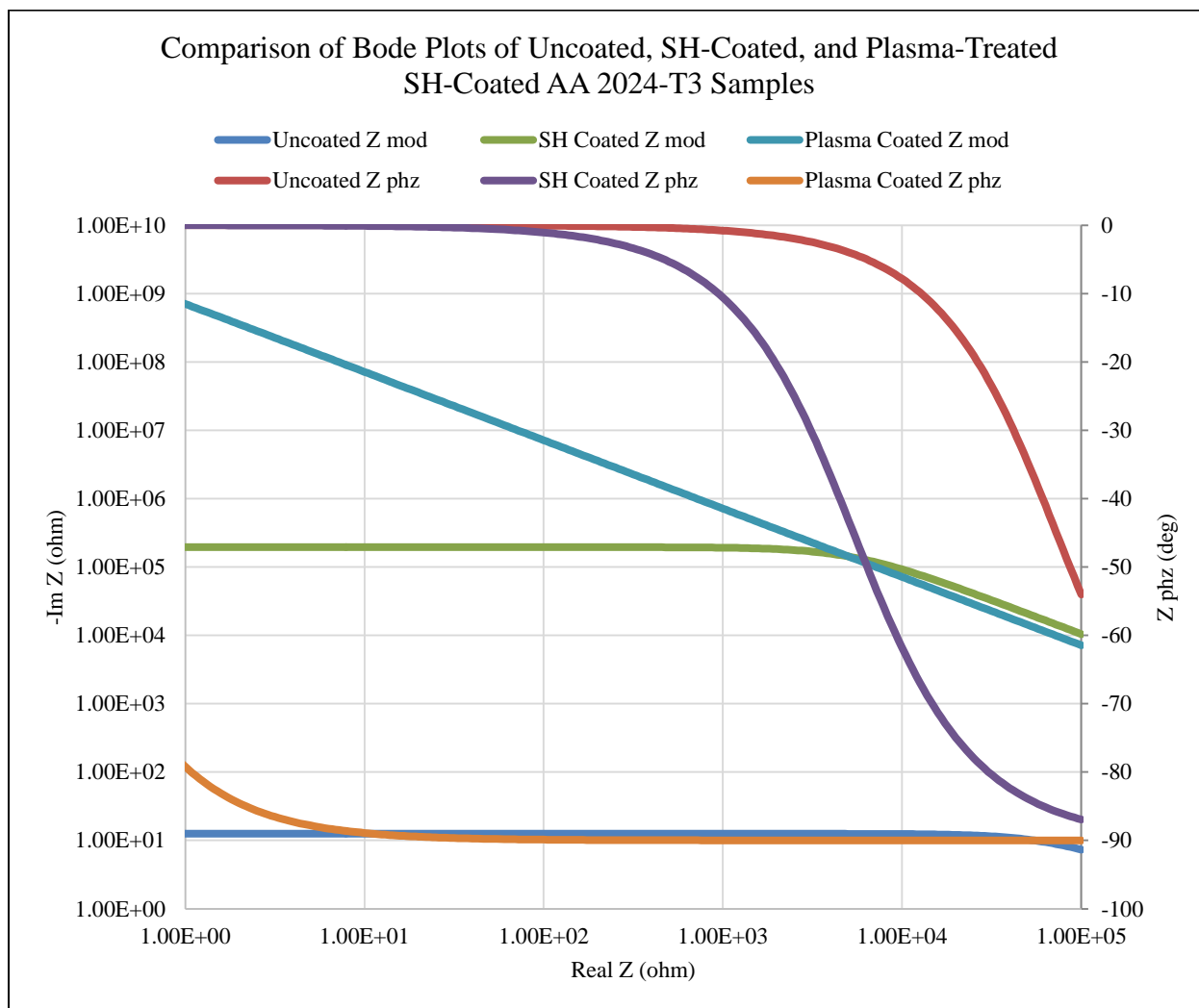


Figure 88. Comparison of Bode plots of uncoated, SH-coated, and plasma-treated SH-coated AA 2024-T3 samples.

4.4 FTIR Spectra Analysis of Plasma-Treated and SH-Coated AA 2024-T3 Samples

FTIR spectra analysis of plasma-treated SH-coated AA 2024-T3 samples is shown in Figures 89 and 90. Figure 89 shows FTIR spectra analysis of the samples for 0 days, that is, the initial day without immersion in the 3% 0.5M NaCl solution. Figure 90 shows the FTIR spectra analysis of the samples after 30-days immersion in the 3% 0.5M NaCl solution.

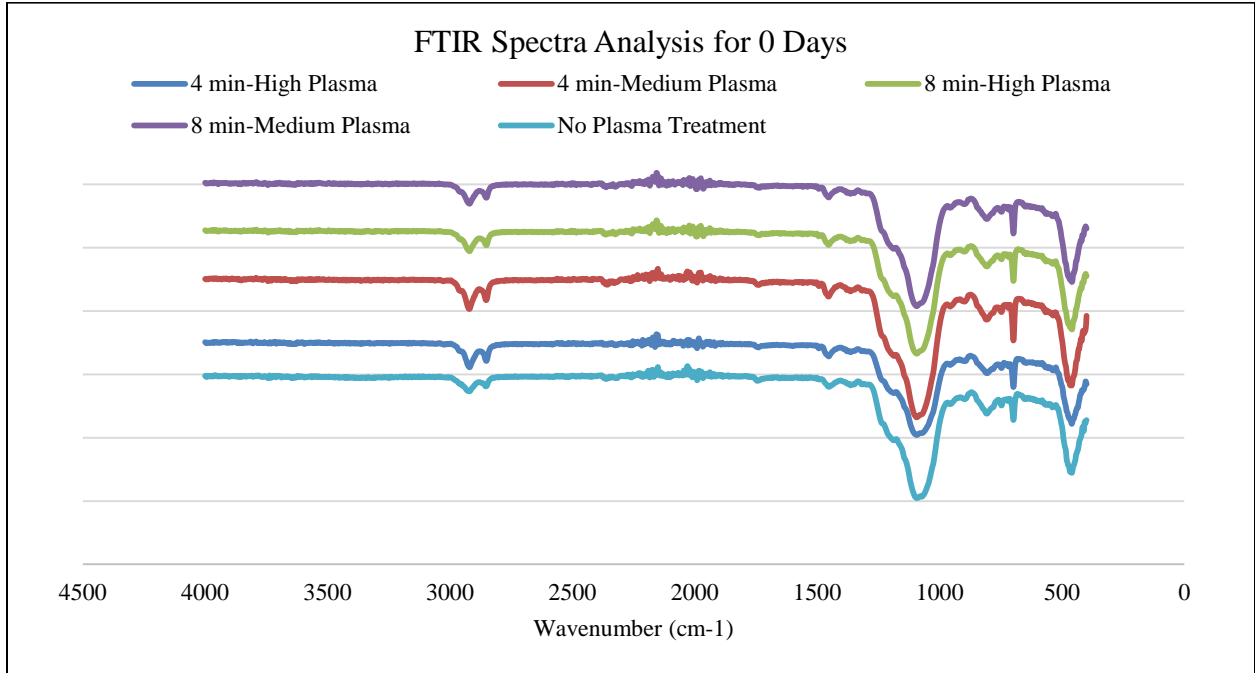


Figure 89. FTIR spectra analysis of the plasma-treated SH-coated AA 2024-T3 samples, and only SH-coated sample for 0 days.

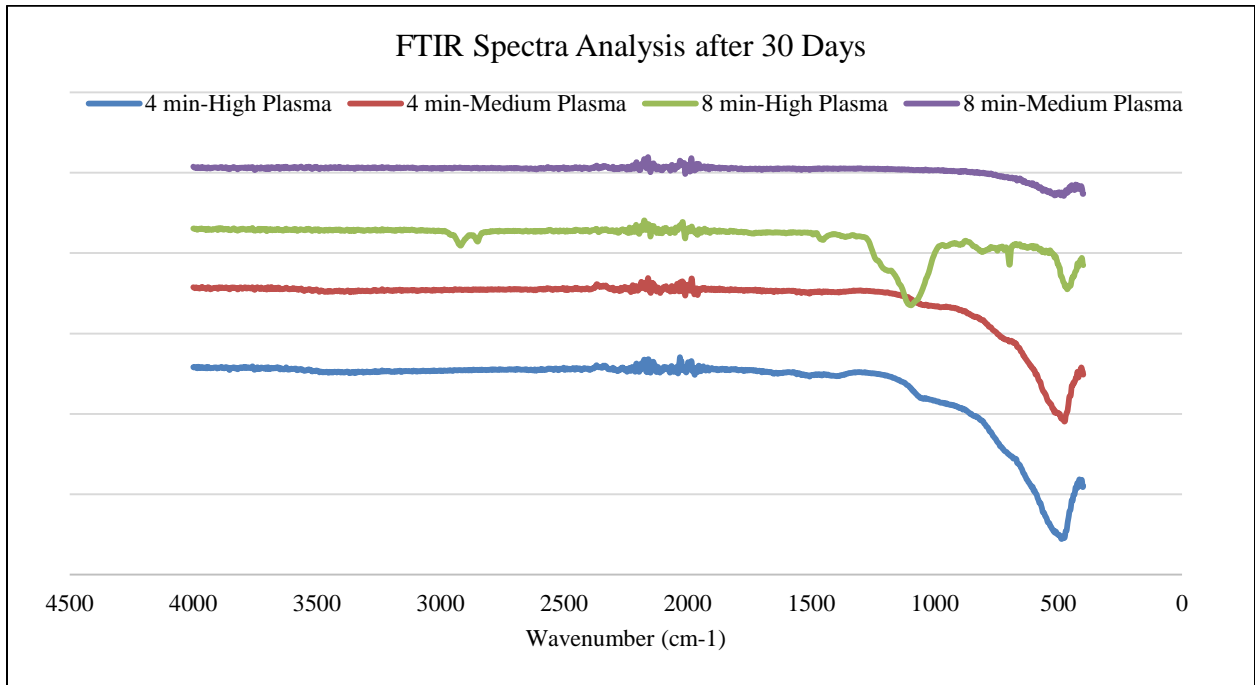


Figure 90. FTIR spectra analysis of plasma-treated SH-coated AA 2024-T3 samples after 30 days.

FTIR spectra analysis suggested that the 8 minutes high plasma-treated SH-coated AA 2024-T3 sample gave the best results for prevention from corrosion effects of 3% 0.5M NaCl solution. When initially at 0 days' results are compared to 30 days' results after the samples were immersed in 3% 0.5M NaCl solution, it can clearly be seen that most of the functional groups were vanished after 30 days of immersing in 3% 0.5M NaCl solution. However, the 8 minutes high plasma-treated SH-coated AA 2024-T3 sample was seen to keep more of the functional groups at the end of 30 days. This suggests that longer the plasma treatment at higher RF level provided stronger bonds between the substrate and the top coating. Due to these obtained results, this sample was thought to be a better candidate for further applications.

4.5 Vickers Micro Hardness Number Measurement of Plasma-Treated SH-Coated AA 2024-T3 Samples

Vickers Micro Hardness test was achieved to check whether the plasma-treated SH-coated AA 2024 – T3 samples are mechanically stable. The technique, plasma surface cleaning treatment is not changing the plasma-treated SH-coated AA 2024 – T3 samples' mechanical properties. In this experiment, the Vickers microhardness number of the 8 minutes high, and medium plasma-treated SH-coated AA 2024 – T3 samples were obtained and compared that with uncoated AA 2024-T3 sample. Vickers microhardness number obtained five times, average and standard deviations were evaluated as shown in Table 22. There is a slight deviation between the Vickers microhardness number values. Figure 91 shows the bar chart shows that the plasma-treated SH-coated AA 2024 – T3 samples' mechanical properties are not changing due to plasma surface cleaning treatment.

TABLE 22

VICKERS MICROHARDNESS TEST RESULTS OF UNCOATED AND PLASMA-TREATED SH-COATED AA 2024-T3 SAMPLES

Plasma-Treated SH-Coated Aluminum	1st Reading	2nd Reading	3rd Reading	4th Reading	5th Reading	Average
8 min High Plasma	143.2	145.2	138.2	139.5	142.3	141.7
8 min Medium Plasma	142.5	139.4	138.4	141.2	134.3	139.2
Uncoated Aluminum	139.4	142.3	136.5	137.2	135.2	138.1

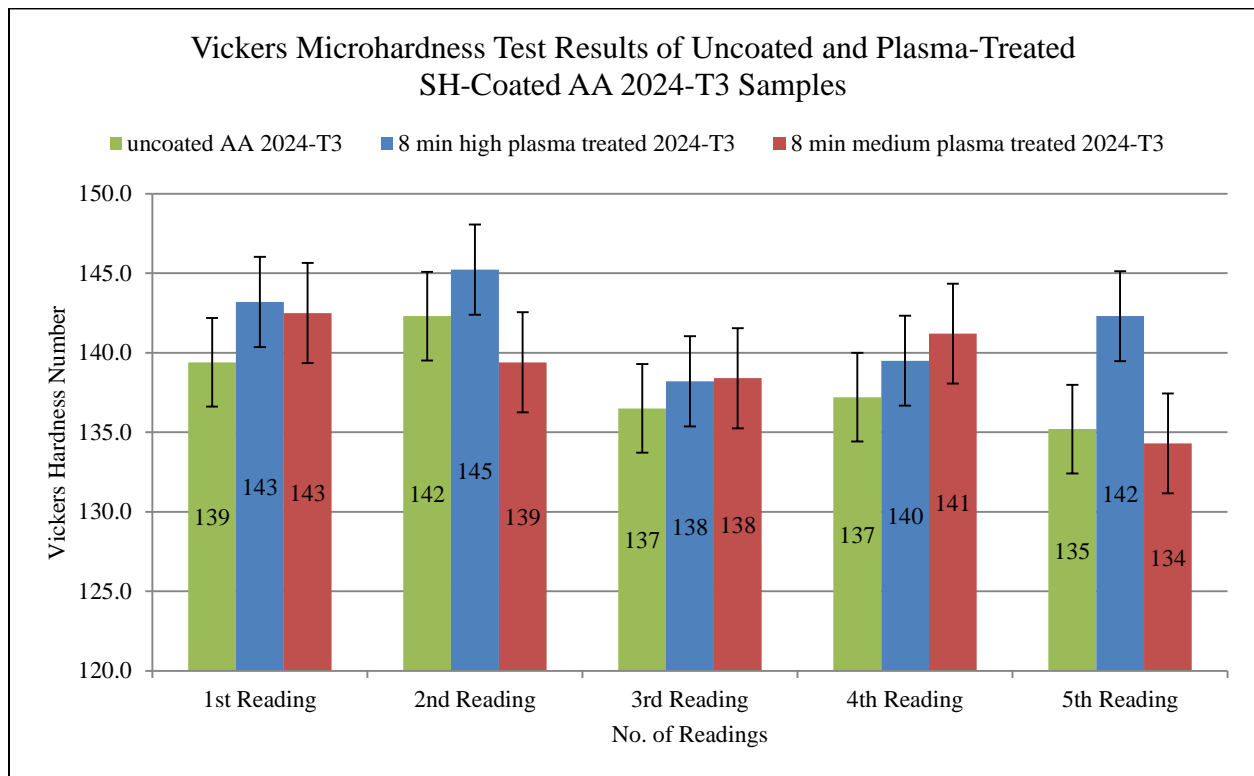


Figure 91. Vickers microhardness test results of uncoated and plasma-treated SH-coated AA 2024-T3 samples.

4.6 Deicing Test Analysis

In these tests, ice cubes were formed in a single ice cube tray. Super-cooled water was dispensed on the 8 minutes plasma-treated SH-coated AA 2024-T3 sample, and then an ice cube

was placed on top of it. Super-cooled water was important as the role of gum by sticking the ice cube to the aluminum sample. However, the 8 minutes high plasma-treated SH-coated AA 2024-T3 sample was chosen for this test, due to the significant results in the contact angle measurements, corrosion rates and all. The deicing test was performed using ice cubes and an air blower test at different surface angles (0° , 5° , 10° , and 20°).

4.6.1 Sliding Angle and Contact Angle Results of 8 Minutes Plasma-Treated SH-Coated AA 2024-T3 Sample after Deicing Test

Ice was formed on the 8 minutes plasma-treated SH-coated AA 2024-T3 sample, as mentioned previously in section 3.2, and then the test was completed. First, the ice started sliding about 19.4° , and the angle improved as the number of times the experiment was executed was increased. As it kept increasing, after the tenth time even the ice slide from the surface as the sliding angle of the surface increased and the adhesion between the aluminum surface and the ice was weak, as anticipated. The sliding angle for the 8 minutes plasma-treated SH-coated AA 2024-T3 sample is shown in Figure 92.

As the experiment was implemented, the contact angle started decreasing slightly with the increase in number of times the deicing test was completed, as shown in Figure 93. The property of the aluminum surface is being superhydrophobic surface, where it can be seen that the contact angle increased above 150° . The SH property decreased as the experiment was completed.

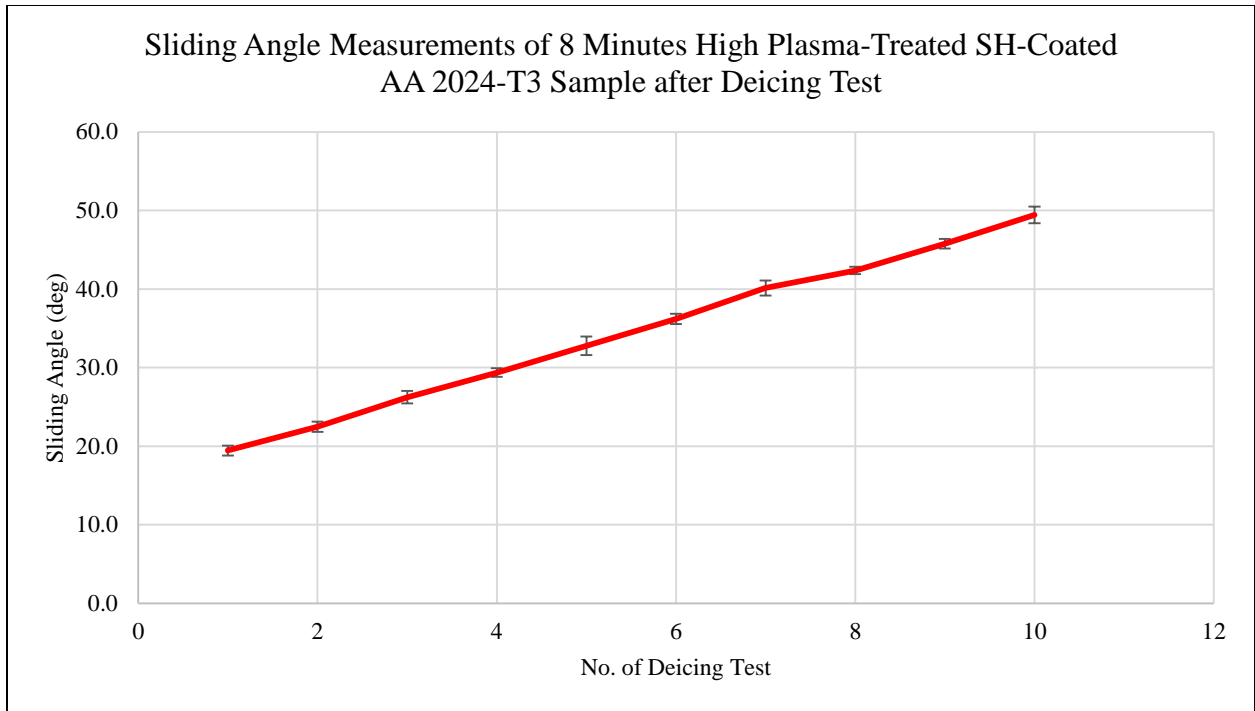


Figure 92. Sliding angle measurements of 8 minutes high plasma-treated SH-coated AA 2024-T3 sample after deicing test.

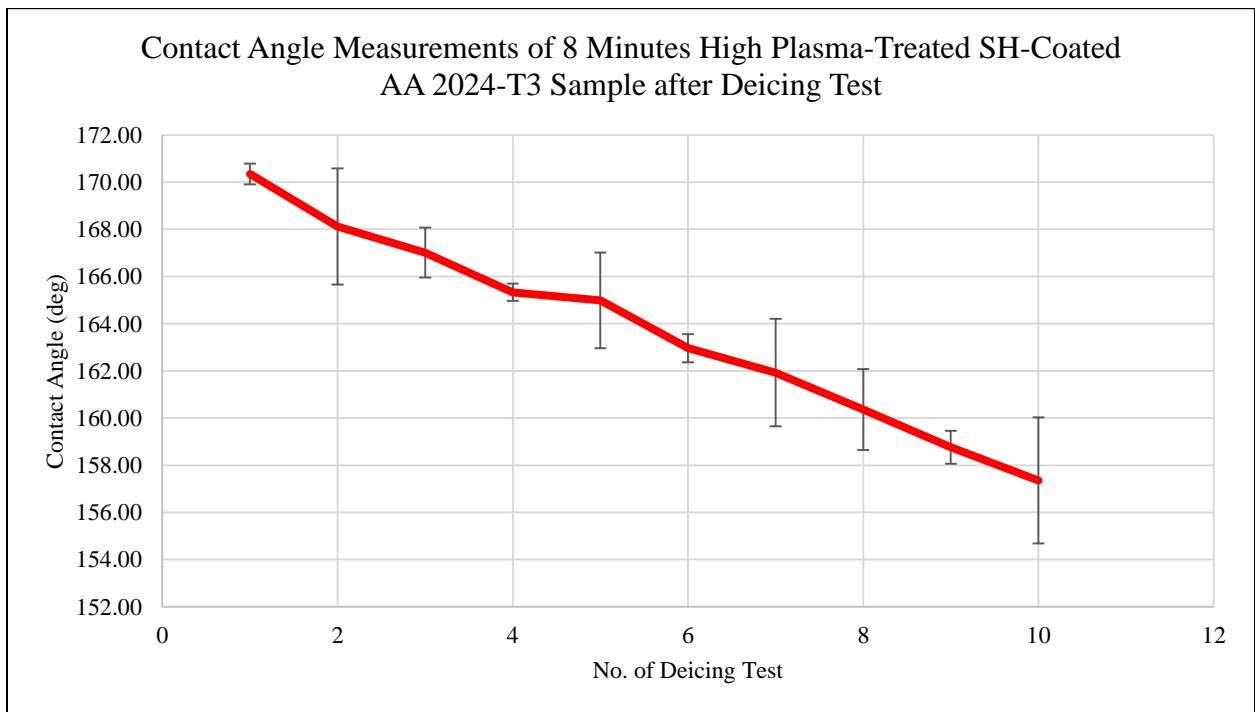


Figure 93. Contact angle measurements of 8 minutes high plasma-treated SH-coated AA 2024-T3 sample after deicing test.

4.6.2 Air Blower Test on 8 Minutes Plasma-Treated SH-Coated AA 2024-T3 Sample with Ice Cube

As air was blown on top of the 8 minutes plasma-treated SH-coated AA 2024-T3 sample with the ice cube on top, it took just one second subsequently the electric air blower was turned on to remove the ice from the aluminum sample. The similar procedure was tried numerous times and the time results continued the identical. The contact angle of the 8 minutes plasma-treated SH-coated AA 2024-T3 sample was recorded after every test. Figure 94 shows that the superhydrophobic properties of the aluminum sample drop slightly, decreasing its contact angle. Although the decreasing rate of the contact angle was steady, it remained with its superhydrophobic properties after ten tests.

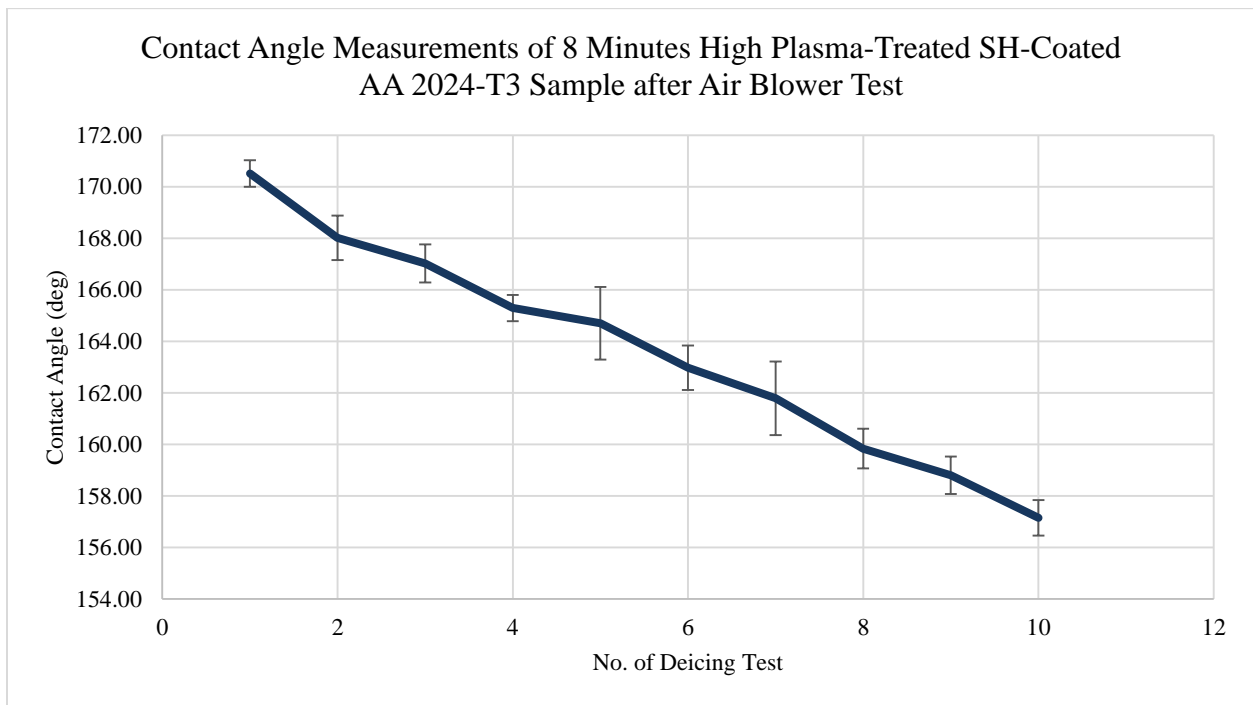


Figure 94. Contact angle measurements of 8 minutes high plasma-treated SH-coated AA 2024-T3 sample after air blower test.

4.6.3 Air Blower Test on 8 Minutes Plasma-Treated SH-Coated AA 2024-T3 Sample with Ice Cubes on Surface at Different Angles (0°, 5°, 10°, and 20°).

As air was blown on top of the 8 minutes plasma-treated SH-coated AA 2024-T3 sample with the ice cube on top, and then the air blower test was directed. The aluminum sample stayed fixed to the ground, and air was blown on the aluminum sample surface keeping the air blower at a 45° angle. The air blower applies the air velocity of 55.25 m/s. Then the 8 minutes plasma-treated SH-coated AA 2024-T3 sample was fixed with the ground at angles of 5°, 10°, and 20°, and over again air was blown onto the aluminum sample. Table 23 shows that the time necessary for the blown air to eliminate the ice cube on the aluminum sample was instantaneous. It can be observed that if the aluminum sample is placed at 0°, the time necessary to blow ice is one second, but as the tilted angle was increased, the time necessary to blow ice off the aluminum sample diminished. At angles of 5°, 10°, and 20°, ice was blown away immediately when the blower was activated.

TABLE 23

TIME REQUIRED FOR REMOVAL OF ICE FORMED FROM 8 MINUTES HIGH PLASMA-TREATED SH-COATED AA 2024-T3 SAMPLES

0° Angle of Plasma-Treated Al	5° Angle of Plasma-Treated Al	10° Angle of Plasma-Treated Al	20° Angle of Plasma-Treated Al
1 sec	Immediate	Immediate	Immediate
1 sec	Immediate	Immediate	Immediate
1 sec	Immediate	Immediate	Immediate
1 sec	Immediate	Immediate	Immediate
1 sec	Immediate	Immediate	Immediate

The contact angle results of the 8 minutes plasma-treated SH-coated AA 2024-T3 sample were documented after every test. Figure 95 shows that the superhydrophobic properties of the aluminum sample decreased slightly. Although the decreasing rate of the contact angle was steady, it remained with its superhydrophobic properties after five tests.

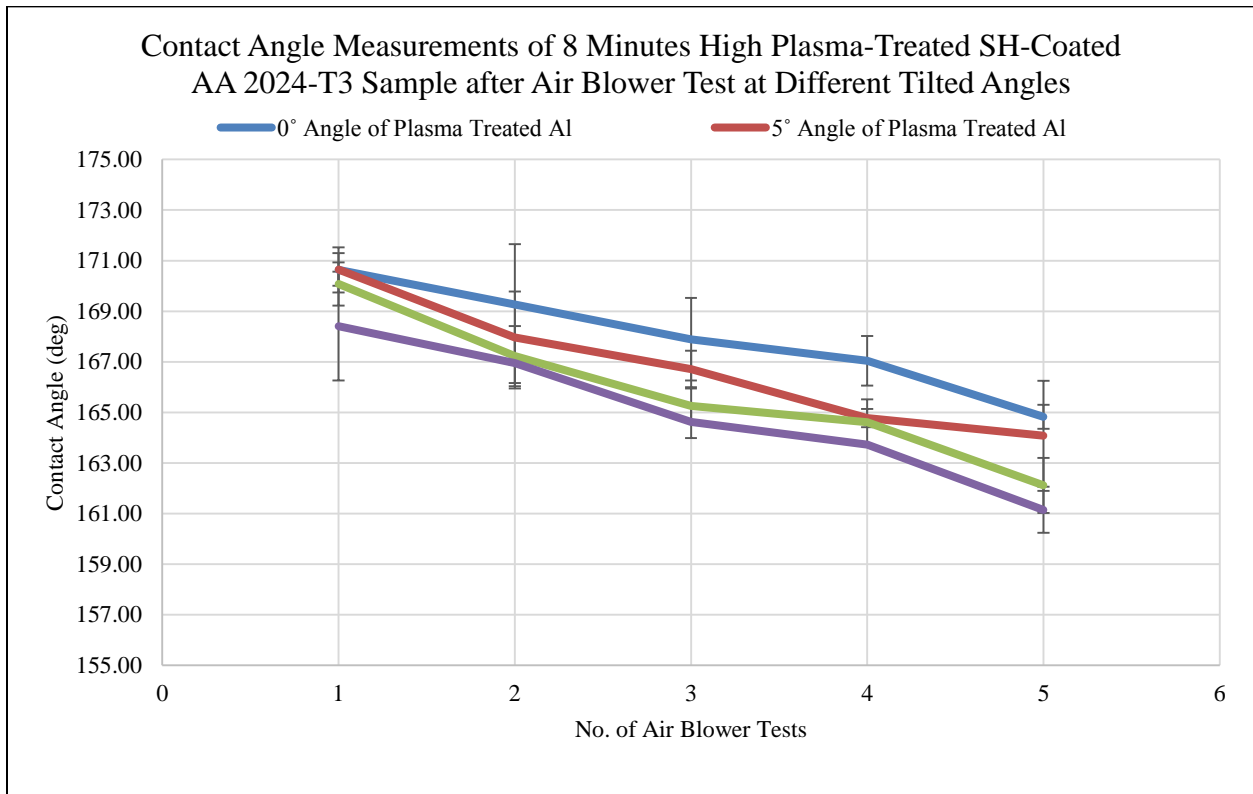


Figure 95. Contact angle measurements of 8 minutes high plasma-treated SH-coated AA 2024-T3 sample after air blower test at different tilted angles.

4.7 Self-Cleaning Ability of Plasma-Treated SH-Coated AA 2024-T3 Samples

The proficiency of the self-cleaning ability increases with the tilt angle, which is proven by the Table 24 which presents the detailed information of the experimentation process on the tilted plasma-treated SH-coated AA 2024-T3 samples and the number of sprays to remove the dust particles, in this case it is graphene powder from the surface while Figure 96 shows the steady decrease in the use of the number of sprays as we increase the tilt angle of the plasma-treated SH-coated AA 2024-T3 samples.

TABLE 24

SELF CLEANING RESULTS OF UNCOATED AND PLASMA-TREATED SH-COATED AA 2024-T3 SAMPLES

Plasma-Treated SH Coated Aluminum	5°	10°	20°	40°	60°
8 min High Plasma	5	5	4	3	1
8 min Medium Plasma	7	6	5	3	2
Uncoated Aluminum	15	13	10	8	6

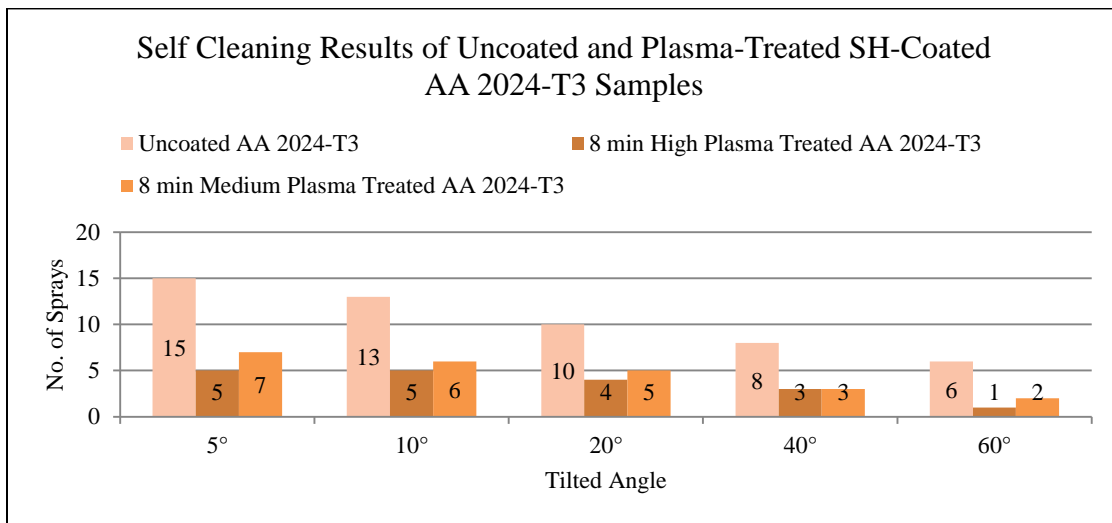


Figure 96. Self-cleaning results of uncoated and plasma-treated SH-coated AA 2024-T3 samples.

4.8 Salt Soaking Test Analysis

In these tests, samples from each test group were immersed in a 3% 0.5 M NaCl solution for 90 days at room temperature. The 4 minutes medium plasma-treated SH-coated AA 2024-T3 sample display severe damage and developed the highest corrosion rates. This might also be the result of penetration of the unwanted ions and molecules through the interface. The 4 minutes high plasma-treated SH-coated AA 2024-T3 sample showed a few edge swellings, while the 8 minutes medium plasma-treated SH-coated AA 2024-T3 sample showed only the slight color

changes. However, the 8 minutes high plasma-treated SH-coated AA 2024-T3 sample did not show significant in central or edge blisters, holes, or color changes and appeared to be in excellent conditions as compared to the other samples.

4.8.1 Contact Angle Measurement of Four Best Plasma-Treated SH-Coated AA 2024-T3 Samples after Salt Soaking Test

Contact angles results of the plasma-treated SH-coated AA 2024-T3 samples after the salt soaking test was measured and the results indicate that the 8 minutes high plasma-treated SH-coated AA 2024-T3 sample's surface remains superhydrophobic, even after 90 days of immersion in 3% 0.5M NaCl solutions. The contact angle of the 8 minutes high plasma-treated SH-coated AA 2024-T3 sample after the salt soaking test is 155.16°. The contact angle of the 4 minutes medium plasma-treated SH-coated AA 2024-T3 sample after the salt soaking test is 143.16°, which indicates that surface becomes hydrophobic surface after 90 days inside the 3% 0.5M NaCl solution. From this, the use of plasma surface cleaning treatment for a long time can give a better solution for superhydrophobicity. The contact angle measurements of the plasma-treated SH-coated AA 2024-T3 samples after salt soaking test are shown in Figure 97.

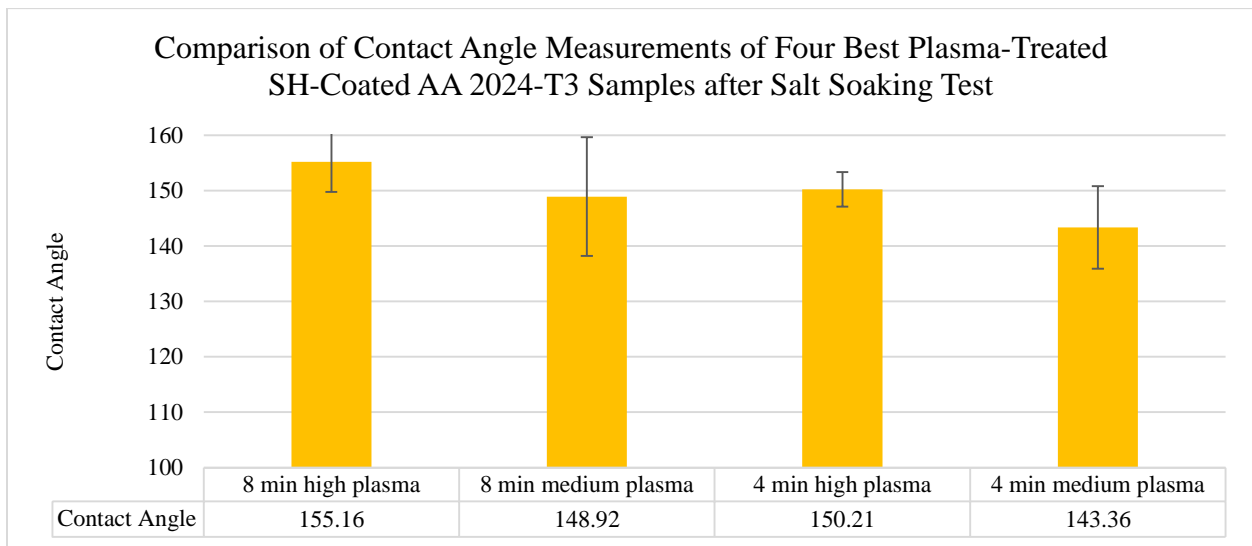


Figure 97. Comparison of contact angle measurements of four best plasma-treated SH-coated AA 2024-T3 samples after salt soaking test.

4.8.2 Polarization Curves of Four Best Plasma-Treated SH-Coated AA 2024-T3 Samples after Salt Soaking Test

PC results of the plasma-treated SH-coated AA 2024-T3 samples after salt soaking test shows the greatest effect of plasma surface cleaning treatment on preventing corrosion. From the results, the 8 minutes high plasma-treated SH-coated AA 2024-T3 sample has the greatest corrosion rate value, even after 90 days of immersion in 3% 0.5M NaCl solution. The corrosion rate of the 8 minutes high plasma-treated SH-coated AA 2024-T3 sample after the salt soaking test is 1.804E-02 mpy. Corrosion rates along with E_{corr} and I_{corr} is obtained from Tafel curves are shown in Table 25 for the plasma-treated SH-coated AA 2024-T3 samples after salt soaking test. Figure 98 shows the plasma-treated SH-coated AA 2024-T3 samples' Tafel curve after salt soaking test.

TABLE 25

CORROSION RATE PARAMETERS OF FOUR BEST PLASMA-TREATED SH-COATED AA 2024-T3 SAMPLES AFTER SALT SOAKING TEST

Category	CR (mpy)	E_{corr} (V)	I_{corr} (A)
8 min High Plasma	1.804E-02	3.570	2.050E-08
8 min Medium Plasma	2.928E-02	4.090	3.330E-07
4 min High Plasma	4.671E-02	3.300	5.320E-06
4 min Medium Plasma	5.565E-02	2.740	6.340E-06

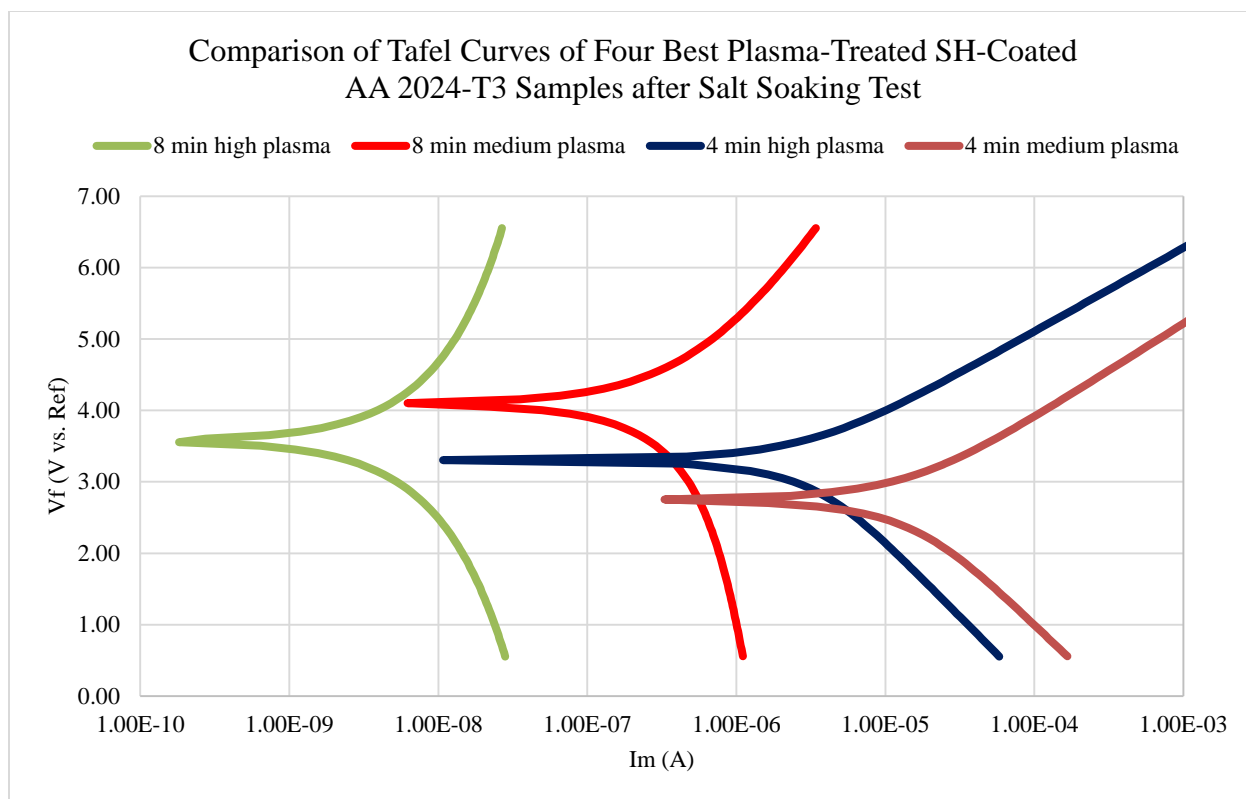


Figure 98. Comparison of Tafel curves of four best plasma-treated SH-coated AA 2024-T3 samples after salt soaking test.

4.8.3 Electrochemical Impedance Spectroscopy of Four Best Plasma-Treated SH-Coated AA 2024-T3 Samples after Salt Soaking Test

EIS results of the plasma-treated SH-coated AA 2024-T3 samples after the salt soaking test, Figure 99 and 100 specifies that just about similar styles of Nyquist plot and Bode plot for 90 days immersion time periods in 3% 0.5M NaCl solutions to attain the corrosion parameters that assigned from Randles cell circuit. Randles cell parameters' values obtained from the Nyquist plot and Bode plot are shown in Table 26. It is found that from the EIS results, the 8 minutes high plasma-treated SH-coated AA 2024-T3 sample give higher values of polarization resistance and lower values of double layer capacitance even after 90 days of immersion in 3% 0.5M NaCl solutions.

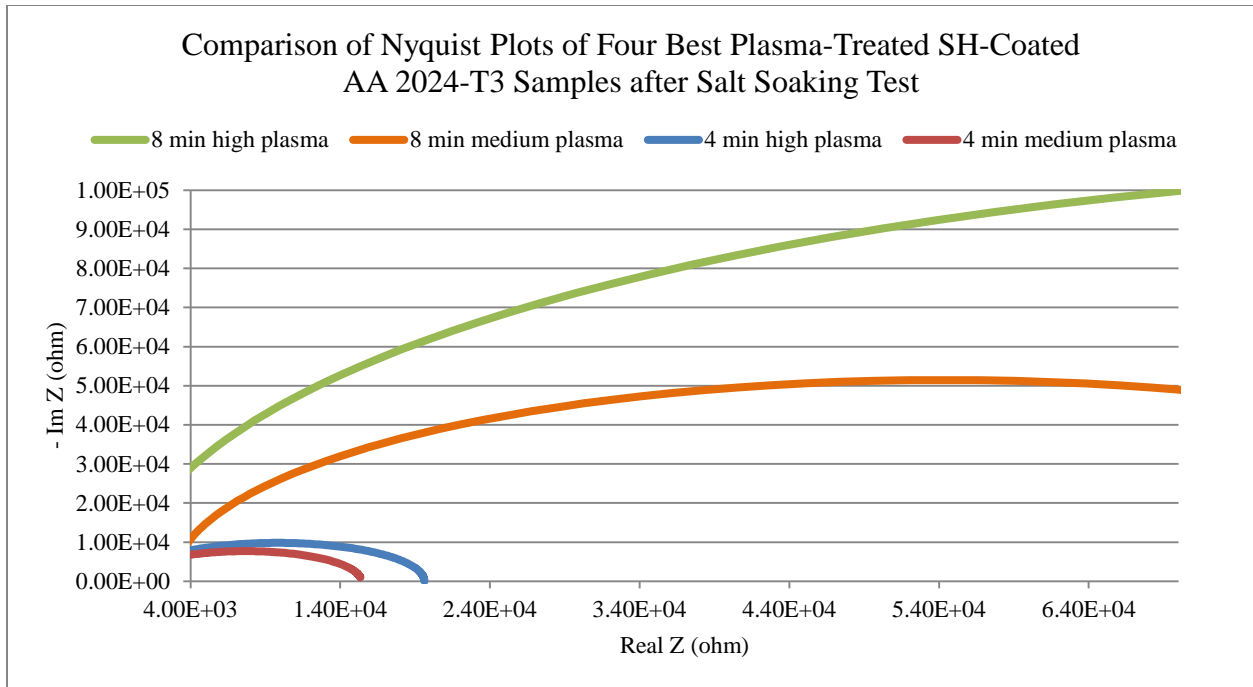


Figure 99. Comparison of Nyquist plots of four best plasma-treated SH-coated AA 2024-T3 samples after salt soaking test.

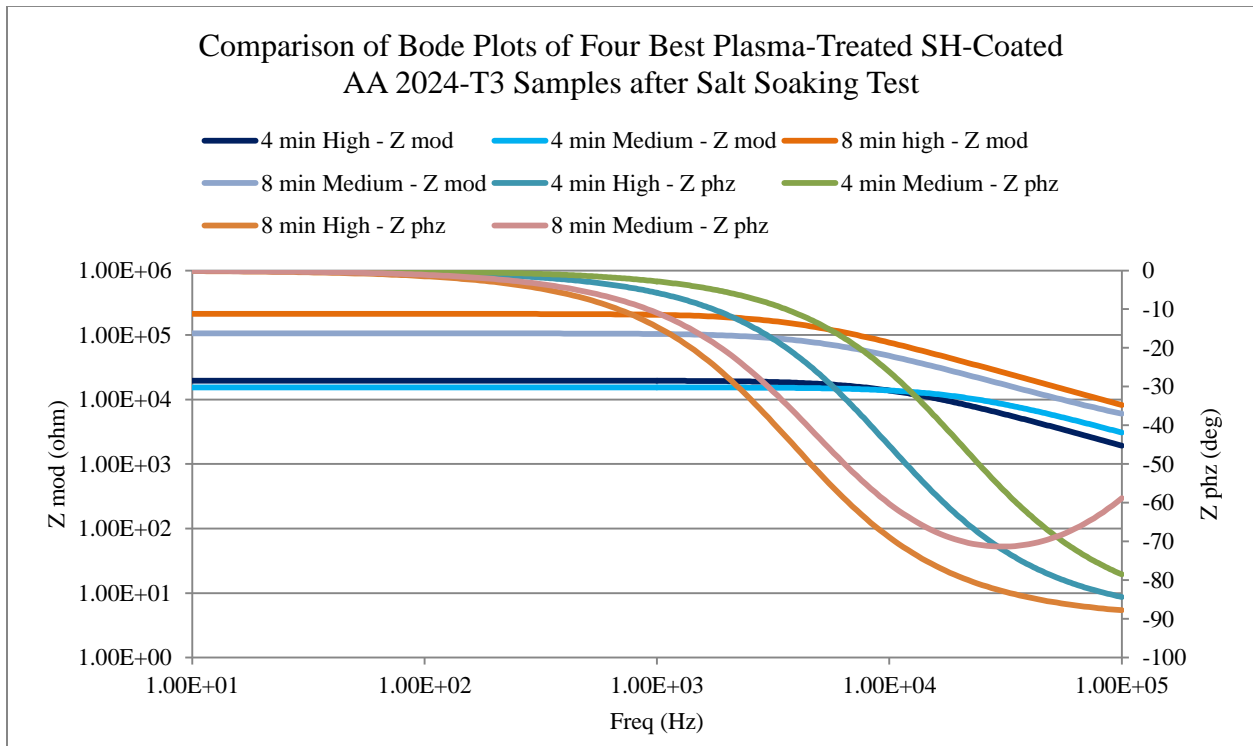


Figure 100. Comparison of Bode plots of four best plasma-treated SH-coated AA 2024-T3 samples after salt soaking test.

TABLE 26

RANGLES CELL PARAMETERS OF FOUR BEST PLASMA-TREATED SH-COATED AA 2024-T3 SAMPLES AFTER SALT SOAKING TEST

Category	Rp (ohm)	Ru (ohm)	Cdl (F)
4 min High Plasma	1.96E+04	3.17E-03	8.19E-10
4 min Medium Plasma	1.54E+04	2.93E-04	5.08E-10
8 min High Plasma	2.12E+05	7.13E-03	1.95E-10
8 min Medium Plasma	1.03E+05	2.86E-03	3.08E-10

4.9 Freezing Time Test of Plasma-Treated SH-Coated AA 2024-T3 Samples

A droplet of DI water was placed on both the uncoated and 8 minutes plasma-treated SH-coated AA 2024-T3 samples, as shown in Figure 101. Then, both samples were placed in a freezer for 30 minutes. The water droplet on the uncoated AA 2024-T3 sample froze faster than the water droplet on the 8 minutes plasma-treated SH-coated AA 2024-T3 sample, which eliminated the ice drop more quickly than the uncoated sample. The frozen water droplets are shown in Figure 102.



Figure 101. Water droplet on plasma-treated SH-coated AA 2024-T3 sample (left) and uncoated AA 2024-T3 sample (right).



Figure 102. Frozen water droplet on plasma-treated SH-coated AA 2024-T3 sample (left) and uncoated AA 2024-T3 sample (right).

4.10 Super-Cooled Water Test of Plasma-Treated SH-Coated AA 2024-T3 Samples

Chilled super-cooled water was dropped on both the 8 minutes plasma-treated SH-coated AA 2024-T3 sample and uncoated AA 2024-T3 sample as shown in Figure 103. When super-cooled water is poured down on the 8 minutes plasma-treated SH-coated AA 2024-T3 sample, there was no realization of ice on the surface. However, on uncoated AA 2024-T3 sample, some ice flakes shaped on the surface as super-cooled water was dropped through it. Super-cooled water spontaneously changes its state from liquid to solid when it originates the interaction through the flat, smooth surface. On the 8 minutes, plasma-treated SH-coated AA 2024-T3 sample, the surface roughness is high, and it does not permit ice to form on the surface when super-cooled water was dropped on it.



Figure 103. Super-cooled water test on plasma-treated SH-coated AA 2024-T3 sample (left) and uncoated AA 2024-T3 sample (right).

CHAPTER 5

CONCLUSIONS

This research study showed that the plasma surface cleaning treatment plays a significant role in preventing corrosion highly robust superhydrophobic coatings on the decided material, in this case Aluminum 2024-T3 alloy. The plasma surface cleaning treatment of the Aluminum 2024-T3 alloy served as corrosion protection of the bare metal, forming robust physical or chemical bonds on the substrate, stopping delamination of the coating system, and increasing the adhesiveness between the substrate and the top coat.

This study mainly focused on superhydrophobicity, wettability, and corrosion prevention using the plasma surface cleaning technique, effects of the mechanical properties on the Aluminum 2024-T3 alloy after coating, the self-cleaning mechanism, the significance of self-cleaning mechanism on tilted surfaces, and deicing properties of the superhydrophobic-coated surfaces.

In this research, Aluminum 2024-T3 alloy was treated with plasma, coated with a superhydrophobic coating, and heat treated a highly robust superhydrophobic coating on the metal surface. The tape adhesive test showed that the contact angle started to decrease slightly with each peel test. However, this rate of reduction was minimum. This test also clearly showed how highly robust the metal surface was with the superhydrophobic coating for a longer period of time. After the samples were immersed in 3% 0.5M NaCl solution for 30 days, the samples showed a slight decrease in contact angle. As the immersion days were increased, the contact angles slowly decreased.

The electrochemical results in this study showed that the corrosion rates of the plasma-treated SH-coated AA 2024-T3 samples were undesirably low and increased with the increase in

immersion time in the NaCl solution. The corrosion rate of the 8 minutes high plasma-treated SH-coated samples did not increase as much as when the immersion time in the NaCl solution was increased. Under the conditions of exposure studied, this alloy suffered from pitting corrosion that took place around the intermetallic particles existing in the alloy. It was observed that the plasma surface cleaning method increased the adhesiveness between the substrate and the top coat, which caused the surface to remain superhydrophobic coated for a long period of time. This also reduced the corrosion rate, which has a double effect on the surface.

The Vickers microhardness test showed that the mechanical properties of the surface did not change as a result of the plasma surface cleaning treatment. The Vickers microhardness number remained constant in this study. This study also demonstrated that the more the surface is tilted, the less time it takes water to self-clean the surface. Deicing observations showed that ice that is formed on the plasma-treated SH-coated AA 2024-T3 samples can be removed easily using an air blower by placing the material at an angle. Notably, this type of surface does not allow ice to stay on the surface, which was proven by the freezing time test and the super-cooled water test.

In conclusion, it can be said that the techniques used in this study are simple and easy, but this plasma surface cleaning treatment can help the Aluminum 2024-T3 alloy to highly robust superhydrophobic coating, which is advantageous for corrosion, deicing, and self-cleaning.

CHAPTER 6

FUTURE WORK

Corrosion is a continuously significant problem in the world. Plasma surface cleaning treatment has emerged as a probable solution to this concern. Using plasma surface cleaning treatment to form a superhydrophobic coating on the metal surface can be one reliable solution to corrosion. Based on the results of this study, some supplementary work that might be completed in this field are the following:

- Use additional nanoparticles to create a strong bonding between the top coat and substrate.
- Apply the same technique to check validity with lightning strikes.
- Conduct more tests on plasma-treated SH-coated AA2024-T3 samples to check for durability and reliability.
- Use plasma surface cleaning treatment for 12 minutes and 16 minutes.
- Explore the corrosion parameter with steel, zinc, and iron.
- Perform the cross-cut test and x-cut test.
- Work on creating a unique bottom coat and top coat using a significant amount of nanoparticles.
- Perform a study based on corrosion rates using extended immersion times in the NaCl solution.
- Use already-coated metal that is frequently applied in aircraft, apply the same technique on the surface, and check the corrosion properties.

REFERENCES

REFERENCES

- [1] DeviantArt, [Online], *adv37.*, [cited Jan. 20, 2018]. Available:<https://urbex-fantasy.deviantart.com/art/adv37-62749095>.
- [2] C.-H. Xue, S.-T. Jia, J. Zhang, and J.-Z. Ma, "Large-area fabrication of superhydrophobic surfaces for practical applications: an overview," *Science and Technology of Advanced Materials*, vol. 11, pp. 033-002, 2010.
- [3] J. Drelich and E. Chibowski, "Superhydrophilic and superwetting surfaces: definition and mechanisms of control," *Langmuir*, vol. 26, pp. 18621-18623, 2010.
- [4] E. J. Falde, S. T. Yohe, Y. L. Colson, and M. W. Grinstaff, "Superhydrophobic materials for biomedical applications," *Biomaterials*, vol. 104, pp. 87-103, 2016.
- [5] IFLScience, "Superhydrophobic Material Developed That Makes Water Bounce Like A Ball", [Online], [cited Jan. 20, 2018]. Available: <http://www.iflscience.com/technology/superhydrophobic-material-developed-makes-water-bounce-ball/>.
- [6] J. Borges and J. F. Mano, "Molecular interactions driving the layer-by-layer assembly of multilayers," *Chemical Reviews*, vol. 114, pp. 8883-8942, 2014.
- [7] H. Ogihara, J. Xie, J. Okagaki, and T. Saji, "Simple method for preparing superhydrophobic paper: spray-deposited hydrophobic silica nanoparticle coatings exhibit high water-repellency and transparency," *Langmuir*, vol. 28, pp. 4605-4608, 2012.
- [8] F. C. Campbell Jr, *Manufacturing Technology for Aerospace Structural Materials*: Elsevier, 2011.
- [9] T. Burns, "Characteristics of Heat Treatable vs. Non Heat Treatable Aluminum Alloys.", [Online], [cited Jan. 20, 2018]. Available: <http://www.fabricatingandmetalworking.com/2014/02/characteristics-of-heat-treatable-vs-non-heat-treatable-aluminum-alloys/>.
- [10] J. Davis, *Aluminum and Auminum Alloys*: ASM international, 2013.
- [11] T. L. Durbin, "Modeling dissolution in aluminum alloys", *Ph.D. Dissteration*, Georgia Institute of Technology, 2005.
- [12] M. Peters and C. Leyens, "Aerospace and space materials," *Material Science and Engineering*, 2009.

REFERENCES (continued)

- [13] G. Wranglén, "An introduction to corrosion and protection of metals," *Anti-Corrosion Methods and Materials*, vol. 19, pp. 5-5, 1972.
- [14] Alumeco. "Corrosion: Reasons, types and solution", [Online], [cited Jan. 20, 2018]. Available: <https://www.alumeco.com/knowledge-technique/general/aluminium-corrosion>.
- [15] D. A. Jones, *Principles and Prevention of Corrosion*: Prentice Hall, 1996.
- [16] D. Zhu, "Corrosion protection of metals by silane surface treatment", *Ph.D. Dissteration*, University of Cincinnati, 2005.
- [17] A. E. Hughes, N. Birbilis, J. M. Mol, S. J. Garcia, X. Zhou, and G. E. Thompson, "High strength Al-alloys: microstructure, corrosion and principles of protection," in *Recent Trends in Processing and Degradation of Aluminium Alloys*, ed: InTech, 2011.
- [18] H. Shalaby, A. Al-Hashem, M. Lowther, and J. Al-Besharah, *Industrial Corrosion and Corrosion Control Technology*: KISR, 1996.
- [19] H. R. Golsefatan, M. Fazeli, A. R. Mehrabadi, and H. Ghomi, "Enhancement of corrosion resistance in thermal desalination plants by diamond like carbon coating," *Desalination*, vol. 409, pp. 183-188, 2017.
- [20] Nace., "Uniform Corrosion." [Online], [cited Jan. 20, 2018]. Available: <https://www.nace.org/Corrosion-Central/Corrosion-101/Uniform-Corrosion/>.
- [21] H. Pulkkinen, H. Apajalahti, S. Papula, J. Talonen, and H. Hänninen, "Pitting corrosion resistance of Mn-alloyed austenitic stainless steels," *steel research international*, vol. 85, pp. 324-335, 2014.
- [22] S. H. Zaferani, "Failure Analysis of Corrosion Case Histories," *OMICS Group eBooks*, Foster City, 2015.
- [23] M. Raunio, "Basic approaches and goals for crevice corrosion modelling.", 2015
- [24] J.-J. Lee, K.-Y. Song, S.-G. Ahn, J.-Y. Choi, J.-M. Seo, and J.-M. Park, "Evaluation of effect of galvanic corrosion between nickel-chromium metal and titanium on ion release and cell toxicity," *The Journal of Advanced Prosthodontics*, vol. 7, pp. 172-177, 2015.
- [25] A. Moncmanová, "Environmental factors that influence the deterioration of materials," *Environmental Deterioration of Materials*. Athenaeum Press Ltd, Great Britain, pp. 4-21, 2007.

REFERENCES (continued)

- [26] Medium. , "A Guide To Galvanic Corrosion & How To Treat It – Alex Newton – Medium", [Online], [cited Jan. 20, 2018]. Available: <https://medium.com/@alex.newton1992/a-guide-to-galvanic-corrosion-how-to-treat-it-f2c622692eed>.
- [27] S. Syed, "Atmospheric corrosion of materials," *Emirates Journal for Engineering Research*, vol. 11, pp. 1-24, 2006.
- [28] R.-c. Zeng, J. Zhang, W.-j. Huang, W. Dietzel, K. Kainer, C. Blawert, *et al.*, "Review of studies on corrosion of magnesium alloys," *Transactions of Nonferrous Metals Society of China*, vol. 16, pp. s763-s771, 2006.
- [29] E. Ghali, W. Dietzel, and K.-U. Kainer, "General and localized corrosion of magnesium alloys: a critical review," *Journal of Materials Engineering and Performance*, vol. 13, pp. 7-23, 2004.
- [30] B. J. Little and J. S. Lee, "Microbiologically Influenced Corrosion," in *Kirk-Othmer Encyclopedia of Chemical Technology*, ed: John Wiley & Sons, Inc., 2000.
- [31] T. Harvey, J. Wharton, and R. Wood, "Development of synergy model for erosion–corrosion of carbon steel in a slurry pot," *Tribology-Materials, Surfaces & Interfaces*, vol. 1, pp. 33-47, 2007.
- [32] M. Esmaily, J. Svensson, S. Fajardo, N. Birbilis, G. Frankel, S. Virtanen, *et al.*, "Fundamentals and advances in magnesium alloy corrosion," *Progress in Materials Science*, vol. 89, pp. 92-193, 2017.
- [33] Y. I. Kuznetsov and J. G. N. Thomas, *Organic Inhibitors of Corrosion of Metals*: Springer, 1996.
- [34] Nde-ed , "Corrosion Properties.", [Online], [cited Jan. 20, 2018]. Available: https://www.nde-ed.org/EducationResources/CommunityCollege/Materials/Physical_Chemical/Corrosion.htm.
- [35] J. Zhang, Z. Xia, and L. Dai, "Carbon-based electrocatalysts for advanced energy conversion and storage," *Science Advances*, vol. 1, p. e1500564, 2015.
- [36] S. Gudić, I. Smoljko, and M. Kliškić, "The effect of small addition of tin and indium on the corrosion behavior of aluminium in chloride solution," *Journal of Alloys and Compounds*, vol. 505, pp. 54-63, 2010.

REFERENCES (continued)

- [37] A. R. Mendoza and F. Corvo, "Outdoor and indoor atmospheric corrosion of non-ferrous metals," *Corrosion Science*, vol. 42, pp. 1123-1147, 2000.
- [38] A. M. Lucente and J. R. Scully, "Pitting and alkaline dissolution of an amorphous–nanocrystalline alloy with solute-lean nanocrystals," *Corrosion Science*, vol. 49, pp. 2351-2361, 2007.
- [39] D. D. Macdonald, "The point defect model for the passive state," *Journal of the Electrochemical Society*, vol. 139, pp. 3434-3449, 1992.
- [40] F. Administration., "Lessons Learned." [Online], [cited Jan. 20, 2018]. Available: http://lessonslearned.faa.gov/ll_main.cfm?TabID=2&LLID=75&LLTypeID=2.
- [41] T. Li, X. Li, C. Dong, and Y. Cheng, "Characterization of atmospheric corrosion of 2A12 aluminum alloy in tropical marine environment," *Journal of Materials Engineering and Performance*, vol. 19, pp. 591-598, 2010.
- [42] Nace., "CORROSION FAILURES: Lowe's Motor Speedway Bridge Collapse". [Online], [cited Jan. 20, 2018]. Available: <https://www.nace.org/CORROSION-FAILURES-Lowes-Motor-Speedway-Bridge-Collapse.aspx>.
- [43] R. J. McKay and R. Worthington, *Corrosion Resistance of Metals and Alloys*: Reinhold Publishing Corporation.; New York, 1936.
- [44] N. Warren, *Metal Corrosion in Boats: The Prevention of Metal Corrosion in Hulls, Engines, Rigging and Fittings*: Sheridan House, Inc., 2006.
- [45] M. Dibetsoe, "Gravimetric, Electrochemical and Quantum chemical studies of some Naphthalocyanine and Pthalocyanine derivatives as corrosion inhibitors for aluminium in acidic medium," 2014.
- [46] A. Bhatia, "Cooling water problems and solutions," *Continuing Education and Development, Inc*, vol. 9, pp. 005-009, 2003.
- [47] I. CP Solutions, "Corrosion Control Solutions", [Online], [cited Jan. 20, 2018]. Available: <https://cpsolutionsinc.net/corrosion-control-solutions/>.
- [48] G. Kakuba, "The impressed current cathodic protection system," *Master's Thesis, Technische Universiteit of Eindhoven*, 2005.
- [49] J. R. Davis, *Corrosion: Understanding the Basics*: ASM International, 2000.

REFERENCES (continued)

- [50] L. Guo, I. B. Obot, X. Zheng, X. Shen, Y. Qiang, S. Kaya, *et al.*, "Theoretical insight into an empirical rule about organic corrosion inhibitors containing nitrogen, oxygen, and sulfur atoms," *Applied Surface Science*, vol. 406, pp. 301-306, 2017/06/01/ 2017.
- [51] R. Solmaz, G. Kardaş, M. Culha, and M. Erbil, "Investigation of adsorption and inhibitive effect of 2-mercaptothiazoline on corrosion of mild steel in hydrochloric acid media," *Electrochimica Acta*, vol. 53, pp. 5941-5952, 2008.
- [52] B. Rani and B. B. J. Basu, "Green inhibitors for corrosion protection of metals and alloys: an overview," *International Journal of Corrosion*, vol. 2012, 2012.
- [53] Z. W. Wicks, F. N. Jones, S. P. Pappas, and D. A. Wicks, "Binders based on polyisocyanates: polyurethanes," *Organic Coatings: Science and Technology, Third Edition*, pp. 231-270, 2007.
- [54] Globalspec. "Industrial Coatings Information.", [Online], [cited Jan. 20, 2018]. Available: http://www.globalspec.com/learnmore/materials_chemicals_adhesives/industrial_sealants_coatings/industrial_coatings.
- [55] W. Freitag and D. Stoye, *Paints, Coatings and Solvents*: Wiley, 2008.
- [56] J. Gray and B. Luan, "Protective coatings on magnesium and its alloys—a critical review," *Journal of Alloys and Compounds*, vol. 336, pp. 88-113, 2002.
- [57] Y.-Y. Chang, C.-C. Tsaur, and J. C. Rock, "Microstructure studies of an aluminide coating on 9Cr-1Mo steel during high temperature oxidation," *Surface and Coatings Technology*, vol. 200, pp. 6588-6593, 2006.
- [58] American Galvanizers Association, "HDG Process", [Online], [cited Jan. 20, 2018]. Available: <https://www.galvanizeit.org/hot-dip-galvanizing/what-is-hot-dip-galvanizing-hdg/hdg-process#inspection>.
- [59] A. Sparavigna, "Plasma Treatment Advantages for Textiles," *arXiv preprint arXiv:0801.3727*, 2008.
- [60] F. Mansfeld and F. Perez, "Surface modification of aluminum alloys in molten salts containing CeCl₃," *Thin Solid Films*, vol. 270, pp. 417-421, 1995.
- [61] M. Petrunin, A. Nazarov, and Y. N. Mikhailovski, "Formation mechanism and anticorrosive properties of thin siloxane films on metal surfaces," *Journal of the Electrochemical Society*, vol. 143, pp. 251-257, 1996.

REFERENCES (continued)

- [62] C. Borcia, G. Borcia, and N. Dumitrascu, "Surface treatment of polymers by plasma and UV radiation," *Romanian Journal in Physics*, vol. 56, pp. 224-232, 2011.
- [63] H. P. Treatment, "Plasma Treatment Explained in Simple Terms.", [Online], [cited Jan. 20, 2018]. Available: <https://plasmamatreatment.co.uk/henniker-plasma-technology/plasma-surface-technology/plasma-technology-what-is-plasma-treatment/plasma-treatment-explained>.
- [64] E. M. Liston, "Plasma treatment for improved bonding: a review," *The Journal of Adhesion*, vol. 30, pp. 199-218, 1989.
- [65] Anon. "Applications For Plasma Surface Treatment In The Medical Industry." [Online], [cited Jan. 20, 2018]. Available: <https://www.adhesivesmag.com/articles/83423-applications-for-plasma-surface-treatment-in-the-medical-industry>.
- [66] C.-M. Chan, T.-M. Ko, and H. Hiraoka, "Polymer surface modification by plasmas and photons," *Surface Science Reports*, vol. 24, pp. 1-54, 1996.
- [67] S. Mändl and B. Rauschenbach, "Improving the biocompatibility of medical implants with plasma immersion ion implantation," *Surface and Coatings Technology*, vol. 156, pp. 276-283, 2002.
- [68] M. B. Kizling and S. G. Järås, "A review of the use of plasma techniques in catalyst preparation and catalytic reactions," *Applied Catalysis A: General*, vol. 147, pp. 1-21, 1996.
- [69] A. Ohl, W. Schleinitz, A. Meyer-Sievers, A. Becker, D. Keller, K. Schröder, *et al.*, "Design of an UHV reactor system for plasma surface treatment of polymer materials," *Surface and Coatings Technology*, vol. 116, pp. 1006-1010, 1999.
- [70] A. Ohl and K. Schröder, "Plasma-induced chemical micropatterning for cell culturing applications: a brief review," *Surface and Coatings Technology*, vol. 116, pp. 820-830, 1999.
- [71] T. Vargo, E. Bekos, Y. Kim, J. Ranieri, R. Bellamkonda, P. Aebischer, *et al.*, "Synthesis and characterization of fluoropolymeric substrata with immobilized minimal peptide sequences for cell adhesion studies. I," *Journal of Biomedical Materials Research Part A*, vol. 29, pp. 767-778, 1995.
- [72] J. Bockris and A. Reddy, "Ion-Solvent Interactions," in *Modern Electrochemistry 1: Ionics*, ed Boston, MA: Springer US, 1998, pp. 35-224.

REFERENCES (continued)

- [73] R. Ramachandran and M. Nosonovsky, "Coupling of surface energy with electric potential makes superhydrophobic surfaces corrosion-resistant," *Physical Chemistry Chemical Physics*, vol. 17, pp. 24988-24997, 2015.
- [74] Gamry, "Electrochemical Corrosion Measurements-Galvanic Corrosion.", [Online], [cited Jan. 20, 2018]. Available: <https://www.gamry.com/application-notes/corrosion-coatings/basics-of-electrochemical-corrosion-measurements/>.
- [75] Q.-A. Huang, R. Hui, B. Wang, and J. Zhang, "A review of AC impedance modeling and validation in SOFC diagnosis," *Electrochimica Acta*, vol. 52, pp. 8144-8164, 2007.
- [76] D. Pletcher and F. C. Walsh, *Industrial electrochemistry*: Springer Science & Business Media, 2012.
- [77] L. Lu and X.-g. Li, "Corrosion products of reverse crevice corrosion of copper," *International Journal of Minerals, Metallurgy, and Materials*, vol. 18, pp. 320-324, June 01 2011.
- [78] D. L. Piron, *The Electrochemistry of Corrosion*: Houston Univ., 1991.
- [79] S. Barnartt, "High-temperature pH of dilute ammonia and ammonium chloride solutions and mixtures with strong alkali," *Corrosion*, vol. 42, pp. 549-554, 1986.
- [80] Q. Wang, J.-E. Moser, and M. Grätzel, "Electrochemical impedance spectroscopic analysis of dye-sensitized solar cells," *The Journal of Physical Chemistry B*, vol. 109, pp. 14945-14953, 2005.
- [81] J. R. Macdonald and E. Barsoukov, "Impedance spectroscopy: theory, experiment, and applications," *History*, vol. 1, 2005.
- [82] S. Singh, "Electrochemical Properties of SiC-C Microelectrode System for Neuronal and Biochemical Sensing," University of Cincinnati, 2005.
- [83] V. S. Bagotsky, *Fundamentals of Electrochemistry* vol. 44: John Wiley & Sons, 2005.
- [84] A. J. Bard and L. R. Faulkner, "Fundamentals and applications," *Electrochemical Methods*, vol. 2, p. 482, 2001.
- [85] M. E. Orazem and B. Tribollet, *Electrochemical impedance spectroscopy* vol. 48: John Wiley & Sons, 2011.

REFERENCES (continued)

- [86] M. N. El-Haddad, "Hydroxyethylcellulose used as an eco-friendly inhibitor for 1018 c-steel corrosion in 3.5% NaCl solution," *Carbohydrate Polymers*, vol. 112, pp. 595-602, 2014.
- [87] J. Garcia-Jareno, D. Gimenez-Romero, M. Keddad, and F. Vicente, "Graphical analysis of electrochemical impedance spectroscopy of two consecutive irreversible electron transfers. 1. Theoretical study of the anodic dissolution of metals," *The Journal of Physical Chemistry B*, vol. 109, pp. 4584-4592, 2005.
- [88] V. Sridharan, "Measurement of Carbon Dioxide Corrosion on Carbon Steel Using Electrochemical Frequency Modulation", *Master's Thesis*, Department of Chemical Engineering University of Saskatchewan, 2009.
- [89] P. Modiba, "Electrolytes for redox flow battery systems," Stellenbosch: University of Stellenbosch, 2010.
- [90] L. Feng, S. Li, Y. Li, H. Li, L. Zhang, J. Zhai, *et al.*, "Super-hydrophobic surfaces: from natural to artificial," *Advanced Materials*, vol. 14, pp. 1857-1860, 2002.
- [91] K. Knausgård, "Superhydrophobic anti-ice nanocoatings," Institutt for konstruksjonsteknikk, 2012.
- [92] M. Ma and R. M. Hill, "Superhydrophobic surfaces," *Current opinion in colloid & interface science*, vol. 11, pp. 193-202, 2006.
- [93] L. Oberli, D. Caruso, C. Hall, M. Fabretto, P. J. Murphy, and D. Evans, "Condensation and freezing of droplets on superhydrophobic surfaces," *Advances in Colloid and Interface Science*, vol. 210, pp. 47-57, 2014/08/01/ 2014.
- [94] T. Brar, P. France, and P. G. Smirniotis, "Heterogeneous versus homogeneous nucleation and growth of zeolite A," *The Journal of Physical Chemistry B*, vol. 105, pp. 5383-5390, 2001.
- [95] A. M. A. Mohamed, A. M. Abdullah, and N. A. Younan, "Corrosion behavior of superhydrophobic surfaces: A review," *Arabian Journal of Chemistry*, vol. 8, pp. 749-765, 2015/11/01/ 2015.
- [96] S. Pal, D. Roccatano, H. Weiss, H. Keller, and F. Müller-Plathe, "Molecular dynamics simulation of water near nanostructured hydrophobic surfaces: interfacial energies," *ChemPhysChem*, vol. 6, pp. 1641-1649, 2005.
- [97] Wikimedia Commons, "Contact angle." [Online], [cited Jan. 21, 2018]. Available: https://commons.wikimedia.org/wiki/File:Contact_angle.svg.

REFERENCES (continued)

- [98] A. Balkenende, H. Van de Boogaard, M. Scholten, and N. Willard, "Evaluation of different approaches to assess the surface tension of low-energy solids by means of contact angle measurements," *Langmuir*, vol. 14, pp. 5907-5912, 1998.
- [99] G. Alberti and A. DeSimone, "Wetting of rough surfaces: a homogenization approach," in *Proceedings of the Royal Society of London A: Mathematical, Physical and Engineering Sciences*, 2005, pp. 79-97.
- [100] E. Hosono, S. Fujihara, I. Honma, and H. Zhou, "The fabrication of an upright-standing zinc oxide nanosheet for use in dye-sensitized solar cells," *Advanced Materials*, vol. 17, pp. 2091-2094, 2005.
- [101] J. B.-C. T.-D. Quéré, "Rough wetting," *EPL (Europhysics Letters)*, vol. 55.
- [102] L. Shuangping. "Lotus effect." [Online], [cited Jan. 21, 2018]. Available: http://phylab.fudan.edu.cn/doku.php?id=home:whyx:proj:lotus_leaf#%E8%8D%B7%E5%8F%B6%E6%95%88%E5%BA%94.
- [103] R. Rosario, D. Gust, A. A. Garcia, M. Hayes, J. Taraci, T. Clement, *et al.*, "Lotus effect amplifies light-induced contact angle switching," *The Journal of Physical Chemistry B*, vol. 108, pp. 12640-12642, 2004.
- [104] Q.-S. Zheng, Y. Yu, and Z.-H. Zhao, "Effects of hydraulic pressure on the stability and transition of wetting modes of superhydrophobic surfaces," *Langmuir*, vol. 21, pp. 12207-12212, 2005.
- [105] V. H. Kwong, M. A. Mossman, and L. A. Whitehead, "Control of reflectance of liquid droplets by means of electrowetting," *Applied Optics*, vol. 43, pp. 808-813, 2004.
- [106] A. Marmur, "Wetting on hydrophobic rough surfaces: to be heterogeneous or not to be?," *Langmuir*, vol. 19, pp. 8343-8348, 2003.
- [107] S. M. Fikke, J. E. Kristjánsson, and B. E. K. Nygaard, "Modern meteorology and atmospheric icing," in *Atmospheric Icing of Power Networks*, ed: Springer, 2008, pp. 1-29.
- [108] R. Cattin, S. Kunz, A. Heimo, R. Oechslin, and M. Russi, *An improved approach for the determination of in-cloud icing at wind turbine sites* vol. 6490, 1530.
- [109] C. D. Ahrens, *Meteorology Today: An Introduction To Weather, Climate, and The Environment*: Cengage Learning, 2012.

REFERENCES (continued)

- [110] A. Boag, D. McCulloch, D. Jamieson, S. Hearne, A. Hughes, C. Ryan, *et al.*, "Analysis of Intermetallic Phases in Aerospace Aluminium Alloys Using a Nuclear Microprobe and Phase Correlation Mapping," 2005.